ATLAS NOTE

ATLAS-CONF-2015-012

17th March 2015

Search for production of vector-like quark pairs and of four top quarks in the lepton plus jets final state in pp collisions at $\sqrt{s}$ = 8 TeV with the ATLAS detector

The ATLAS Collaboration

Abstract

A search is presented for pair production of vector-like quarks, both up-type (T) and down-type (B), as well as for four-top-quark production. The search is based on pp collisions at $\sqrt{s}$ = 8 TeV recorded in 2012 with the ATLAS detector at the CERN Large Hadron Collider and corresponding to an integrated luminosity of 20.3 fb^{-1}. Data are analysed in the lepton plus jets final state, characterised by a high-transverse-momentum isolated electron or muon, large missing transverse momentum and multiple jets. Dedicated analyses are performed targeting three cases: a T quark with significant branching ratio to a W boson and a b quark ($T\bar{T} \rightarrow Wb$+X), and both a T quark and a B quark with significant branching ratio to a Higgs boson and a third generation quark ($T\bar{T} \rightarrow Ht$+X and $B\bar{B} \rightarrow Hb$+X respectively). The analyses exploit characteristic features of the signals to discriminate against the dominant background from top quark pair production, such as the high total transverse momenta of all final state objects, the presence of boosted hadronically-decaying W bosons, or the presence of Higgs bosons decaying into $b\bar{b}$, resulting in high b-jet multiplicity. No significant excess of events above the Standard Model expectation is observed, and 95% CL lower limits are derived on the masses of the vector-like T and B quarks under several branching ratio hypotheses assuming contributions from $T \rightarrow Wb$, Zt, Ht and $B \rightarrow Wt$, Zb, Hb decays. The 95% CL observed lower limits on the T quark mass range between 715 GeV and 950 GeV for all possible values of the branching ratios into the three decay modes, representing the most stringent constraints to date. Additionally, the most restrictive existing upper bounds on four-top-quark production are set in a number of new physics scenarios.

ATLAS-CONF-2015-012
20 March 2015

1. Introduction

The discovery of a new particle consistent with the Standard Model (SM) Higgs boson by the ATLAS [1] and CMS [2] collaborations was a major milestone in high-energy physics. However the underlying nature of electroweak symmetry breaking remains unknown. Naturalness arguments [3] require that quadratic divergences that arise from radiative corrections to the Higgs mass must be cancelled by some new mechanism in theories beyond the SM (BSM) in order to avoid fine-tuning. To that effect, several explanations have been proposed. In supersymmetry, the cancellation comes from the association of superpartners to the SM bosons and fermions. Alternatively, Little Higgs [4, 5] and Composite Higgs [6, 7] models introduce a spontaneously-broken global symmetry, with the Higgs boson emerging as a pseudo-Nambu-Goldstone boson [8]. Such models predict the existence of vector-like quarks, defined as colour-triplet spin-1/2 fermions whose left- and right-handed chiral components have the same transformation properties under the weak-isospin SU(2) gauge group [9, 10]. In these models vector-like quarks are expected to couple preferentially to third-generation quarks [9, 11] and they can have flavour-changing neutral current decays, in addition to the charged-current decays characteristic of chiral quarks. As a result, an up-type quark T with charge $+2/3$ can decay not only to a W boson and a b-quark, but also to a Higgs or Z boson and a top quark ($T \to Wb$, Zt, and Ht). Similarly, a down-type quark B with charge $-1/3$ can decay to a Higgs or Z boson and a b-quark, in addition to decaying to a W boson and a top quark ($B \to Wt$, Zb, and Hb). In order to be consistent with precision electroweak data, a small mass splitting between vector-like quarks belonging to the same $SU(2)$ multiplet is required [12], which forbids cascade decays such as $T \to WB$ and leaves direct decays into SM particles as the only possibility. Couplings between the vector-like quarks and the first and second quark generations, although not favoured, are not excluded [13, 14]. This leads to a rich phenomenology at the LHC, which the ATLAS and CMS collaborations are investigating.

Early searches for the pair production of exotic heavy quarks published by the ATLAS and CMS collaborations focused on individual decay modes assuming a 100% branching ratio. These include searches for $T\bar{T} \to W^+bW^-\bar{b}$ [15–18], $B\bar{B} \to ZbZ\bar{b}$ [19–21], and $B\bar{B} \to W^+tW^-\bar{t}$ [20, 22, 23]. The limits derived from these searches can not easily be applied to other branching ratio values, due to the potentially large expected signal contamination from mixed decay modes. A consistent treatment of those additional signal contributions is thus necessary to set quasi-model independent limits in the plane defined by the branching ratios to two of the decay modes[1] as a function of the heavy quark mass. The first search to consider simultaneously all three decay modes in the interpretation of results, performed by the ATLAS collaboration at $\sqrt{s} = 7$ TeV, primarily targeted the $T\bar{T} \to W^+bW^-\bar{b}$ process [24]. Using the full dataset collected at $\sqrt{s} = 8$ TeV, the ATLAS collaboration has recently published searches for heavy quarks decaying to a Z boson and a third generation quark [25], and searches for heavy quarks decaying predominantly to Wt in events with one lepton and jets [26] and in events with two same-sign or three leptons [27]. In the context of vector-like quarks, these searches are used to probe $T\bar{T}$ and $B\bar{B}$ production considering the three decay modes in the interpretation of the results. The CMS collaboration has published an inclusive search for $T\bar{T}$ production [28] resulting from the combination of several analyses in lepton plus jets and multilepton final states. This search sets 95% confidence level (CL) lower limits on the T quark mass ranging between 690 GeV and 780 GeV for all possible values of the branching ratios into the three possible decay modes.

The results presented in this paper complete the program of searches for pair production of vector-like

[1] The branching ratio to the third decay mode is fully determined by the requirement that the sum of branching ratios equals unity.

quarks decaying into third-generation quarks by the ATLAS collaboration using the dataset collected at $\sqrt{s} = 8$ TeV. Three separate searches are presented, all of them focused on the pair production of vector-like quarks in final states involving one isolated electron or muon, high missing transverse momentum and multiple jets. The first search, referred to as $T\bar{T} \to Wb$+X, is optimised for $T\bar{T}$ production with at least one $T \to Wb$ decay, where the resulting W boson acquires a high momentum from the large T-quark mass. The second search, referred to as $T\bar{T} \to Ht$+X, targets $T\bar{T}$ production with at least one $T \to Ht$ decay, with $H \to b\bar{b}$, resulting in events with high jet multiplicity and a large number of jets tagged as originating from b-quarks. The third search, referred to as $B\bar{B} \to Hb$+X, is instead focused on $B\bar{B}$ production with at least one $B \to Hb$ decay and $H \to b\bar{b}$, in events with the same final state signature probed by the $T\bar{T} \to Ht$+X search. In all three searches the isolated lepton and the high missing transverse momentum are provided by the leptonic decay of a W boson coming from the decay of a vector-like quark, a top quark, or a Higgs boson. Given its sensitivity to a wide range of models, the $T\bar{T} \to Ht$+X search is also used to search for a four-top-quark signal, both within the SM as well as in several BSM scenarios involving new heavy particles preferentially coupled to the top quark.

This paper is organised as follows. A brief description of the ATLAS detector is provided in Section 2. The object reconstruction, data sample, and event preselection are described in Sections 3 and 4. The signal and background modelling are discussed in Sections 5 and 6 respectively. The three searches are described in separate sections: $T\bar{T} \to Wb$+X in Section 7, $T\bar{T} \to Ht$+X in Section 8, and $B\bar{B} \to Hb$+X in Section 9. A discussion of the systematic uncertainties and the statistical analysis is provided in Sections 10 and 11 respectively. The results are presented in Section 12. Finally, the conclusions are given in Section 13.

2. ATLAS detector

The ATLAS detector [29] consists of the following main subsystems: an inner tracking system, electromagnetic and hadronic calorimeters, and a muon spectrometer. The inner detector provides tracking information from silicon pixel and microstrip detectors in the pseudorapidity[2] range $|\eta| < 2.5$ and from a straw-tube transition radiation tracker covering $|\eta| < 2.0$, all immersed in a 2 T magnetic field provided by a superconducting solenoid. The electromagnetic (EM) sampling calorimeter uses lead as the absorber material and liquid-argon (LAr) as the active medium, and is divided into barrel ($|\eta| < 1.475$) and end-cap ($1.375 < |\eta| < 3.2$) regions. Hadron calorimetry is also based on the sampling technique, with either scintillator tiles or LAr as active media, and with steel, copper, or tungsten as the absorber material. The calorimeters cover $|\eta| < 4.9$. The muon spectrometer measures the deflection of muons within $|\eta| < 2.7$ using multiple layers of high-precision tracking chambers located in a toroidal field of approximately 0.5 T and 1 T in the central and end-cap regions of ATLAS respectively. The muon spectrometer is also instrumented with separate trigger chambers covering $|\eta| < 2.4$. A three-level trigger system [30] is used to select interesting events. The first-level trigger is implemented in custom electronics and uses a subset of detector information to reduce the event rate to at most 75 kHz. This is followed by two software-based

[2] ATLAS uses a right-handed coordinate system with its origin at the nominal interaction point (IP) in the centre of the detector and the z-axis coinciding with the axis of the beam pipe. The x-axis points from the IP to the centre of the LHC ring, and the y-axis points upward. Cylindrical coordinates (r,ϕ) are used in the transverse plane, ϕ being the azimuthal angle around the beam pipe. The pseudorapidity is defined in terms of the polar angle θ as $\eta = -\ln\tan(\theta/2)$. For the purpose of the fiducial selection, this is calculated relative to the geometric centre of the detector; otherwise, it is relative to the reconstructed primary vertex of each event.

trigger levels exploiting the full detector information and yielding a typical recorded event rate of 400 Hz during 2012.

3. Object reconstruction

The main reconstructed objects considered in this search are electrons, muons, jets, b-jets and missing transverse momentum.

Electron candidates [31] are reconstructed from energy deposits (clusters) in the EM calorimeter that are associated to reconstructed tracks in the inner detector. They are required to have a transverse energy[3], E_{T}, greater than 25 GeV and $|\eta_{\mathrm{cluster}}| < 2.47$, where $|\eta_{\mathrm{cluster}}|$ is the pseudorapidity of the cluster associated with the electron candidate. Candidates in the calorimetry transition region $1.37 < |\eta_{\mathrm{cluster}}| < 1.52$ are excluded. Electrons are required to satisfy "tight" quality requirements [31], which include stringent selection requirements on calorimeter, tracking and combined variables that provide good separation between prompt electrons and jets. The longitudinal impact parameter of the electron track with respect to the selected event primary vertex (see Sect. 4), z_0, is required to be less than 2 mm. To reduce the background from non-prompt electrons resulting from semileptonic decays of b- or c-hadrons, and from jets with a high fraction of their energy deposited in the EM calorimeter, electron candidates must also satisfy calorimeter- and track-based isolation requirements. The calorimeter isolation variable is based on the energy sum of cells within a cone with radius $\Delta R = \sqrt{(\Delta\phi)^2 + (\Delta\eta)^2} = 0.2$ around the direction of each electron candidate, and an η-dependent requirement is made, giving an average efficiency of 90% for prompt electrons from Z boson decays. This energy sum excludes cells associated with the electron cluster and is corrected for leakage from the electron cluster itself and for energy deposits from additional pp interactions within the same bunch crossing ("pileup"). A further 90% efficient isolation requirement is made on the track transverse momentum (p_{T}) sum around the electron in a cone of radius $\Delta R = 0.3$.

Muon candidates [32, 33] are reconstructed from track segments in the various layers of the muon spectrometer and matched with tracks found in the inner detector. The final candidates are refitted using the complete track information from both detector systems and required to satisfy $p_{\mathrm{T}} > 25$ GeV and $|\eta| < 2.5$. Muons are required to have a hit pattern in the inner detector consistent with a well-reconstructed track to ensure good p_{T} resolution. The muon track longitudinal impact parameter with respect to the primary vertex, z_0, is required to be less than 2 mm. Muons are required to satisfy a p_{T}-dependent track-based isolation requirement: the scalar sum of the track p_{T} within a cone of variable radius $\Delta R = 10\ \mathrm{GeV}/p_{\mathrm{T}}^{\mu}$ around the muon (excluding the muon track itself) must be less than 5% of the muon p_{T} (p_{T}^{μ}). This requirement has good signal efficiency and background rejection even under high-pileup conditions, as well as in boosted configurations where the muon is close to a jet. For muons from W decays in simulated $t\bar{t}$ events the average efficiency of the isolation requirement is about 95%.

Jets are reconstructed with the anti-k_t algorithm [34–36] with a radius parameter $R = 0.4$ from calibrated topological clusters [37, 38] built from energy deposits in the calorimeters. Prior to jet finding, a local cluster calibration scheme [39] is applied to correct the topological cluster energies for the effects of non-compensation, dead material and out-of-cluster leakage. The corrections are obtained from simulations of charged and neutral particles. After energy calibration [40], jets are required to have $p_{\mathrm{T}} > 25$ GeV and $|\eta| < 2.5$. To reduce the contamination due to pileup jets, a selection on the so-called "jet vertex fraction"

[3] The electron transverse energy is defined as $E_{\mathrm{T}} = E_{\mathrm{cluster}}/\cosh\eta_{\mathrm{track}}$, where E_{cluster} is the energy of the electron cluster in the calorimeter and η_{track} is the pseudorapidity of its associated track.

(JVF) variable above 0.5 is applied to jets with $p_{\mathrm{T}} < 50$ GeV and $|\eta| < 2.4$. This requirement ensures that at least 50% of the scalar sum of the p_{T} of tracks matched to the jet comes from tracks originating from the primary vertex. During jet reconstruction, no distinction is made between identified electrons and jet energy deposits. Therefore, if any of the jets lie within $\Delta R = 0.2$ of a selected electron, the closest jet is discarded in order to avoid double-counting of electrons as jets. As the last step, any electron or muon within ΔR of 0.4 of selected jets is discarded.

Jets are identified as originating from the hadronisation of a b-quark (b-tagged) via an algorithm [41, 42] that uses multivariate techniques to combine information from the impact parameters of displaced tracks as well as topological properties of secondary and tertiary decay vertices reconstructed within the jet. Each jet is assigned a value for the multivariate b-tagging discriminant and is considered b-tagged if this value is above a given threshold. The threshold used for this search corresponds to 70% efficiency to tag a b-quark jet, with a light-jet rejection factor of ~130 and a charm-jet rejection factor of 5, as determined for jets with $p_{\mathrm{T}} > 20$ GeV and $|\eta| < 2.5$ in simulated $t\bar{t}$ events.

The missing transverse momentum ($E_{\mathrm{T}}^{\mathrm{miss}}$) is constructed [43] from the vector sum of all calorimeter energy deposits[4] contained in topological clusters. All topological cluster energies are corrected using the local cluster calibration scheme discussed above. Those topological clusters associated to a high-p_{T} object (e.g. jet or electron) are further calibrated using their respective energy corrections. In addition, contributions from the p_{T} of selected muons are included in the calculation of $E_{\mathrm{T}}^{\mathrm{miss}}$.

4. Data sample and event preselection

This search is based on pp collision data at $\sqrt{s} = 8$ TeV collected by the ATLAS experiment between April and December 2012. Only events recorded with a single-electron or single-muon trigger under stable beam conditions and for which all detector subsystems were operational are considered. The corresponding integrated luminosity is 20.3 ± 0.6 fb^{-1} [44]. Single-lepton triggers with different p_{T} thresholds are combined in a logical OR in order to increase the overall efficiency. The p_{T} thresholds are 24 or 60 GeV for the electron triggers and 24 or 36 GeV for the muon triggers. The triggers with the lower p_{T} threshold include isolation requirements on the candidate lepton, resulting in inefficiencies at high p_{T} that are recovered by the triggers with higher p_{T} threshold. Events satisfying the trigger selection are required to have at least one reconstructed vertex with at least five associated tracks, consistent with originating from the beam collision region in the x–y plane. If more than one vertex is found, the hard-scatter primary vertex is taken to be the one which has the largest sum of the squared transverse momenta of its associated tracks.

Events are required to have exactly one reconstructed electron or muon and at least four jets satisfying the quality and kinematic criteria discussed in Section 3. The selected lepton is required to match within $\Delta R < 0.15$ the lepton reconstructed by the trigger. The background from multijet production is suppressed by a requirement on $E_{\mathrm{T}}^{\mathrm{miss}}$ as well as on the transverse mass of the lepton and $E_{\mathrm{T}}^{\mathrm{miss}}$ ($m_{\mathrm{T}}^{\mathrm{W}}$).[5] For both lepton selections the requirements are $E_{\mathrm{T}}^{\mathrm{miss}} > 20$ GeV and $E_{\mathrm{T}}^{\mathrm{miss}} + m_{\mathrm{T}}^{\mathrm{W}} > 60$ GeV. Further suppression

[4] Each cluster in the calorimeter is considered a massless object and is assigned the four-momentum $(E_{\mathrm{cluster}}, \vec{p}_{\mathrm{cluster}})$, where E_{cluster} is the measured energy and $\vec{p}_{\mathrm{cluster}}$ is a vector of magnitude E_{cluster} directed from $(x, y, z) = (0, 0, 0)$ to the centre of the cluster.

[5] $m_{\mathrm{T}}^{\mathrm{W}} = \sqrt{2 p_{\mathrm{T}}^{\ell} E_{\mathrm{T}}^{\mathrm{miss}} (1 - \cos\Delta\phi)}$, where p_{T}^{ℓ} is the transverse momentum (energy) of the muon (electron) and $\Delta\phi$ is the azimuthal angle separation between the lepton and the direction of the missing transverse momentum.

of the background not including b-quark jets is achieved by requiring at least one b-tagged jet in the $T\bar{T} \to Wb$+X search, and at least two b-tagged jets in the $T\bar{T} \to Ht$+X and $B\bar{B} \to Hb$+X searches. In the following, events satisfying either the electron or muon selections will be combined and treated as a single analysis channel.

5. Signal modeling

This section describes the different signal scenarios considered in the interpretation of the results, together with details on how they are modelled in the analysis.

5.1. Vector-like quark pair production

Vector-like quarks with mass below approximately 1 TeV are dominantly produced in pairs via the strong interaction in pp collisions at $\sqrt{s} = 8$ TeV. The predicted cross section ranges from 5.3 pb for a quark mass of 350 GeV to 3.3 fb for a quark mass of 1000 GeV, with an uncertainty that increases from 8% to 14% over this mass range. This cross section is independent of the electroweak quantum numbers of the new heavy quark and just depends on its mass. It was computed using Top++ v2.0 [45] at next-to-next-to leading order (NNLO) in QCD, including resummation of next-to-next-to-leading logarithmic (NNLL) soft gluon terms [46–50], and using the MSTW 2008 NNLO [51, 52] set of parton distribution functions (PDF). Theoretical uncertainties include factorisation and renormalisation scale variations, as well as uncertainties on the PDF and α_S. The latter two represent the largest contribution to the overall theoretical uncertainty on the cross section and were calculated using the PDF4LHC prescription [53] with the MSTW 2008 68% CL NNLO, CT10 NNLO [54, 55] and NNPDF2.3 5f FFN [56] PDF sets.

As discussed previously, vector-like quarks can couple preferentially to third-generation quarks, as the mixing between weak eigenstates of the same electric charge is proportional to the mass of the SM quark [9, 11], and thus present a rich phenomenology. In particular, a vector-like quark has neutral-current tree-level decays to a Z or H boson plus an SM quark, in addition to the charged-current decay mode to a W boson and an SM quark, which is the only decay mode chiral quarks can have. Figure 1 depicts representative Feynman diagrams for the signals probed by the searches discussed in this paper. The branching ratios to each of these decay modes vary as a function of the heavy quark mass and depend on its weak-isospin ($SU(2)$) quantum numbers [10]. Figure 2(a) shows the branching ratios as a function of mass for a T quark for the $SU(2)$ singlet and doublet hypotheses.[6] In the case of a singlet, all three decay modes have sizeable branching ratios, while the charged-current decay mode $T \to Wb$ is absent in the doublet cases. The doublet prediction is valid for an (X,T) doublet, where the charge of the X quark is +5/3, as well as a (T,B) doublet when a mixing assumption of $V_{Tb} \ll V_{tB}$ is made, where V_{ij} are the elements of a generalised Cabibbo-Kobayashi-Masukawa matrix [10]. Similarly, Fig. 2(b) shows the branching ratios as a function of mass for a B quark for the singlet and doublet hypotheses. In the case of a (T,B) doublet with the mixing assumption $V_{Tb} \ll V_{tB}$, $BR(B \to Wt) = 1$, while such a decay mode is absent for the (B,Y) doublet case, where the charge of the Y quark is $-4/3$. The Y quark is equivalent to a chiral quark since it only has charged-current decays, $Y \to W^- b$.

[6] The branching ratios in Fig. 2 are valid for small mixing between the new heavy quark and the third-generation quark [10–12].

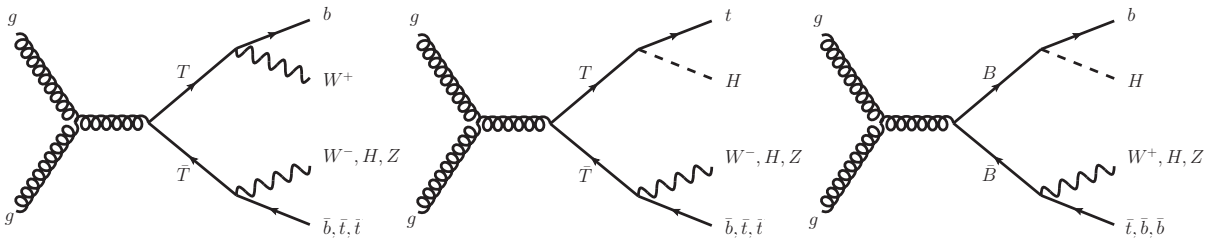

(a) (b) (c)

Figure 1: Representative leading-order Feynman diagrams for $T\bar{T}$ production probed by (a) the $T\bar{T} \to Wb$+X search and (b) the $T\bar{T} \to Ht$+X search, and (c) for $B\bar{B}$ production probed by the $B\bar{B} \to Hb$+X search.

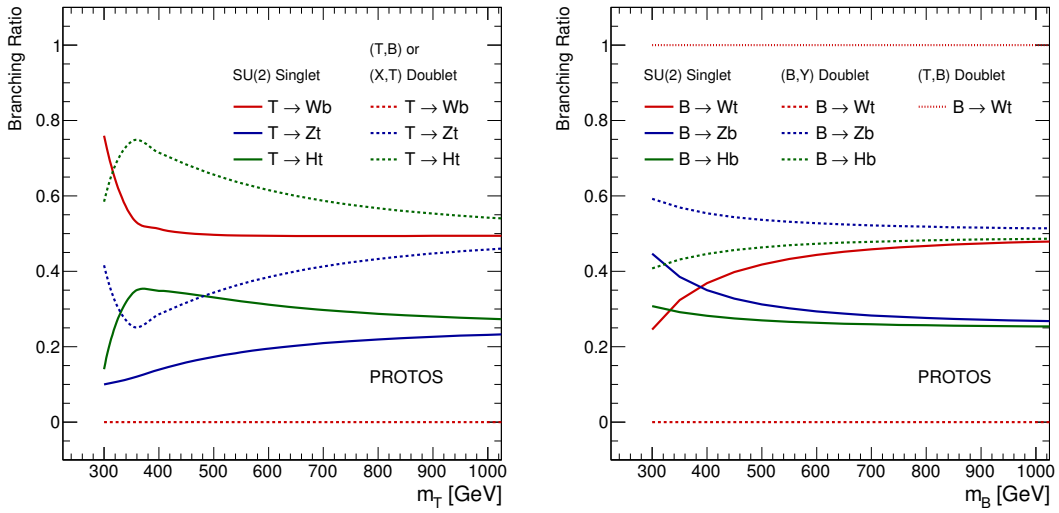

(a) (b)

Figure 2: Branching ratios for the different decay modes as a function of heavy-quark mass in the case of (a) a vector-like T quark and (b) a vector-like B quark, as computed with Protos. In both cases the branching ratios are provided for an SU(2) singlet and two different SU(2) doublet scenarios.

Simulated samples of $T\bar{T}$ and $B\bar{B}$ are generated with the leading-order (LO) generator Protos v2.2 [57] using the MSTW 2008 LO PDF set and interfaced to Pythia 6.426 [58] for parton shower and fragmentation. The AUET2B [59, 60] set of optimised parameters for the underlying event (UE) description, referred to as "UE tune", is used. The vector-like quarks are forced to decay with a branching ratio of 1/3 to each of the three modes (W, Z, H). Arbitrary sets of branching ratios consistent with the three decay modes summing to unity are obtained by reweighting the samples using particle-level information. Samples are generated assuming singlet couplings and for heavy quark masses between 350 GeV and 1100 GeV in steps of 50 GeV. Additional samples were produced at two mass points (350 GeV and 600 GeV) assuming doublet couplings in order to confirm that kinematic differences arising from the different chirality of singlet and doublet couplings are negligible in this analysis. In all simulated samples (both signal and background) used in this search, the top quark and SM Higgs boson masses are set to 172.5 GeV and 125 GeV respectively. The samples are normalised using the Top++ cross-section predictions discussed above.

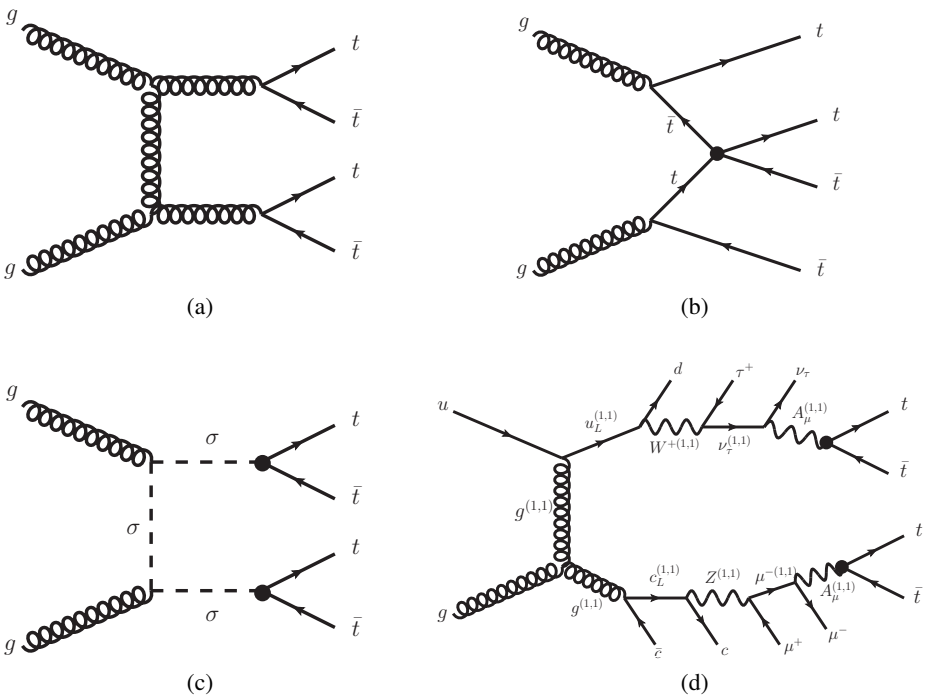

Figure 3: Representative leading-order Feynman diagrams for four-top-quark production within (a) the SM and several beyond-the-SM scenarios (see text for details): (b) via an effective four-top-quark interaction in an effective field theory model, (c) via scalar-gluon-pair production, and (d) via cascade decays from Kaluza-Klein excitations in an universal extra dimensions model with two extra dimensions compactified under the real projective plane.

5.2. Four-top-quark production

The production cross section for four-top-quark events in the SM is very small ($\sigma_{t\bar{t}t\bar{t}} \simeq 1$ fb at $\sqrt{s} = 8$ TeV) [61, 62], but it can be significantly enhanced in several BSM scenarios. Figure 3 depicts representative LO Feynman diagrams for four-top-quark production within the SM and the BSM scenarios considered in this paper. A class of models involving new heavy vector particles strongly coupled to the right-handed top quark, such as top quark compositeness [63–65] or Randall-Sundrum extra dimensions [66], can be described via an effective field theory (EFT) involving a four-fermion contact interaction [67] (Fig. 3(b)). The Lagrangian assumed is $\mathcal{L}_{4t} = \frac{|C_{4t}|}{\Lambda^2}(\bar{t}_R\gamma^\mu t_R)(\bar{t}_R\gamma_\mu t_R)$, where t_R is the right-handed top quark spinor, γ_μ are the Dirac matrices, C_{4t} is the coupling constant, and Λ is the energy scale of new physics. Only the contact interaction operator with right-handed top quarks is considered as left-handed operators are already strongly constrained by electroweak precision data [68].

In addition, two specific models are considered involving new heavy particles: sgluon pair production and an Universal Extra Dimensions (UED) model. Sgluons are colour-adjoint scalars, denoted as σ, that appear in several extensions of the SM, both supersymmetric [69, 70] and non-supersymmetric [71–74]. The dominant production mode at the LHC is in pairs via the strong interaction, $gg \to \sigma\sigma$. For sgluon masses above twice the top-quark mass, the dominant decay mode is into $t\bar{t}$, giving rise to a four-top-quark final state (Fig. 3(c)). The UED model considered has two extra dimensions that are compactified under the real projective plane (2UED/RPP) [75], leading to a discretisation of the momenta along their directions. A tier of Kaluza-Klein towers is labelled by two integers, k and ℓ, referred to as "tier (k,ℓ)".

Within a given tier, the squared masses of the particles are given at leading order by $m^2 = k^2/R_4^2 + \ell^2/R_5^2$, where πR_4 and πR_5 are the size of the two extra dimensions. The model is parameterised by R_4 and R_5 or, alternatively, by $m_{KK} = 1/R_4$ and $\xi = R_4/R_5$. Four-top-quark production can arise from tier (1,1), where particles from this tier have to be pair produced because of symmetries of the model. Then they chain-decay to the lightest particle of this tier, the heavy photon $A^{(1,1)}$, by emitting SM particles (Fig. 3(d)). The branching ratios of $A^{(1,1)}$ into SM particles are not predicted by the model, although the decay into $t\bar{t}$ is expected to be dominant [76]. Four-top-quark events can also arise from tiers (2,0) and (0,2) via a similar mechanism. In this case the expected cross section for four-top-quark production is reduced compared to that from tier (1,1) since each state in tiers (2,0) and (0,2) can decay directly into a pair of SM particles or into a pair of states in tiers (1,0) or (0,1) via bulk interactions, resulting into smaller branching ratios for decay into $t\bar{t}$ [76]. In the following, when considering four-top-quark production from a given tier, it will be assumed that the A photon in that tier decays with 100% branching ratio into $t\bar{t}$ while A photons from other tiers cannot decay into $t\bar{t}$. Observations of dark matter relic abundance prefer values of m_{KK} between 600 GeV and 1200 GeV [77].

Simulated samples of four-top-quark production within the SM, within a EFT model, and within the 2UED/RPP model, are generated with the MADGRAPH5 1.3.33 [78] LO generator and the MSTW 2008 PDF set, interfaced to PYTHIA 8.1 [79] and the A2 UE tune [59, 60]. In the case of the 2UED/RPP model, samples are generated for four different values of m_{KK} (600, 800, 1000 and 1200 GeV) and the BRIDGE [80] generator is used to decay the pair-produced excitations from tier (1,1) generated by MADGRAPH5. Samples of four-top-quark production via sgluon pairs are generated with PYTHIA 6.426 with the CTEQ6L1 [81] PDF set and the AUET2B UE tune, for seven different values of the sgluon mass between 350 GeV and 1250 GeV, and normalised to the NLO theoretical cross section [82].

Events from minimum bias interactions are simulated with the PYTHIA 8.1 generator with the MSTW 2008 LO PDF set and the A2 tune. They are overlaid on the simulated signal events according to the luminosity profile of the recorded data. The contributions from these pileup interactions are modelled both within the same bunch crossing of the hard-scattering process and in neighbouring bunch crossings. Finally, the generated samples are processed through a simulation [83] of the detector geometry and response using GEANT4 [84] with a fast simulation of the calorimeter response [83]. All samples are processed through the same reconstruction software as the data. Simulated events are corrected so that the object identification efficiencies, energy scales and energy resolutions match those determined from data control samples.

6. Background modelling

After event preselection, the main background is $t\bar{t}$+jets production, with the production of a W boson in association with jets (W+jets) and multijet events contributing to a lesser extent. Small contributions arise from single top quark, Z+jets and diboson (WW, WZ, ZZ) production, as well as from the associated production of a vector boson or a Higgs boson and a $t\bar{t}$ pair ($t\bar{t}V$ and $t\bar{t}H$). Multijet events contribute to the selected sample via the misidentification of a jet or a photon as an electron or via the presence of a non-prompt lepton, e.g. from a semileptonic b- or c-hadron decay; the corresponding yield is estimated via data-driven methods. The rest of background contributions are estimated from the simulation and normalised to their theoretical cross sections. In the case of the $t\bar{t}$+jets and W/Z+jets background predictions, further corrections to improve the agreement between the data and the simulation are applied, as discussed in Sects. 6.1 and 6.2 respectively.

All simulated background samples utilise Photos 2.15 [85] to simulate photon radiation and Tauola 1.20 [86] to simulate τ decays. Similarly to the signal samples, they include also a simulation of pileup interactions, and are processed through a full Geant4 detector simulation and the same reconstruction software as the data. Further details on the modelling of each of the backgrounds are provided below.

6.1. $t\bar{t}$+jets background

Simulated samples of $t\bar{t}$+jets are generated with the next-to-leading order (NLO) generator Powheg r2129 [87–89] using the CT10 PDF set [54]. The nominal sample is interfaced to Pythia 6.425 [58] with the CTEQ6L1 PDF set and the Perugia2011C UE tune [90]. An alternative sample, used to study the uncertainty related to the fragmentation model, is interfaced to Herwig v6.520 [91] with the CTEQ6L1 PDF set and Jimmy v4.31 [92] to simulate the UE. The $t\bar{t}$+jets samples are normalised to the theoretical cross section obtained with Top++, performed at NNLO in QCD and including resummation of NNLL soft gluon terms.

The $t\bar{t}$+jets samples are generated inclusively, but events are categorised depending on the flavour content of additional particle jets in the event (i.e. jets not originating from the decay of the $t\bar{t}$ system). Particle jets are reconstructed with the anti-k_t algorithm with a radius parameter $R = 0.4$ and are required to have $p_{\mathrm{T}} > 15$ GeV and $|\eta| < 2.5$. Events where at least one such particle jet is matched within $\Delta R < 0.4$ to a b hadron with $p_{\mathrm{T}} > 5$ GeV not originating from a top-quark decay are labelled as $t\bar{t} + b\bar{b}$ events. Similarly, events where at least one such particle jet is matched within $\Delta R < 0.4$ to a c hadron with $p_{\mathrm{T}} > 5$ GeV not originating from a W boson decay, that are not labelled already as $t\bar{t} + b\bar{b}$, are labelled as $t\bar{t} + c\bar{c}$ events. Events labelled as either $t\bar{t} + b\bar{b}$ or $t\bar{t} + c\bar{c}$ will generically be referred to as $t\bar{t}$+HF events, where HF stands for "heavy flavour". The remaining events are labelled as $t\bar{t}$+light jet events, including those with no additional jets. In Powheg+Pythia the modelling of $t\bar{t}$+HF is via the parton-shower evolution. To study uncertainties related to this simplified description, an alternative $t\bar{t}$+jets sample is generated with Madgraph5 1.5.11 using the CT10 PDF set. It includes tree-level diagrams with up to three additional partons (including b- and c-quarks) and is interfaced to Pythia 6.425.

Since the best possible modelling of the $t\bar{t}$+jets background is a key aspect of these searches, a correction is applied to simulated $t\bar{t}$ events in Powheg+Pythia based on the ratio of measured differential cross sections at $\sqrt{s} = 7$ TeV between data and the simulation as a function of top quark p_{T} and $t\bar{t}$ system p_{T} [93]. The stability of the ratio between $\sqrt{s} = 7$ TeV and $\sqrt{s} = 8$ TeV was studied to support the usage of $\sqrt{s} = 7$ TeV data to correct the simulation at $\sqrt{s} = 8$ TeV. This correction significantly improves the agreement between simulation and data in distributions such as the jet multiplicity and the p_{T} of decay products of the $t\bar{t}$ system. This correction is applied only to $t\bar{t}$+light jets and $t\bar{t} + c\bar{c}$ events. The modelling of the $t\bar{t} + b\bar{b}$ background, particularly important for the Ht/Hb+X searches, is improved by reweighting the Powheg+Pythia prediction to a NLO prediction of $t\bar{t} + b\bar{b}$ including parton-showering [94], based on Sherpa+OpenLoops [95, 96] using the CT10 PDF set. This reweighting is performed for different topologies of $t\bar{t} + b\bar{b}$ in such a way that the inter-normalisation of each of the categories and the relevant kinematics distributions are at NLO accuracy. More details on the modelling of the $t\bar{t}$+jets background can be found in Ref. [97].

6.2. W/Z+jets background

Samples of W/Z+jets events are generated with up to five additional partons using the ALPGEN v2.14 [98] LO generator and the CTEQ6L1 PDF set, interfaced to PYTHIA v6.426 for parton showering and fragmentation. To avoid double-counting of partonic configurations generated by both the matrix-element calculation and the parton shower, a parton-jet matching scheme ("MLM matching") [99] is employed. The W+jets samples are generated separately for W+light jets, $Wb\bar{b}$+jets, $Wc\bar{c}$+jets, and Wc+jets. The Z+jets samples are generated separately for Z+light jets, $Zb\bar{b}$+jets, and $Zc\bar{c}$+jets. Overlap between $W/ZQ\bar{Q}$+jets ($Q = b, c$) events generated from the matrix element calculation and those generated from parton-shower evolution in the W/Z+light jets samples is avoided via an algorithm based on the angular separation between the extra heavy quarks: if $\Delta R(Q,\bar{Q}) > 0.4$, the matrix-element prediction is used, otherwise the parton-shower prediction is used. Both W+jets and Z+jets backgrounds are normalised to their inclusive NNLO theoretical cross sections [100]. Further corrections are applied to W/Z+jets events in order to better describe data in the preselected sample. Scale factors for each of the W+jets categories ($Wb\bar{b}$+jets, $Wc\bar{c}$+jets, Wc+jets and W+light jets) are derived for events with one lepton and at least four jets by simultaneously analysing six different event categories, defined by the b-tag multiplicity (0, 1 and $\geq$2) and the sign of the lepton charge. The b-tag multiplicity provides information about the heavy flavour composition of the W+jets background, while the lepton charge is used to determine the normalisation of each component, exploiting the expected charge asymmetry for W+jets production in pp collisions as predicted by ALPGEN. In the case of Z+jets events, a correction to the heavy-flavour fraction has been derived to reproduce the relative rates of Z+2 jets events with 0 and 1 b-tagged jets observed in data. In addition, the Z p_{T} spectrum has been compared between data and the simulation in Z+2 jets events, and a reweighting function has been derived in order to improve the modelling.

6.3. Other simulated background

Samples of single top quark backgrounds corresponding to the t-channel, s-channel and Wt production mechanisms are generated with POWHEG using the CT10 PDF set and interfaced to PYTHIA 6.425 with the CTEQ6L1 PDF set and the Perugia2011C UE tune. Overlaps between the $t\bar{t}$ and Wt final states are removed using the "diagram removal" scheme [101]. The single top quark samples are normalised to the approximate NNLO theoretical cross sections [102–104] using the MSTW 2008 NNLO PDF set.

The $WW/WZ/ZZ$+jets samples are generated with up to three additional partons using ALPGEN v2.13 and the CTEQ6L1 PDF set, interfaced to HERWIG v6.520 and JIMMY v4.31 for parton showering, fragmentation and UE modelling, and are normalised to their NLO theoretical cross sections [105]. The WW+jets samples require at least one of the W bosons to decay leptonically, while the WZ/ZZ+jets require one Z boson to decay leptonically, with the other boson decaying inclusively. Additionally, WZ+jets samples requiring the W and Z bosons to decay leptonically and hadronically respectively, are generated with up to three additional partons (including massive b and c quarks) using SHERPA v1.4.1 and the CT10 PDF set.

Samples of $t\bar{t}V$ ($V = W, Z$), including $t\bar{t}WW$, are generated with up to two additional partons using MADGRAPH5 1.3.28 with the CTEQ6L1 PDF set, and interfaced to PYTHIA 6.425 with the AUET2B UE tune. A sample of $t\bar{t}H$ is generated with the POWHEL framework, which combines the POWHEG-BOX generator and NLO matrix elements obtained from the HELAC-Oneloop package [106]. The sample is generated using the NLO CT10 PDF set. Showering is performed with PYTHIA 8.1 using the CTEQ6L1 PDF set and the AU2 UE tune [59, 60]. Inclusive decays for the Higgs boson are assumed in the generation

of the $t\bar{t}H$ sample. The $t\bar{t}V$ samples are normalised to the NLO cross section predictions [107, 108], while the $t\bar{t}H$ sample is normalised to the NLO cross section [109–112] and Higgs decay branching ratios [113–116] collected in Ref. [117].

6.4. Multijet background

Multijet events can enter the selected data sample through several production and mis-reconstruction mechanisms. In the electron channel, the multijet background consists of both non-prompt electrons and mis-identified photons (e.g. with a conversion into an e^+e^- pair) or jets with a high fraction of their energy deposited in the EM calorimeter. In the muon channel, the background contributed by multijet events is predominantly due to final states with non-prompt muons, such as those from semileptonic b- or c-hadron decays.

The multijet background normalisation and shape are estimated directly from data by using the "Matrix Method" (MM) technique [118]. The MM exploits differences in lepton identification-related properties between prompt, isolated leptons from W and Z boson decays (referred to as "real leptons" below) and those where the leptons are either non-isolated or result from the mis-identification of photons or jets (referred to as "fake leptons" below). For this purpose, two samples are defined after imposing the final kinematic selection criteria, differing only in the lepton identification criteria: a "tight" sample and a "loose" sample, the former being a subset of the latter. The tight selection employs the final lepton identification criteria used in the analysis. For the loose selection the lepton isolation requirements are omitted. The method assumes that the number of selected events in each sample (N^{loose} and N^{tight}) can be expressed as a linear combination of the numbers of events with real and fake leptons, so that the number of multijet events in the tight sample is given by $N_{\text{MJ}}^{\text{tight}} = \frac{\epsilon_{\text{fake}}}{\epsilon_{\text{real}}-\epsilon_{\text{fake}}}(\epsilon_{\text{real}}N^{\text{loose}} - N^{\text{tight}})$ where ϵ_{real} (ϵ_{fake}) represents the probability for a real (fake) lepton that satisfies the loose criteria to also satisfy the tight ones. Both probabilities are measured in data control samples. To measure ϵ_{real}, samples enriched in real leptons from W bosons decays are selected by requiring high $E_{\text{T}}^{\text{miss}}$ or m_{T}^{W}. The average ϵ_{real} is ~0.75 (~0.98) in the electron (muon) channel. To measure ϵ_{fake}, samples enriched in multijet background are selected by requiring either low $E_{\text{T}}^{\text{miss}}$ (electron channel) or high impact parameter significance for the lepton track (muon channel). The average ϵ_{fake} value is ~0.35 (~0.20) in the electron (muon) channel. Dependencies of ϵ_{real} and ϵ_{fake} on quantities such as lepton p_{T} and η, ΔR between the lepton and the closest jet, or number of b-tagged jets, are parameterised in order to obtain a more accurate estimate.

7. Search for $T\bar{T} \to Wb$+X production

This search is sensitive to $T\bar{T}$ production where at least one of the T quarks decays into a W boson and a b quark, although it is particularly optimised for $T\bar{T} \to W^+bW^-\bar{b}$ events. One of the W bosons present in the final state is then required to decay leptonically. After the preselection described in Section 4, further background suppression is achieved by applying requirements aimed at exploiting the distinct kinematic features of the signal. The large T quark mass results in energetic W bosons and b quarks in the final state with large angular separation between them, while the decay products from the boosted W bosons have small angular separation. The combination of these properties is very effective in distinguishing the dominant $t\bar{t}$ background since $t\bar{t}$ events with boosted W boson configurations are rare and are typically characterised by a small angular separation between the W boson and the b quark from the top-quark decay.

To take advantage of these properties, it is necessary to identify the hadronically-decaying W boson (W_{had}) as well as the b-jets in the event. The candidate b-jets are defined as the two jets with the highest b-tag discriminant value, although only one of them is explicitly required to be b-tagged in the event selection. Two types of W_{had} candidates are defined, $W_{\text{had}}^{\text{type I}}$ and $W_{\text{had}}^{\text{type II}}$, depending on the angular separation between their decay products. $W_{\text{had}}^{\text{type I}}$ candidates correspond to boosted W bosons, where the quarks from the W-boson decay have small angular separation between them and are reconstructed as a single jet. $W_{\text{had}}^{\text{type II}}$ candidates correspond to W bosons where the two quarks from the W boson decay are reconstructed as separate jets. In the construction of both types of W_{had} candidates, the two candidate b-jets are excluded from consideration.

A $W_{\text{had}}^{\text{type I}}$ candidate is defined as a single jet with $p_{\text{T}} > 400$ GeV, which is the typical p_{T} above which the decay products from a W boson would have an angular separation $\Delta R \leq R_{\text{cone}} = 0.4$. A $W_{\text{had}}^{\text{type II}}$ candidate is defined as a dijet system with $p_{\text{T}} > 250$ GeV, angular separation $\Delta R(j,j) < 0.8$ and mass within the range of 60–120 GeV. The asymmetric window about the W-boson mass value is chosen in order to increase the acceptance for hadronically-decaying Z bosons from $T\bar{T} \to WbZt$ events. Any jets satisfying the $W_{\text{had}}^{\text{type I}}$ requirements are excluded from consideration to form $W_{\text{had}}^{\text{type II}}$ candidates. The leptonically-decaying W boson (W_{lep}) is reconstructed using the lepton and $E_{\text{T}}^{\text{miss}}$, which is taken as a measurement of the neutrino p_{T}. Requiring that the invariant mass of the lepton–neutrino system equals the nominal W boson mass allows reconstruction of the neutrino longitudinal momentum up to a two-fold ambiguity. If two solutions exist, they are both considered. If no real solution exists, the neutrino pseudorapidity is set equal to that of the lepton, since in the kinematic regime of interest the decay products of the W boson tend to be collinear.

Selection	Requirements
Preselection	One electron or muon $E_{\text{T}}^{\text{miss}} > 20$ GeV, $E_{\text{T}}^{\text{miss}} + m_{\text{T}} > 60$ GeV $\geq$4 jets, $\geq$1 b-tagged jets
Loose selection	Preselection $\geq$1 W_{had} candidate (type I or type II) $H_{\text{T}} > 800$ GeV $p_{\text{T}}(b_1) > 160$ GeV, $p_{\text{T}}(b_2) > 110$ GeV (type I) or $p_{\text{T}}(b_2) > 80$ GeV (type II) $\Delta R(\ell,\nu) < 0.8$ (type I) or $\Delta R(\ell,\nu) < 1.2$ (type II)
Tight selection	Loose selection $\min(\Delta R(\ell,b_{1,2})) > 1.4$, $\min(\Delta R(W_{\text{had}},b_{1,2})) > 1.4$ $\Delta R(b_1,b_2) > 1.0$ (type I) or $\Delta R(b_1,b_2) > 0.8$ (type II) $\Delta m < 250$ GeV (type I)

Table 1: Summary of event selection requirements for the $T\bar{T} \to Wb$+X analysis (see text for details).

Table 1 summarises the event selection requirements. Two selections, "loose" and "tight", are defined, with the latter being more restrictive than the former and representing the final selection. As discussed below, the loose selection is used to validate the background modelling in a kinematic regime close to the final selection. The loose selection considers preselected events with at least one $W_{\text{had}}^{\text{type I}}$ or $W_{\text{had}}^{\text{type II}}$ candidate. If multiple W_{had} candidates are found in a given event, the one with the highest p_{T} is chosen.

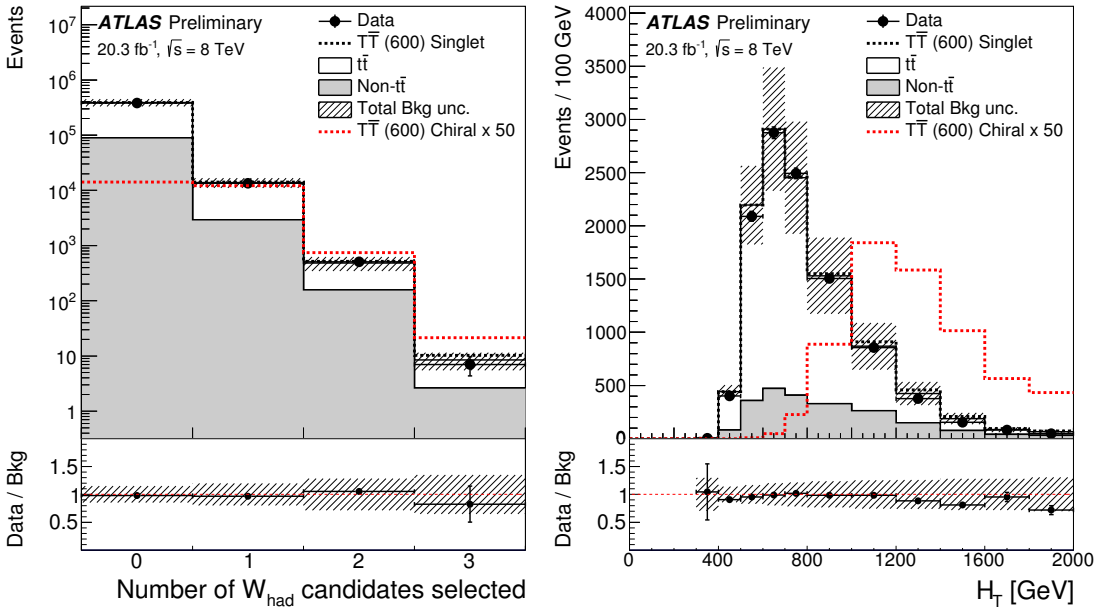

(a) (b)

Figure 4: Distribution of (a) the number of hadronically-decaying W boson (W_{had}) candidates after preselection requirements, and (b) the scalar sum of the transverse momenta of the lepton, the selected jets and the missing transverse momentum (H_{T}) after preselection and $\geq$1 W_{had} candidate requirements. The data (solid black points) are compared to the SM prediction (stacked histograms). The contributions from backgrounds other than $t\bar{t}$ are combined into a single background source referred to as "Non-$t\bar{t}$". The total uncertainty on the background estimation is shown as a black hashed band. The expected contribution from a chiral fourth-generation T quark with mass $m_T = 600$ GeV, multiplied by a factor of 50, is also shown (red dashed histogram), The lower panel shows the ratio of data to the SM prediction. The overflow has been added to the last bin.

Figure 4(a) shows the distribution of number of W_{had} candidates after preselection and prior to the requirement on this variable itself. The events must satisfy $H_{\text{T}} > 800$ GeV, where H_{T} is the scalar sum of the lepton p_{T}, $E_{\text{T}}^{\text{miss}}$ and the p_{T} of the selected jets. The H_{T} distribution peaks at $\sim 2m_T$ for signal events, which makes the $H_{\text{T}} > 800$ GeV requirement particularly efficient for signal with $m_T \gtrsim 400$ GeV, while rejecting a large fraction of the background. Figure 4(b) shows the distribution of H_{T} after the requirement of $\geq$1 W_{had} candidate and prior to the $H_{\text{T}} > 800$ GeV requirement. In addition, the highest-p_{T} b-jet candidate (b_1) and the next-to-highest-p_{T} b-jet candidate (b_2) are required to have $p_{\text{T}}(b_1) > 160$ GeV and $p_{\text{T}}(b_2) > 110\,(80)$ GeV respectively, in the case of a $W_{\text{had}}^{\text{type I}}$ ($W_{\text{had}}^{\text{type II}}$) candidate. Finally, the angular separation between the lepton and the reconstructed neutrino is required to satisfy $\Delta R(\ell,\nu) < 0.8\,(1.2)$ in case of a $W_{\text{had}}^{\text{type I}}$ ($W_{\text{had}}^{\text{type II}}$) candidate. Figure 5(a) shows the distributions of $\Delta R(\ell,\nu)$ after all previous requirements and prior to the $\Delta R(\ell,\nu)$ requirement.

The tight selection adds further requirements that are particularly effective at suppressing $t\bar{t}$ background. First, a large angular separation between the W bosons and the b-jets from the top-quark decay is required: $\min(\Delta R(\ell, b_{1,2})) > 1.4$ and $\min(\Delta R(W_{\text{had}}, b_{1,2})) > 1.4$. Figure 5(b) shows the distributions of $\min(\Delta R(\ell, b_{1,2}))$ after loose selection and prior to the $\min(\Delta R(\ell, b_{1,2})) > 1.4$ requirement. Finally, additional requirements are made on $\Delta R(b_1, b_2) > 1.0\,(0.8)$ in the case of a $W_{\text{had}}^{\text{type I}}$ ($W_{\text{had}}^{\text{type II}}$) candidate and $\Delta m < 250$ GeV only in the case of a $W_{\text{had}}^{\text{type I}}$ candidate, where $\Delta m = \min(|m_{\text{reco}}^{\text{lep}} - m_{\text{reco}}^{\text{had}}|)$ is the smallest

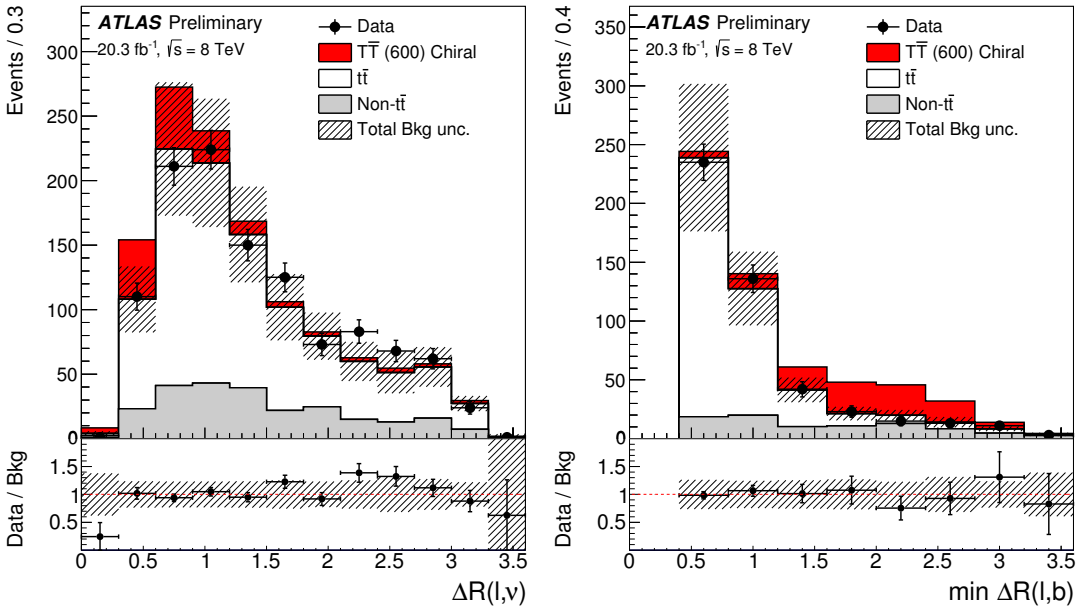

(a) (b)

Figure 5: Distribution of (a) the angular separation between the lepton and the reconstructed neutrino ($\Delta R(\ell,\nu)$), and (b) the minimum angular separation between the lepton and the two candidate b-jets ($\min(\Delta R(\ell,b_{1,2}))$). The selections made include all previous requirements except for the requirement on each of these variables (see text for details). The data (solid black points) are compared to the SM prediction (stacked histograms). The contributions from backgrounds other than $t\bar{t}$ are combined into a single background source referred to as "Non-$t\bar{t}$". The total uncertainty on the background estimation is shown as a black hashed band. The expected contribution from a chiral fourth-generation T quark with mass $m_T = 600$ GeV is also shown (red histogram), stacked on top of the SM background. The lower panel shows the ratio of data to the SM prediction. The overflow has been added to the last bin.

absolute difference between the reconstructed heavy quark masses obtained by pairing the W_{lep} and W_{had} candidates with the two b-jet candidates as described below.

Table 2 presents a summary of the background estimates for the loose and tight selections, as well as a comparison of the total predicted and observed yields. The quoted uncertainties include both statistical and systematic contributions. The latter are discussed in Section 10. The predicted and observed yields are in agreement within these uncertainties.

The main discriminant variable used in this search is the reconstructed heavy-quark mass (m_{reco}), built from the W_{had} candidate and one of the two b-jet candidates. The reconstruction of the W_{lep} candidate usually yields two solutions, and there are two possible ways to pair the b-jet candidates with the W boson candidates to form the heavy quarks. Among all possible combinations, the one yielding the smallest absolute difference between the two reconstructed heavy quark masses, $|m^{\text{lep}}_{\text{reco}} - m^{\text{had}}_{\text{reco}}|$, is chosen. The resulting m_{reco} distributions for the loose and tight selections are shown in Fig. 6 for the sum of $W^{\text{type I}}_{\text{had}}$ and $W^{\text{type II}}_{\text{had}}$ events. The tight selection has the best expected sensitivity, and only this selection is chosen to derive the final result for the search. The loose selection, displaying a significant $t\bar{t}$ background at low m_{reco} which is in good agreement with the expectation, provides further confidence in the background modelling prior to the application of b-jet isolation requirements in the tight selection.

	Loose selection	Tight selection
$T\bar{T}(m_T = 600$ GeV)		
Chiral fourth-generation	115 ± 10	58.9 ± 5.9
Vector-like singlet	60.3 ± 5.1	24.5 ± 2.3
$t\bar{t}$	390 ± 110	10.7 ± 4.3
$t\bar{t}V$	6.5 ± 2.5	0.4 ± 0.2
W+jets	38 ± 19	11.4 ± 6.2
Z+jets	1.5 ± 1.2	0.4 ± 0.4
Single top	36 ± 17	2.2 ± 1.5
Diboson	5.6 ± 1.4	1.5 ± 0.6
Multijet	0.3 ± 1.6	0.8 ± 0.7
Total background	480 ± 120	27.5 ± 8.6
Data	478	34

Table 2: Number of observed events, integrated over the whole mass spectrum, compared to the SM expectation after the loose and tight selections in the $T\bar{T} \to Wb$+X search. The expected signal yields in two different scenarios, a chiral fourth-generation T quark and a vector-like singlet T quark, assuming $m_T = 600$ GeV, are also shown. The quoted uncertainties include both statistical and systematic contributions.

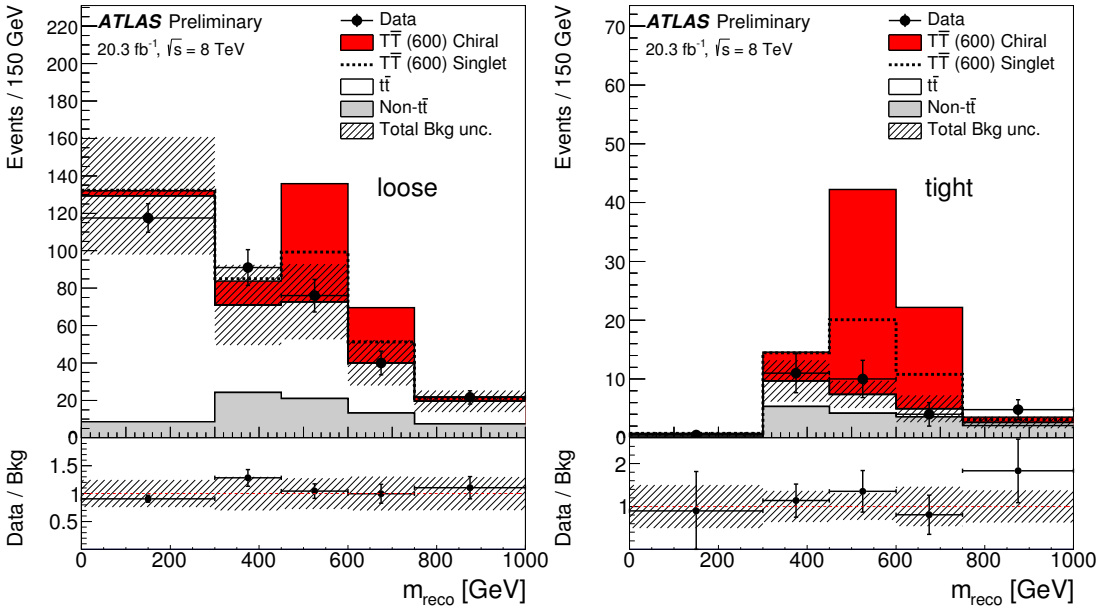

(a) (b)

Figure 6: Distribution of the reconstructed heavy-quark mass (m_{reco}) after (a) the loose selection and (b) the tight selection, for the sum of $W_{\text{had}}^{\text{type I}}$ and $W_{\text{had}}^{\text{type II}}$ events. The data (solid black points) are compared to the SM prediction (stacked histograms). The contributions from backgrounds other than $t\bar{t}$ are combined into a single background source referred to as "Non-$t\bar{t}$". The total uncertainty on the background estimation is shown as a black hashed band. The expected contributions from a chiral fourth-generation T quark (red histogram) and a singlet vector-like T quark (dashed black histogram), both with mass $m_T = 600$ GeV, are also shown stacked on top of the SM background. The lower panel shows the ratio of data to the SM prediction. The overflow has been added to the last bin.

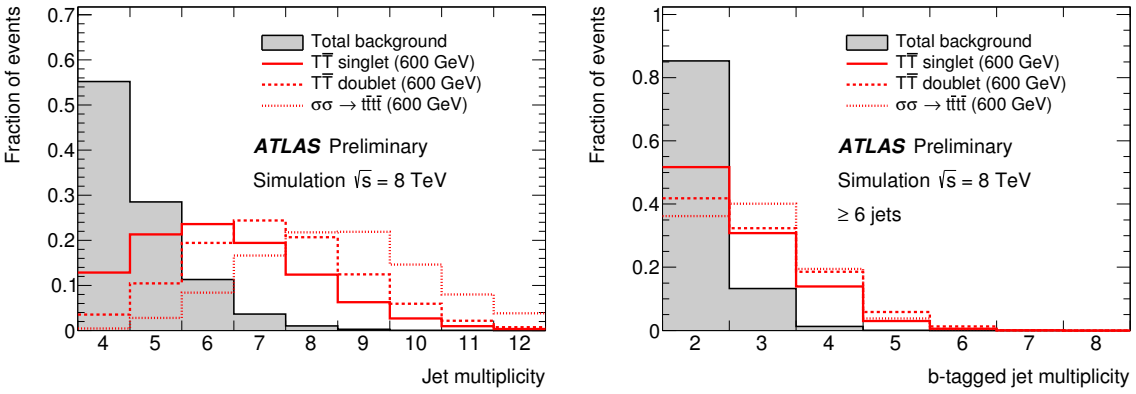

(a) (b)

Figure 7: $T\bar{T} \to Ht$+X search: comparison of (a) the jet multiplicity distribution after preselection, and (b) the b-tag multiplicity distribution after the requirement of ≥6 jets, between the total background (shaded histogram) and several signal scenarios considered in this search: $T\bar{T}$ production in the T quark singlet (red solid histogram) and doublet (red dashed histogram) cases, and sgluon pair production giving a a four-top-quark final state (red dotted histogram). A mass of 600 GeV is assumed for the T quark and the sgluon.

8. Search for $T\bar{T} \to Ht$+X and $t\bar{t}t\bar{t}$ production

This search is focused on $T\bar{T}$ production where at least one of the T quarks decays into a Higgs boson and a top quark resulting from the following processes: $T\bar{T} \to HtH\bar{t}$, $ZtHt$ and $WbHt$.[7] For the dominant $H \to b\bar{b}$ decay mode, the final state signature is characterised by high jet and b-tag multiplicities, which provide a powerful experimental handle to suppress the background. Similarly, this search is also sensitive to $T\bar{T} \to ZtZ\bar{t}$ and $WbZt$, with $Z \to b\bar{b}$. High jet and b-tag multiplicities are also characteristic of $t\bar{t}t\bar{t}$ events (both within the SM and in BSM extensions), which makes this search also sensitive to this process. Figure 7(a) compares the jet multiplicity distribution after preselection (described in Section 4) between the total background and several signal scenarios. Signal events have, on average, higher jet multiplicity than the background. The higher b-quark content of signal events results in a higher b-tag multiplicity than for the background, as illustrated in Fig. 7(b) for events with ≥6 jets. Therefore, after preselection, the final selection requirements are ≥5 jets of which ≥2 jets are b-tagged, leaving a sample completely dominated by $t\bar{t}$+jets background. In order to ensure a non-overlapping analysis sample and to facilitate the combination of results, events accepted by the Wb+X search are rejected. This veto only removes about 2% of the events with ≥6 jets and ≥4 b-tagged jets in data.

In order to optimise the sensitivity of the search, the selected events are categorised in different channels depending on the number of jets (5 and ≥6) and on the number of b-tagged jets (2, 3 and ≥4). The channel with ≥6 jet and ≥4 b-tagged jets has the largest signal-to-background ratio and therefore drives the sensitivity of the search. The channels with 2 and 3 b-tagged jets have significantly lower signal-to-background ratio. These are particularly useful to calibrate the $t\bar{t}$+jets background prediction and constrain the related systematic uncertainties. In the case of the channel with ≥6 jet and ≥4 b-tagged jets the background uncertainty is dominated by uncertainties on the b-tagging, jet energy calibration and

[7] In the following $ZtHt$ will be used to denote both $ZtH\bar{t}$ and its charge conjugate, $HtZ\bar{t}$. Similar notation will be used for other processes, as appropriate.

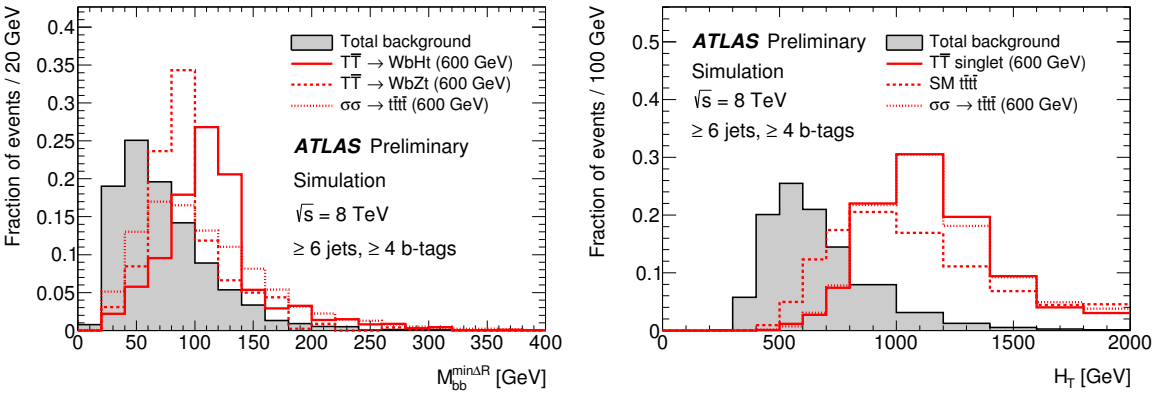

(a) (b)

Figure 8: $T\bar{T} \to Ht$+X search: comparison of the distributions of (a) the invariant mass of the two b-tagged jets with lowest ΔR separation ($M_{bb}^{\mathrm{min}\Delta R}$), and (b) the scalar sum of the transverse momenta of the lepton, the selected jets and the missing transverse momentum (H_{T}), between the total background (shaded histogram) and several signal scenarios considered in this search: $T\bar{T} \to WbHt$ (red solid histogram), $T\bar{T} \to WbZt$ or SM $t\bar{t}t\bar{t}$ production (red dashed histograms), and sgluon pair production giving a $t\bar{t}t\bar{t}$ final state (red dotted histogram). A mass of 600 GeV is assumed for the T quark and the sgluon. The selection used in both (a) and (b) corresponds to events satisfying the preselection requirements and with ≥6 jets and ≥4 b-tagged jets.

physics modelling, including the $t\bar{t}$+HF content. A detailed discussion of the systematic uncertainties considered is given in Section 10. In addition, events with ≥6 jets and 3 or ≥4 b-tagged jets are split into two channels each depending on the value of the invariant mass of the two b-tagged jets with lowest ΔR separation: $M_{bb}^{\mathrm{min}\Delta R} < 100$ GeV ("low $M_{bb}^{\mathrm{min}\Delta R}$") and $M_{bb}^{\mathrm{min}\Delta R} > 100$ GeV ("high $M_{bb}^{\mathrm{min}\Delta R}$"). For high values of m_T, the Higgs boson from the $T \to Ht$ decay has high p_{T}, and the $b\bar{b}$ pair from the Higgs boson decay has smaller angular separation than other pairs resulting from combinatorial background. As shown in Fig. 8(a), this simple variable provides a good approximation to the reconstructed $H \to b\bar{b}$ invariant mass and allows the separation of these channels into channels depleted or enriched in $T \to Ht$, $H \to b\bar{b}$ decays, the latter having a higher signal-to-background ratio. Therefore, the total number of analysis channels considered in this search is eight: (5 j, 2 b), (5 j, 3 b), (5 j, ≥4 b), (≥6 j, 2 b), (≥6 j, 3 b, low $M_{bb}^{\mathrm{min}\Delta R}$), (≥6 j, 3 b, high $M_{bb}^{\mathrm{min}\Delta R}$), (≥6 j, ≥4 b, low $M_{bb}^{\mathrm{min}\Delta R}$), and (≥6 j, ≥4 b, high $M_{bb}^{\mathrm{min}\Delta R}$), where ($n$ j, m j) indicates n selected jets and m b-tagged jets.

To further improve the separation between signal and background, the distinct kinematic features of the signal are exploited. In particular, the large T quark mass results in energetic leptons and jets in the final state, and H_{T} provides a suitable discriminating variable between signal and background. Figure 8(b) compares the H_{T} distribution between signal and background for events with ≥6 jets and ≥4 b-tagged jets. The H_{T} distribution is quite similar for different signal scenarios corresponding to pair production of exotic particles with the same mass (600 GeV in this case), and significantly different from that of the background. The discrimination between signal and background increases with mass.

Figures 9 and 10 show the comparison of data and prediction for the H_{T} distributions in each of the analysis channels considered. The corresponding predicted and observed yields per channel can be found in Table 3. No significant signal-like excess above the SM prediction is observed. Following the statistical procedure outlined in Section 11, a fit to the observed H_{T} distributions in data in the eight analysis channels is performed. This provides an improved background prediction with smaller uncertainties, and

hence improved sensitivity to a signal. The results are presented in Section 12.

9. Search for $B\bar{B} \to Hb$+X production

This search is focused on $B\bar{B}$ production where at least one of the B quarks decays into a Higgs boson and a b quark. The $B \to Hb$ decay channel is of interest because it has been mostly omitted from previous searches for $B\bar{B}$ production [25–27]. In particular, the $BB \to HbHb$ final state is the least covered one because the most-common Higgs boson decay mode, $H \to b\bar{b}$, leads to a challenging final state with six b-jets and no leptons. In contrast, cleaner experimental signatures involving leptons tend to be suppressed by the small decay branching ratios. However, a sizeable signal rate results from the mixed decay mode where one of the Higgs bosons decays into W^+W^-, while the other Higgs boson decays into $b\bar{b}$: $B\bar{B} \to HbH\bar{b} \to (W^+W^-)b(b\bar{b})\bar{b}$. When one of the W bosons decays leptonically, this leads to the final state signature considered by this search, involving one lepton and high jet and b-tag multiplicities, analogous to the signature exploited by the $T\bar{T} \to Ht$+X search.

Consequently, this search considers the same discriminating variable, H_{T}, and the same eight analysis channels as the $T\bar{T} \to Ht$+X search. Figure 11(a) illustrates the good separation between signal and background in the H_{T} distribution for events passing the preselection requirements and with ≥ 6 jets and ≥ 4 b-tagged jets. A peculiarity of the $B \to Hb$ decay mode is that the b-jet originating (directly) from the B-quark decay can have very high transverse momentum in the case of a heavy B quark. To exploit this feature, the event selection is tightened relative to that used in the $T\bar{T} \to Ht$+X search by raising the minimum p_{T} requirement on the two highest-p_{T} (leading) b-tagged jets to $p_{\mathrm{T}} > 150$ GeV. Figure 11(b) shows the distribution of the subleading b-jet p_{T} for events passing the preselection requirements and with ≥ 6 jets and ≥ 4 b-tagged jets. The tighter requirement on the subleading b-jet p_{T} rejects about 90% of the $t\bar{t}$ background while retaining a large acceptance for the $B\bar{B} \to Hb$+X signal. This search is also sensitive to other $B\bar{B}$ final states, such as $B\bar{B} \to HbWt$, that typically do not involve multilepton final states in the topologies usually searched for (opposite-sign dileptons with a $Z \to \ell^+\ell^-$ candidate, same-sign dileptons, and trileptons), thus becoming complementary to previous searches [25–27].

Figures 12 and 13 show the comparison of data and prediction for the H_{T} distributions in each of the analysis channels considered. The corresponding predicted and observed yields per channel can be found in Table 4. No significant signal-like excess above the SM prediction is observed. The results of the fit to the data to improve the background prediction, as in the $T\bar{T} \to Ht$+X search, are presented in Section 12.

10. Systematic uncertainties

Several sources of systematic uncertainties are considered that can affect the normalisation of signal and background and/or the shape of their corresponding final discriminant distributions. Individual sources of systematic uncertainty are considered uncorrelated. Correlations of a given systematic uncertainty are maintained across processes and channels. Table 5 presents a list of all systematic uncertainties considered in the analyses indicating whether they are taken to be normalisation-only, or to affect both shape and normalisation. The following sections describe each of the systematic uncertainties considered in the analysis. Tables summarising the impact from these systematic uncertainties on the normalisation of signal and background for all three searches can be found in Appendix A.

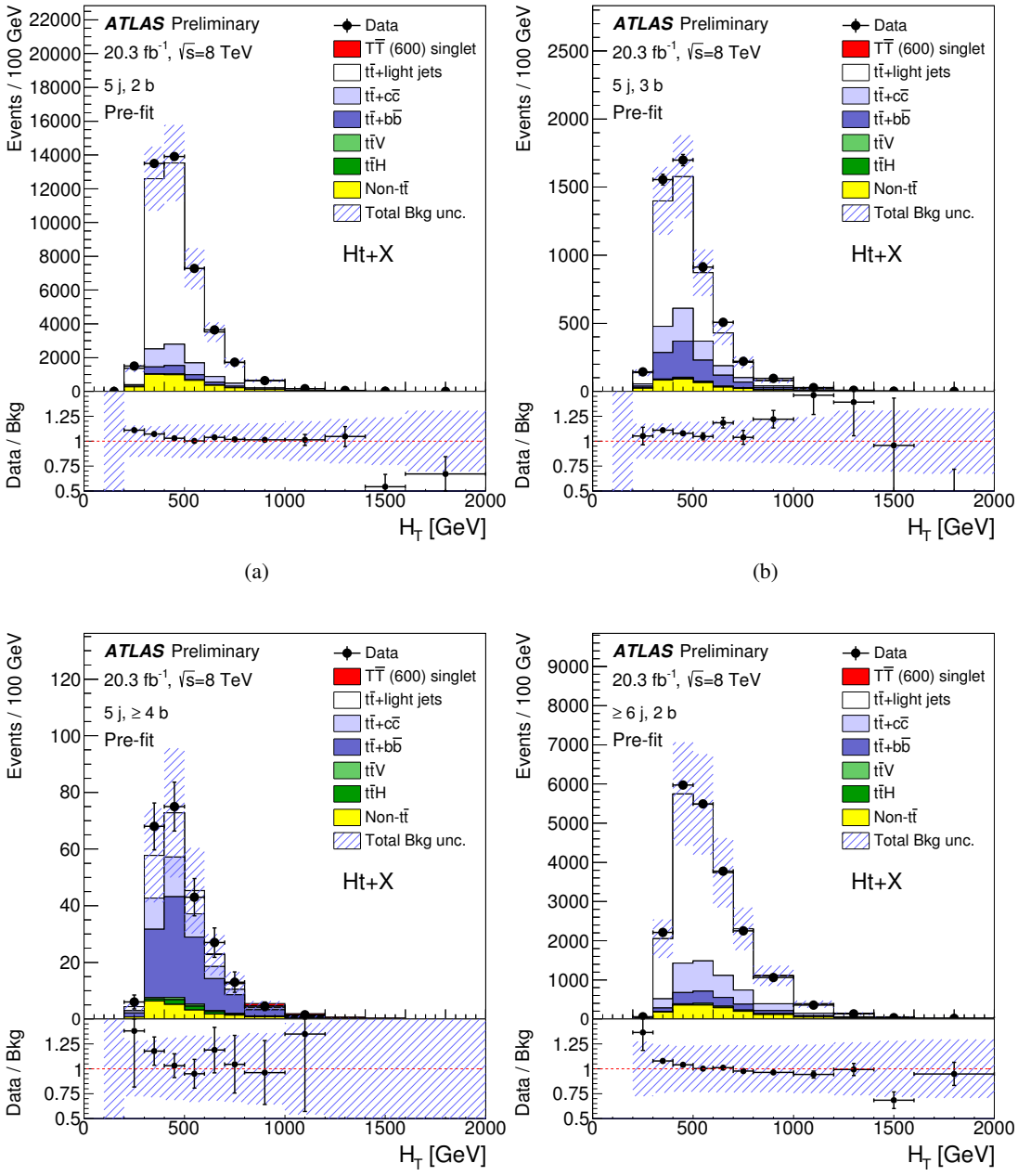

Figure 9: $T\bar{T} \rightarrow Ht$+X search: comparison between data and prediction for the distribution of the scalar sum of the transverse momenta of the lepton, the selected jets and the missing transverse momentum (H_{T}) in each of the analysed channels: (a) (5 j, 2 b), (b) (5 j, 3 b), (c) (5 j, ≥4 b), and (d) (≥6 j, 2 b). The background prediction is shown before the fit to data. The contributions from W/Z+jets, single top, diboson and multijet backgrounds are combined into a single background source referred to as "Non-$t\bar{t}$". Also shown is the expected signal contribution from a singlet vector-like T quark with mass $m_T = 600$ GeV. The last bin in all figures contains the overflow. The bottom panel displays the ratio between data and total background prediction. The hashed area represents the total uncertainty on the background.

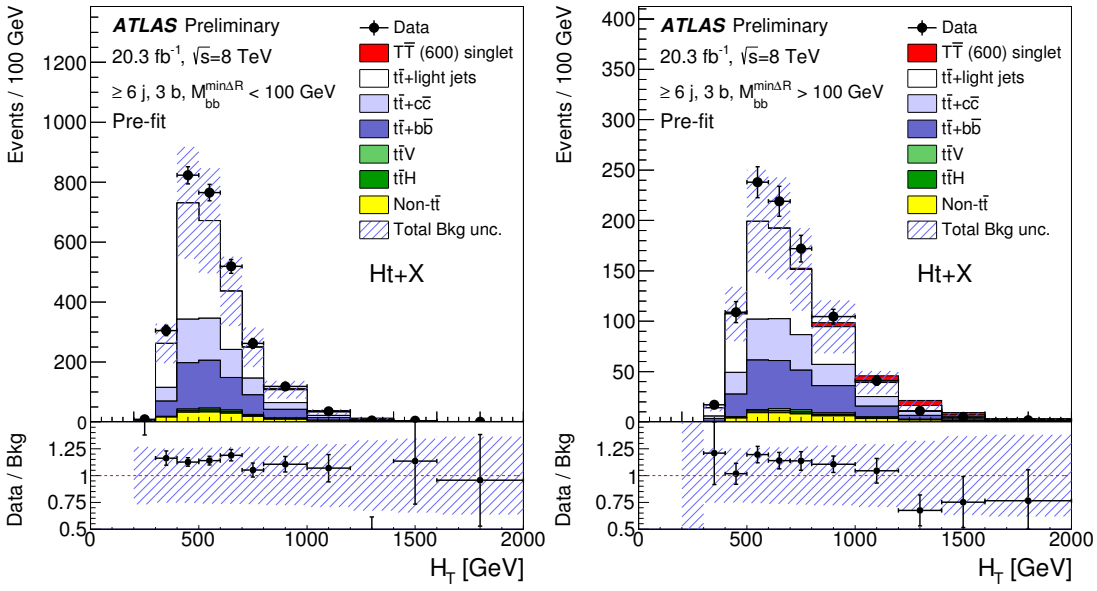

(a)

(b)

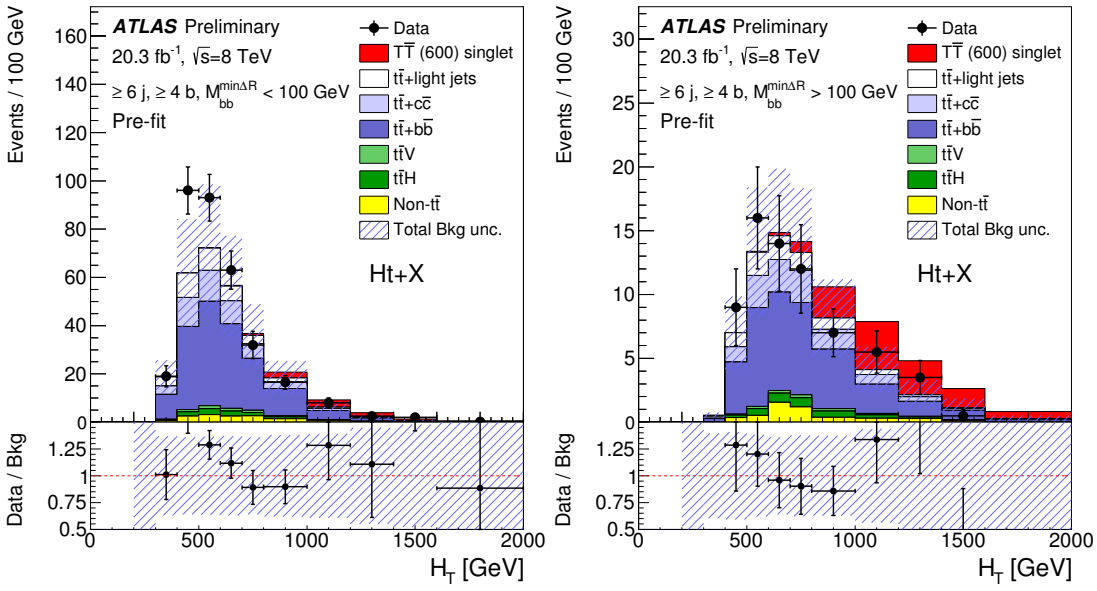

(c)

(d)

Figure 10: $T\bar{T} \rightarrow Ht$+X search: comparison between data and prediction for the distribution of the scalar sum of the transverse momenta of the lepton, the selected jets and the missing transverse momentum (H_{T}) in each of the analysed channels: (a) (≥6 j, 3 b, low $M_{bb}^{\mathrm{min}\Delta R}$), (b) (≥6 j, 3 b, high $M_{bb}^{\mathrm{min}\Delta R}$), (c) (≥6 j, ≥4 b, low $M_{bb}^{\mathrm{min}\Delta R}$), and (d) (≥6 j, ≥4 b, high $M_{bb}^{\mathrm{min}\Delta R}$). The background prediction is shown before the fit to data. The contributions from W/Z+jets, single top, diboson and multijet backgrounds are combined into a single background source referred to as "Non-$t\bar{t}$". Also shown is the expected signal contribution from a singlet vector-like T quark with mass m_T = 600 GeV. The last bin in all figures contains the overflow. The bottom panel displays the ratio between data and total background prediction. The hashed area represents the total uncertainty on the background.

	5 j, 2 b	5 j, 3 b	5 j, ≥4 b	≥6 j, 2 b
$T\bar{T}$ (m_T = 600 GeV)				
Singlet	52.5 ± 4.2	19.0 ± 2.3	5.8 ± 1.2	123.3 ± 6.2
Doublet	25.8 ± 2.0	14.0 ± 1.4	5.0 ± 1.0	154.1 ± 6.4
$\sigma\sigma \to t\bar{t}t\bar{t}$ (m_σ = 800 GeV)	2.0 ± 0.3	1.4 ± 0.3	0.3 ± 0.1	64.8 ± 4.6
$t\bar{t}t\bar{t}$+X (Tier (1,1), m_{KK} = 800 GeV)	1.0 ± 0.4	0.6 ± 0.3	0.06 ± 0.05	180 ± 29
$t\bar{t}$+light jets	32400 ± 5300	2930 ± 520	48 ± 12	16200 ± 4000
$t\bar{t}$ + $c\bar{c}$	3800 ± 2100	730 ± 410	42 ± 24	3300 ± 1800
$t\bar{t}$ + $b\bar{b}$	1530 ± 800	800 ± 420	108 ± 58	1300 ± 700
$t\bar{t}V$	140 ± 46	24.9 ± 8.1	2.9 ± 1.0	172 ± 56
$t\bar{t}H$	39.2 ± 1.7	20.8 ± 1.6	5.6 ± 0.7	60.2 ± 4.5
W+jets	1600 ± 1000	111 ± 71	5.0 ± 3.4	770 ± 530
Z+jets	360 ± 120	24.8 ± 8.4	1.2 ± 0.5	185 ± 67
Single top	1630 ± 320	169 ± 36	7.0 ± 1.0	730 ± 200
Diboson	85 ± 27	7.3 ± 2.5	0.4 ± 0.2	45 ± 15
Multijet	133 ± 48	33 ± 12	6.9 ± 2.6	56 ± 20
Total background	41700 ± 6400	4840 ± 900	228 ± 69	22800 ± 5200
Data	43319	5309	244	23001

	≥6 j, 3 b low $M_{bb}^{\min\Delta R}$	≥6 j, 3 b high $M_{bb}^{\min\Delta R}$	≥6 j, ≥4 b low $M_{bb}^{\min\Delta R}$	≥6 j, ≥4 b high $M_{bb}^{\min\Delta R}$
$T\bar{T}$ (m_T = 600 GeV)				
Singlet	29.5 ± 2.0	44.0 ± 3.6	17.7 ± 1.9	24.1 ± 3.7
Doublet	50.2 ± 2.5	68.9 ± 4.1	41.0 ± 3.9	53.8 ± 7.3
$\sigma\sigma \to t\bar{t}t\bar{t}$ (m_σ = 800 GeV)	22.5 ± 1.6	50.7 ± 3.5	9.3 ± 1.0	16.2 ± 2.6
$t\bar{t}t\bar{t}$+X (Tier (1,1), m_{KK} = 800 GeV)	33.6 ± 2.8	132.5 ± 5.9	27.7 ± 2.3	75 ± 13
$t\bar{t}$+light jets	1280 ± 350	440 ± 110	38 ± 14	9.3 ± 3.9
$t\bar{t}$ + $c\bar{c}$	550 ± 320	220 ± 120	53 ± 31	14.7 ± 9.0
$t\bar{t}$ + $b\bar{b}$	620 ± 330	250 ± 140	178 ± 95	46 ± 25
$t\bar{t}V$	28.7 ± 9.2	12.5 ± 4.2	6.2 ± 2.0	1.5 ± 0.5
$t\bar{t}H$	24.9 ± 1.9	11.6 ± 1.3	10.6 ± 1.2	4.1 ± 0.6
W+jets	68 ± 46	16 ± 10	6.6 ± 4.8	0.6 ± 0.4
Z+jets	15.7 ± 6.3	3.3 ± 1.3	1.6 ± 0.6	0.3 ± 0.1
Single top	74 ± 22	32 ± 12	7.8 ± 2.2	2.1 ± 1.3
Diboson	4.2 ± 1.6	1.2 ± 0.5	0.4 ± 0.1	0.2 ± 0.1
Multijet	1.9 ± 0.8	4.8 ± 2.1	< 0.01	2.8 ± 1.0
Total background	2670 ± 680	990 ± 260	300 ± 110	81 ± 30
Data	3015	1085	362	84

Table 3: Predicted and observed yields in each of the analysis channels considered by the $T\bar{T} \to Ht$+X search. The background prediction is shown before the combined fit to data. Also shown are the signal predictions for different benchmark scenarios considered. The quoted uncertainties are the sum in quadrature of statistical and systematic uncertainties on the yields.

	5 j, 2 b	5 j, 3 b	5 j, ≥4 b	≥6 j, 2 b
$B\bar{B}$ (m_B = 600 GeV)				
$BR(B \to Hb) = 1$	8.6 ± 1.1	9.3 ± 2.2	5.0 ± 1.4	11.9 ± 3.0
Singlet	12.2 ± 1.9	8.8 ± 1.7	3.4 ± 0.8	27.4 ± 4.3
(B,Y) Doublet	8.5 ± 1.1	5.8 ± 1.4	2.8 ± 0.8	10.9 ± 2.1
$t\bar{t}$+light jets	389 ± 93	72 ± 18	2.1 ± 0.7	234 ± 74
$t\bar{t} + c\bar{c}$	56 ± 42	23 ± 15	2.2 ± 1.5	55 ± 40
$t\bar{t} + b\bar{b}$	19 ± 14	25 ± 14	5.5 ± 3.2	22 ± 15
$t\bar{t}V$	4.2 ± 1.4	1.6 ± 0.5	0.3 ± 0.1	5.1 ± 1.7
$t\bar{t}H$	1.0 ± 0.1	1.1 ± 0.2	0.5 ± 0.1	1.5 ± 0.2
W+jets	21 ± 12	3.5 ± 2.1	0.6 ± 0.5	12.5 ± 7.9
Z+jets	8.2 ± 3.3	2.8 ± 2.8	0.5 ± 0.5	4.3 ± 4.1
Single top	41.3 ± 7.2	8.8 ± 1.9	0.6 ± 0.1	28.0 ± 6.8
Diboson	1.9 ± 0.9	0.5 ± 0.3	0.07 ± 0.07	1.2 ± 0.7
Multijet	< 0.01	< 0.01	0.4 ± 0.2	0.2 ± 0.1
Total background	540 ± 120	139 ± 35	12.8 ± 4.9	360 ± 100
Data	576	165	10	375

	≥6 j, 3 b low $M_{bb}^{\min\Delta R}$	≥6 j, 3 b high $M_{bb}^{\min\Delta R}$	≥6 j, ≥4 b low $M_{bb}^{\min\Delta R}$	≥6 j, ≥4 b high $M_{bb}^{\min\Delta R}$
$B\bar{B}$ (m_B = 600 GeV)				
$BR(B \to Hb) = 1$	3.8 ± 0.6	13.1 ± 1.8	3.2 ± 0.7	9.6 ± 2.0
Singlet	7.1 ± 0.9	15.8 ± 2.5	4.6 ± 0.9	7.5 ± 1.5
(B,Y) Doublet	2.7 ± 0.3	7.0 ± 1.3	2.3 ± 0.6	3.9 ± 0.9
$t\bar{t}$+light jets	21.3 ± 9.0	32.8 ± 9.5	1.4 ± 0.5	1.5 ± 0.6
$t\bar{t} + c\bar{c}$	10.8 ± 7.5	20 ± 15	2.2 ± 1.6	2.9 ± 2.2
$t\bar{t} + b\bar{b}$	13.1 ± 8.5	24 ± 16	7.8 ± 4.8	8.1 ± 5.3
$t\bar{t}V$	1.1 ± 0.4	1.6 ± 0.6	0.6 ± 0.2	0.4 ± 0.2
$t\bar{t}H$	0.7 ± 0.1	1.4 ± 0.2	0.5 ± 0.1	0.9 ± 0.2
W+jets	2.0 ± 1.3	1.1 ± 0.8	0.3 ± 0.3	0.05 ± 0.05
Z+jets	0.11 ± 0.07	0.2 ± 0.1	< 0.01	< 0.01
Single top	3.2 ± 0.6	5.1 ± 2.2	0.8 ± 0.2	0.3 ± 0.2
Diboson	0.2 ± 0.1	0.09 ± 0.03	0.02 ± 0.01	< 0.01
Multijet	< 0.01	0.6 ± 0.2	< 0.01	0.4 ± 0.1
Total background	53 ± 18	87 ± 30	13.7 ± 5.9	14.5 ± 7.3
Data	62	103	23	20

Table 4: Predicted and observed yields in each of the analysis channels considered by the $B\bar{B} \to Hb$+X search. The background prediction is shown before the combined fit to data. Also shown are the signal predictions for different benchmark scenarios considered. The quoted uncertainties are the sum in quadrature of statistical and systematic uncertainties on the yields.

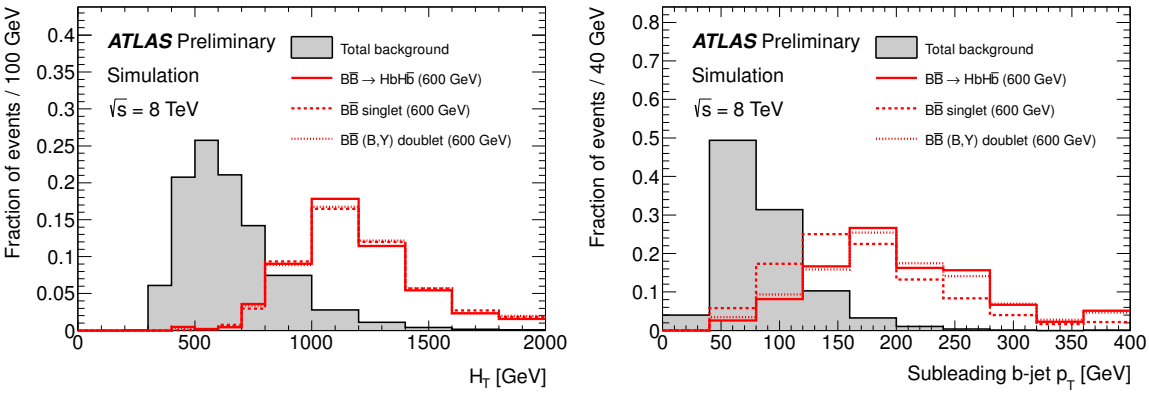

(a) (b)

Figure 11: $B\bar{B} \to Hb$+X search: comparison of the distributions of (a) the scalar sum of the transverse momenta of the lepton, the selected jets and the missing transverse momentum (H_{T}), and (b) the transverse momentum of the next-to-highest-transverse-momentum b-jet, between the total background (shaded histogram) and several $B\bar{B}$ signal scenarios considered in this search: $BR(B \to Hb) = 1$ (red solid histogram), B quark singlet (red dashed histogram), and B quark from a (B,Y) doublet (red dotted histogram). In all cases a mass of 600 GeV is assumed for the B quark. The selection used in both (a) and (b) corresponds to events satisfying the preselection requirements and with ≥6 jets and ≥4 b-tagged jets.

In the case of the $T\bar{T} \to Wb$+X search, the total systematic uncertainty in the background normalisation is approximately 29%, with the dominant contributions originating from the normalisation of the W+jets background (20%), jet energy scale (+17%/−12%) and the $t\bar{t}$+HF normalisation (11%). The total systematic uncertainty in the signal normalisation is +8%/−10%, with comparable contributions from jet energy scale and b-tagging uncertainties.

The leading sources of systematic uncertainty in the $T\bar{T} \to Ht$+X and $B\bar{B} \to Hb$+X searches vary depending on the analysis channel considered, but they typically originate from $t\bar{t}$+jets modelling (including $t\bar{t}$+HF), jet energy scale and b-tagging. For example, the total systematic uncertainty in the background normalisation in the highest-sensitivity channel (≥6 j, ≥4 b, high $M_{bb}^{\mathrm{min}\Delta R}$) of the $T\bar{T} \to Ht$+X search is approximately 37%, with the largest contributions originating from $t\bar{t}$+HF normalisation (23%), jet energy scale (10%) and b-tagging (9%). However, as discussed previously, the fit to data in the eight analysis channels in these searches allows the overall background uncertainty to be reduced significantly, down to approximately 5% in the case of the $T\bar{T} \to Ht$+X search. More details on the fit to data can be found in Section 12.1. The total systematic uncertainty on the signal normalisation is approximately 15%, completely dominated by b-tagging uncertainties.

10.1. Luminosity

The uncertainty on the integrated luminosity is 2.8%, affecting the overall normalisation of all processes estimated from the simulation. It is derived following the same methodology as that detailed in Ref. [44].

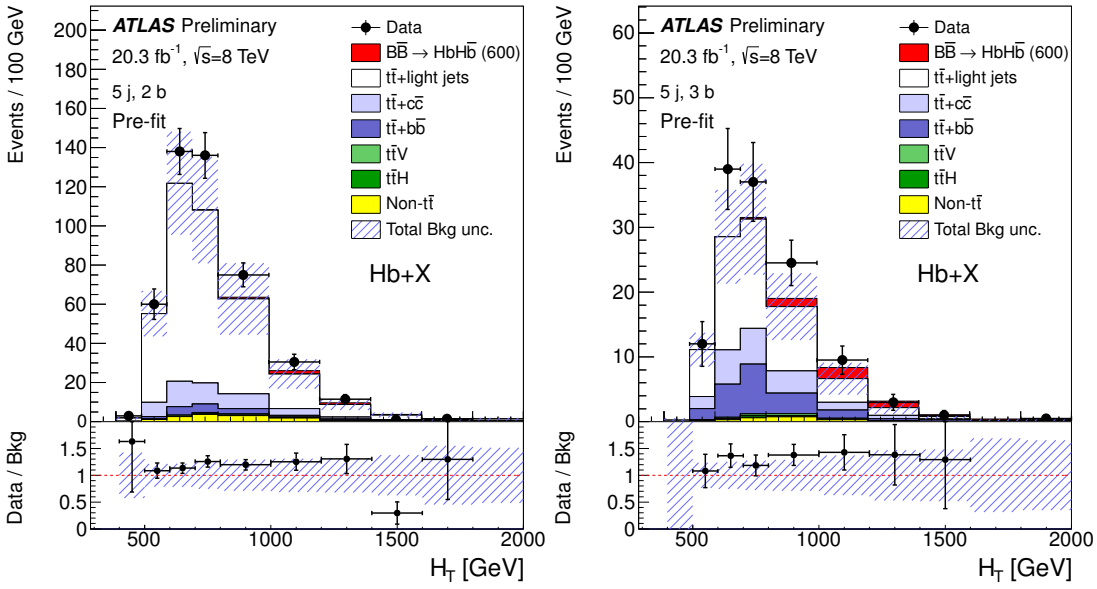

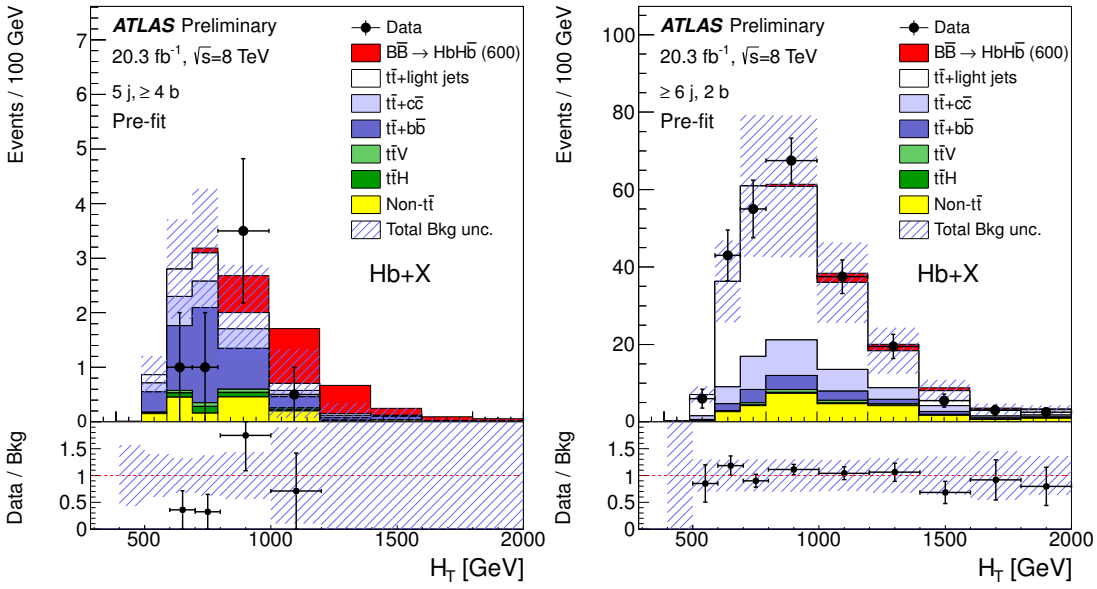

Figure 12: $B\bar{B} \to Hb$+X search: comparison between data and prediction for the distribution of the scalar sum of the transverse momenta of the lepton, the selected jets and the missing transverse momentum (H_{T}) in each of the analysed channels: a) (5 j, 2 b), (b) (5 j, 3 b), (c) (5 j, ≥4 b), and (d) (≥6 j, 2 b). The background prediction is shown before the fit to data. The contributions from W/Z+jets, single top, diboson and multijet backgrounds are combined into a single background source referred to as "Non-$t\bar{t}$". Also shown is the expected signal contribution from a vector-like B quark with mass m_T = 600 GeV under the assumption $BR(B \to Hb) = 1$. The last bin in all figures contains the overflow. The bottom panel displays the ratio between data and total background prediction. The hashed area represents the total uncertainty on the background.

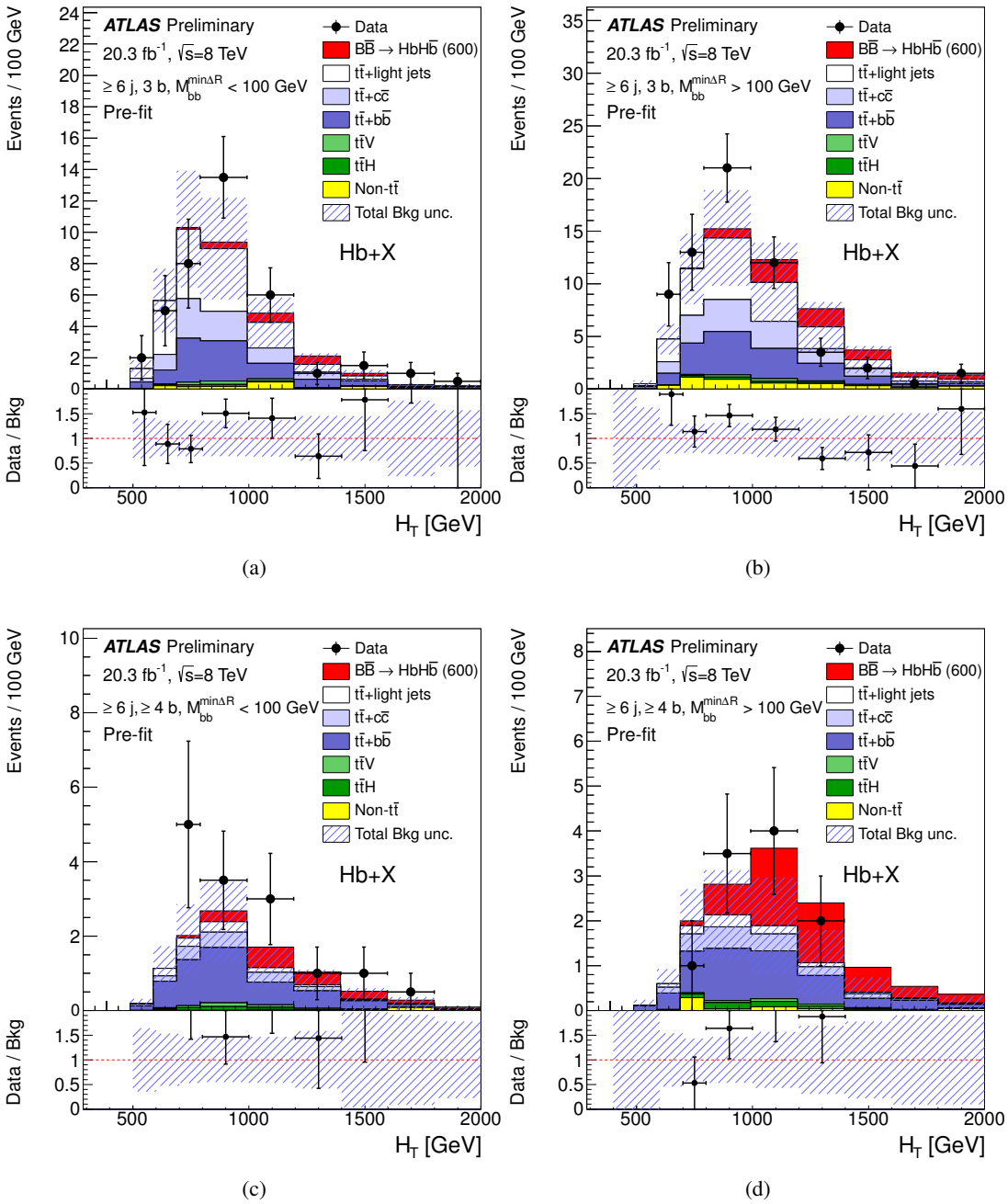

Figure 13: $B\bar{B} \to Hb$+X search: comparison between data and prediction for the distribution of the scalar sum of the transverse momenta of the lepton, the selected jets and the missing transverse momentum (H_{T}) in each of the analysed channels: (a) (≥6 j, 3 b, low $M_{bb}^{\mathrm{min}\Delta R}$), (b) (≥6 j, 3 b, high $M_{bb}^{\mathrm{min}\Delta R}$), (c) (≥6 j, ≥4 b, low $M_{bb}^{\mathrm{min}\Delta R}$), and (d) (≥6 j, ≥4 b, high $M_{bb}^{\mathrm{min}\Delta R}$). The background prediction is shown before the fit to data. The contributions from W/Z+jets, single top, diboson and multijet backgrounds are combined into a single background source referred to as "Non-$t\bar{t}$". Also shown is the expected signal contribution from a vector-like B quark with mass $m_T = 600$ GeV under the assumption $BR(B \to Hb) = 1$. The last bin in all figures contains the overflow. The bottom panel displays the ratio between data and total background prediction. The hashed area represents the total uncertainty on the background.

Systematic uncertainty	Type	Components
Luminosity	N	1
Reconstructed Objects		
Electron	SN	5
Muon	SN	6
Jet reconstruction	SN	1
Jet vertex fraction	SN	1
Jet energy scale	SN	22
Jet energy resolution	SN	1
Missing transverse momentum	SN	2
b-tagging efficiency	SN	6
c-tagging efficiency	SN	4
Light jet-tagging efficiency	SN	12
High-p_{T} tagging	SN	1
Background Model		
$t\bar{t}$ cross section	N	1
$t\bar{t}$ modelling: p_T reweighting	SN	9
$t\bar{t}$ modelling: parton shower	SN	3
$t\bar{t}$+HF: normalisation	N	2
$t\bar{t}$+$c\bar{c}$: HF reweighting	SN	2
$t\bar{t}$+$c\bar{c}$: generator	SN	4
$t\bar{t}$+$b\bar{b}$: NLO Shape	SN	8
W+jets normalisation	N	3
Z+jets normalisation	N	3
Single top cross section	N	1
Single top model	SN	1
Diboson normalisation	N	1
$t\bar{t}V$ cross section	N	1
$t\bar{t}V$ model	SN	1
$t\bar{t}H$ cross section	N	1
$t\bar{t}H$ model	SN	2
Multijet normalisation	N	2

Table 5: List of systematic uncertainties considered. An “N" means that the uncertainty is taken as normalisation-only for all processes and channels affected, whereas “SN" means that the uncertainty is taken on both shape and normalisation. Some of the systematic uncertainties are split into several components for a more accurate treatment.

10.2. Reconstructed objects

10.2.1. Leptons

Uncertainties associated with leptons arise from the reconstruction, identification and trigger, as well as the lepton momentum scale and resolution. The reconstruction and identification efficiency of electrons

and muons, as well as the efficiency of the trigger used to record the events, differ between data and simulation. Scale factors are derived using tag-and-probe techniques on $Z \to \ell^+\ell^-$ ($\ell = e, \mu$) data and simulated samples, and are applied to the simulation to correct for discrepancies. Additional sources of uncertainty originate from the corrections applied to adjust the lepton momentum scale and resolution in the simulation to match those in data, measured using reconstructed distributions of the $Z \to \ell^+\ell^-$ and $J/\psi \to \ell^+\ell^-$ masses, as well as the measured E/p in $W \to e\nu$ events, where E and p are the electron energy and momentum, as measured by the calorimeter and the tracker respectively. The combined effect of all these uncertainties results in an overall normalisation uncertainty on the signal and background of approximately 1.5%.

10.2.2. Jets and missing transverse momentum

Uncertainties associated with jets arise from the efficiency of jet reconstruction and identification based on the JVF variable, as well as the jet energy scale and resolution. The uncertainty associated with the jet reconstruction efficiency is assessed by randomly removing 0.2% of the jets with p_{T} below 30 GeV, which is the level of disagreement between data and the simulation, and has a negligible impact in the analysis. The per-jet efficiency to satisfy the JVF requirement is measured in $Z(\to \ell^+\ell^-)$+1-jet events in data and simulation, selecting separately events enriched in hard-scatter jets and events enriched in jets from pileup, finding good agreement. The associated uncertainty is estimated by changing the nominal JVF cut value by 0.1 up and down and repeating the analysis using the modified cut value, resulting in normalisation uncertainties in the range of 1–5%, depending on the jet multiplicity under consideration and the p_{T} spectra of the jets. The jet energy scale (JES) and its uncertainty have been derived combining information from test-beam data, LHC collision data and simulation [40]. The jet energy scale uncertainty is split into 22 uncorrelated sources with their respective jet p_{T} and η dependences and are treated independently in this analysis. It represents one of the leading sources of uncertainty associated with reconstructed objects, affecting the normalisations of signal and backgrounds by approximately 5% and 15% respectively, in the most signal-rich channels considered. The jet energy resolution has been measured for data and the simulation as a function of jet p_{T} and rapidity using dijet events. They are found to agree within 10%, and the corresponding uncertainty is assessed by smearing the jet p_{T} in the simulation.

The $E_{\mathrm{T}}^{\mathrm{miss}}$ reconstruction is affected by uncertainties associated with leptons and jet energy scales and resolutions, which are propagated to $E_{\mathrm{T}}^{\mathrm{miss}}$. Additional small uncertainties associated with the modelling of the underlying event, in particular its impact on the p_{T} scale and resolution of unclustered energy, are also taken into account.

10.2.3. Heavy- and light-flavour tagging

Efficiencies to tag jets from b- and c-quarks in the simulation have to be corrected by p_{T}-dependent factors, that range approximately from 0.9–1.0 and from 0.9–1.1 respectively, whereas the light jet efficiency has to be scaled by p_{T}- and η-dependent scale factors in the range 1.2–1.5 [41, 42]. Uncertainties on these scale factors include a total of six independent sources affecting b-jets and four independent sources affecting c-jets. Each of these uncertainties has different jet p_{T} dependence. Twelve uncertainties are considered for the light jets tagging which depend on the jet p_{T} and η regions. These systematic uncertainties are taken as uncorrelated between b-jets, c-jets, and light jets. An additional uncertainty is included due to the extrapolation of the b-, c-, and light-tagging scale factors for jets with p_{T} beyond the

kinematic reach of the data calibration samples used: $p_{\mathrm{T}} > 300$ GeV for b- and c-jets, and $p_{\mathrm{T}} > 750$ GeV for light jets. This uncertainty is evaluated in the simulation comparing the tagging efficiencies by varying e.g. the fraction of tracks with shared hits in the silicon detectors or the fraction of fake tracks resulting from random combinations of hits, both of which typically increase at high p_{T} due to growing track multiplicity and density of hits within the jet. These uncertainties are taken to be correlated among the three jet flavours. As an example, the uncertainties on the tagging efficiencies for b-jets and c-jets with 300 GeV $\leq p_{\mathrm{T}} <$ 500 GeV are 14% and 23% respectively.

10.3. Background modelling

10.3.1. $t\bar{t}$ +jets

A number of systematic uncertainties affecting the modelling of $t\bar{t}$+jets are considered. These include the uncertainty on the inclusive theoretical cross section, uncertainties associated with the reweighting procedure applied to $t\bar{t}$+light jets and $t\bar{t} + c\bar{c}$ processes, uncertainties affecting the modelling of $t\bar{t}$+HF jets production, and uncertainties associated with the choice of parton shower and hadronisation model. A summary of these uncertainties can be found below. Additional details can be found in Ref. [97].

An uncertainty of +5%/−6% is assumed for the inclusive $t\bar{t}$ production cross section [45], including contributions from factorisation and renormalisation scale variations and uncertainties arising from the PDFs, α_S and the top-quark mass. The PDF and α_S uncertainties were calculated using the PDF4LHC prescription.

Uncertainties associated with the reweighting procedure applied to $t\bar{t}$+light jets and $t\bar{t} + c\bar{c}$ processes include the nine leading sources of uncertainty in the differential cross section measurement at $\sqrt{s} =$ 7 TeV [93], dominated by the modelling of initial- and final-state radiation and the choice of event generator for $t\bar{t}$ production.

Uncertainties affecting the modelling of $t\bar{t} + b\bar{b}$ production include those associated with the NLO prediction from Sherpa+OpenLoops that the default Powheg $t\bar{t} + b\bar{b}$ is reweighted to. Those include three different scale variations, shower recoil model scheme and two alternative PDFs (MSTW and NNPDF). A fraction of the $t\bar{t} + b\bar{b}$ background originates from multiple parton interactions (MPI) or final-state radiation (FSR) from top decay products. Such background cannot be calibrated to the NLO prediction, and these two categories are kept separate and subject to additional normalisation uncertainties. The NLO corrections and associated systematic uncertainties are adjusted so that the overall normalisation of the $t\bar{t} + b\bar{b}$ background at the particle level is fixed, i.e. effectively only migrations across categories and distortions to the shape of the kinematic distributions are considered. Detailed comparisons of $t\bar{t} + b\bar{b}$ between Powheg+Pythia and Sherpa+OpenLoops show that the cross sections agree to better than 50%, which is taken as normalisation uncertainty for $t\bar{t} + b\bar{b}$.

Beyond the uncertainties associated with the reweighting procedure, additional uncertainties are assigned to the modelling of the $t\bar{t}+c\bar{c}$ component of the background, which cannot be calibrated to NLO prediction as in the case of $t\bar{t}+b\bar{b}$. Those include two uncertainties taken as the full difference between applying and not applying the reweightings of the top-quark and $t\bar{t}$ p_{T} spectra and three uncertainties associated with the choice of LO generator from the comparison of Powheg+Pythia and Madgraph5+Pythia simulations (factorisation and renormalisation scale variations, matching threshold and c-quark mass). Analogously to the procedure used in the $t\bar{t}+b\bar{b}$ background, these uncertainties are adjusted so that the overall normalisation of the $t\bar{t}+c\bar{c}$ background at the particle level is fixed. Finally, an overall normalisation uncertainty

of 50% is also assigned to the $t\bar{t}$ + $c\bar{c}$ component, taken as uncorrelated with the same normalisation uncertainty applied to $t\bar{t}$ + $b\bar{b}$, since only the $t\bar{t}$ + $b\bar{b}$ process is normalised to a NLO prediction.

An uncertainty due to the choice of the parton shower and hadronisation model is derived by comparing events produced by Powheg interfaced to Pythia or Herwig. In the case of $t\bar{t}$+light jets and $t\bar{t}$ + $c\bar{c}$, a reweighting of top p_{T} and $t\bar{t}$ p_{T} is also performed to the Powheg+Herwig samples to ensure reasonable modelling of the top quark kinematics. The corresponding correction factors have been re-derived for Powheg+Herwig in order to match the differential cross section measurements at $\sqrt{s}$ = 7 TeV. In the case of $t\bar{t}$ + $b\bar{b}$, the various HF categories and the corresponding partonic kinematics in Powheg+Herwig are reweighted to match the NLO prediction of Sherpa+OpenLoops, so that only the effect of change in the hadronisation model is propagated. Given the different meaning of this uncertainty for $t\bar{t}$+light jets, $t\bar{t}+c\bar{c}$ and $t\bar{t}+b\bar{b}$, it is treated as uncorrelated between the three processes. This treatment avoids reducing the impact of this systematic uncertainty on $t\bar{t}$ + $c\bar{c}$ and $t\bar{t}$ + $b\bar{b}$ by constraining it for $t\bar{t}$+light jets via the fit to data in the high-statistics channels with 2 b-tagged jets.

10.3.2. W/Z+jets

Uncertainties affecting the modelling of the W/Z+jets background include 5% from their respective normalisations to the theoretical NNLO cross sections [100], as well as an additional 24% normalisation uncertainty added in quadrature for each additional inclusive parton multiplicity bin, based on a comparison among different algorithms for merging LO matrix-elements and parton showers [119]. The above uncertainties are taken as uncorrelated between W+jets and Z+jets.

10.3.3. Other simulated background

Uncertainties affecting the modelling of the single top quark background include a +5%/−4% uncertainty on the total cross section estimated as a weighted average of the theoretical uncertainties on t-, Wt- and s-channel production [102–104], as well as a systematic uncertainty on Wt-channel production concerning the separation between $t\bar{t}$ and Wt at NLO [120]. The latter is estimated by comparing the nominal sample, which uses the so-called "diagram subtraction" scheme, with an alternative sample using the "diagram removal" scheme.

Uncertainties on the diboson background normalisation include 5% from the NLO theoretical cross sections [105] added in quadrature to an uncertainty of 24% due to the extrapolation to the high jet multiplicity channels, following the procedure discussed in Sect. 10.3.2.

Uncertainties on the $t\bar{t}V$ and $t\bar{t}H$ normalisations are 30% and +9%/−12% respectively, from the uncertainties on their respective NLO theoretical cross sections [107, 108, 117]. Additional small uncertainties arising from scale variations, which change the amount of initial-state radiation and thus the event kinematics, are also included.

10.3.4. Multijet

Uncertainties on the multijet background estimate via the MM receive contributions from the limited data statistics, particularly at high jet and b-tag multiplicities, as well as from the uncertainty on the rate of fake leptons, estimated in different control regions (e.g. selected with either an upper $E_{\mathrm{T}}^{\mathrm{miss}}$ or $m_{\mathrm{T}}^{\mathrm{W}}$

requirement). A combined normalisation uncertainty of 50% due to all these effects is assigned, which is taken as correlated across jet and b-tag multiplicity bins, but uncorrelated between electron and muon channels. No explicit shape uncertainty is assigned since the limited statistics in the multijet prediction leads to large statistical uncertainties that are uncorrelated bin-to-bin in the final discriminating variable and thus cover all possible shape uncertainties.

11. Statistical analysis

For a given search, the distributions of the final discriminating variables in each of the analysis channels considered are combined to test for the presence of a signal. The statistical analysis is based on a binned likelihood function $\mathcal{L}(\mu,\theta)$ constructed as a product of Poisson probability terms over all bins considered in the analysis. This function depends on the signal strength parameter μ, a multiplicative factor to the theoretical signal production cross section, and θ, a set of nuisance parameters that encode the effect of systematic uncertainties on the signal and background expectations and are implemented in the likelihood function as Gaussian or log-normal priors. Therefore, the total number of expected events in a given bin depends on μ and θ. The nuisance parameters θ allow adjustments of the expectations for signal and background according to the corresponding systematic uncertainties, and their fitted values correspond to the deviations from the nominal expectations that globally provide the best fit to the data. This procedure allows a reduction of the impact of systematic uncertainties on the search sensitivity by taking advantage of the high-statistics background-dominated channels included in the likelihood fit. It requires a good understanding of the systematic effects affecting the shapes of the discriminant distributions. To verify the improved background prediction, fits are performed under the background-only hypothesis. The agreement between data and background prediction is checked within the smaller post-fit uncertainties in kinematic variables other than the ones used in the fit.

The test statistic q_μ is defined as the profile likelihood ratio: $q_\mu = -2\ln(\mathcal{L}(\mu,\hat{\hat{\theta}}_\mu)/\mathcal{L}(\hat{\mu},\hat{\theta}))$, where $\hat{\mu}$ and $\hat{\theta}$ are the values of the parameters that maximise the likelihood function (with the constraint $0 \leq \hat{\mu} \leq \mu$), and $\hat{\hat{\theta}}_\mu$ are the values of the nuisance parameters that maximise the likelihood function for a given value of μ. Statistical uncertainties in each bin of the discriminant distributions are also taken into account via dedicated parameters in the fit. The test statistic q_μ is implemented in the RooFit package [121, 122] and is used to measure the compatibility of the observed data with the background-only hypothesis (i.e. the discovery test) setting $\mu = 0$ in the profile likelihood ratio: $q_0 = -2\ln(\mathcal{L}(0,\hat{\hat{\theta}}_0)/\mathcal{L}(\hat{\mu},\hat{\theta}))$. The p-value (referred to as p_0) representing the compatibility of the data with the background-only hypothesis is estimated by integrating the distribution of q_0 from background-only pseudo-experiments, approximated using the asymptotic formulae given in Ref. [123], above the observed value of q_0. Some model-dependence exists in the estimation of the p_0 value, as a given signal scenario needs to be assumed in the calculation of the denominator of q_μ, even if the overall signal normalisation is left floating and fitted to data. The observed p_0 is checked for each explored signal scenario. In absence of any significant excess above the background expectation, upper limits on the signal production cross section for each of the signal scenarios considered are derived by using q_μ in the CL_s method [124, 125]. For a given signal scenario, values of the production cross section (parameterised by μ) yielding $CL_s<0.05$, where CL_s is computed using the asymptotic approximation [123], are excluded at $\geq$95% CL.

12. Results

This section presents the results obtained from the searches discussed in Sections 7–9, following the statistical analysis discussed in Section 11.

12.1. Likelihood fits to data

The consideration of high-statistics background-dominated channels in the analysis allows an improved background prediction with significantly reduced systematic uncertainties to be obtained during the statistical analysis, as discussed in Section 11. This is the strategy adopted by the $T\bar{T} \to Ht$+X and $B\bar{B} \to Hb$+X searches, which also results in an improved search sensitivity. Figures 14 and 15 show the comparison of data and the post-fit background prediction for the H_{T} distributions in each of the analysis channels considered by the $T\bar{T} \to Ht$+X search. The corresponding comparisons for the $B\bar{B} \to Hb$+X search can be found in Figs. 16 and 17. The fit to the data is performed under the background-only hypothesis. Tables with the corresponding predicted and observed yields per channel can be found in Appendix B.

Compared to the pre-fit distributions shown in Sects. 8 and 9, the total background uncertainty is significantly reduced after the fit, not only in the background-dominated channels, but also in the signal-rich channels. The reduced uncertainty results from the significant constraints provided by the data on some systematic uncertainties, as well as the anti-correlations among sources of systematic uncertainty resulting from the fit to the data. For example, the uncertainty in the $t\bar{t}$+$b\bar{b}$ background in the highest-sensitivity channel (≥6 j, ≥4 b, high $M_{bb}^{\mathrm{min}\Delta R}$) is reduced from about 60% prior to the fit to about 15% and 30% in the $T\bar{T} \to Ht$+X and the $B\bar{B} \to Hb$+X searches respectively. The larger post-fit uncertainty in the case of $B\bar{B} \to Hb$+X search is partly caused by the smaller available data statistics due to the tighter selection requirements compared to the $T\bar{T} \to Ht$+X search. A more detailed comparison between pre-fit and post-fit uncertainties for the different sources of systematic uncertainty and background processes is shown in Appendix A. In contrast, the low data statistics in the $T\bar{T} \to Wb$+X search results in virtually the same background prediction and uncertainties both pre-fit and post-fit.

12.2. Limits on $T\bar{T}$ production

The consistency of the data with the background prediction is assessed by computing the p_0-value for each signal scenario considered. In the case of the $T\bar{T} \to Wb$+X search, the smallest p_0-value found, 0.023, is obtained for $m_T = 600$ GeV, $BR(T \to Wb) = 0.30$ and $BR(T \to Ht) = 0.65$ ($BR(T \to Zt) = 1 - BR(T \to Wb) - BR(T \to Ht) = 0.05$), and corresponds to a local significance of 2.0 standard deviations above the background-only prediction. In the case of the $T\bar{T} \to Ht$+X search, the smallest p_0-value found, 0.44, is obtained for $m_T = 600$ GeV, $BR(T \to Wb) = 0.0$, $BR(T \to Ht) = 0.0$, and $BR(T \to Zt) = 1.0$, and corresponds to a local significance of 0.2 standard deviations above the background-only prediction. Thus, no significant excess above the background expectation is found in either of the two searches.

Since the two searches have complementary sensitivity to different decay modes of a T quark, they are combined in a single likelihood function taking into account the correlation of systematic uncertainties. Upper limits at 95% CL on the $T\bar{T}$ production cross section are set in several benchmark scenarios as a function of the T quark mass m_T and are compared to the theoretical prediction from Top++, as shown in

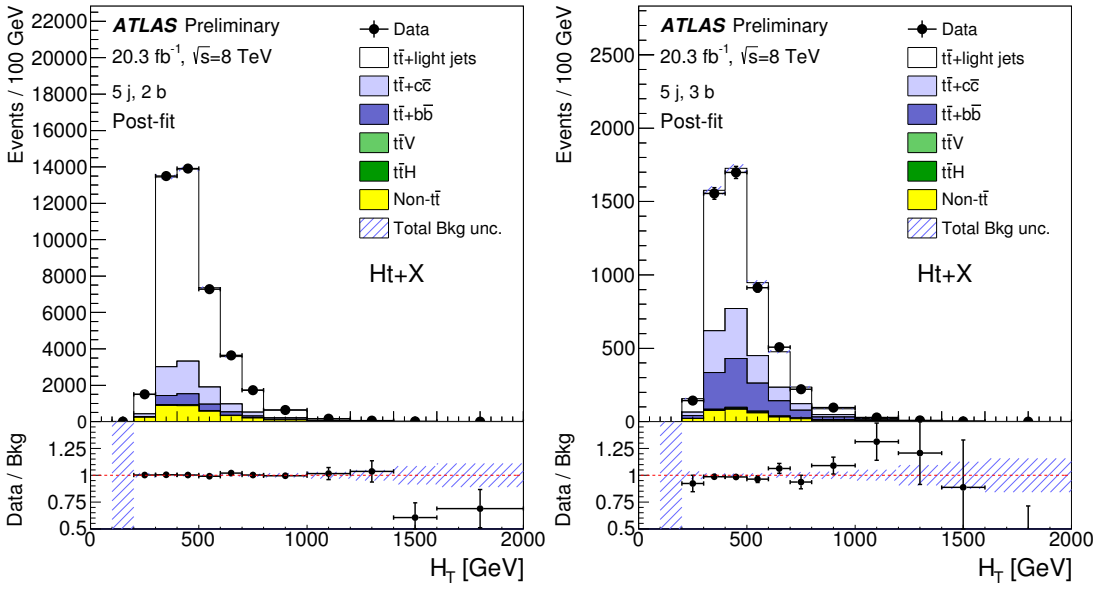

Figure 14: $T\bar{T} \rightarrow Ht$+X search: comparison between data and prediction for the distribution of the scalar sum of the transverse momenta of the lepton, the selected jets and the missing transverse momentum (H_{T}) in each of the analysed channels: (a) (5 j, 2 b), (b) (5 j, 3 b), (c) (5 j, ≥4 b), and (d) (≥6 j, 2 b). The background prediction is shown after the fit to data under the background-only hypothesis. The small contributions from W/Z+jets, single top, diboson and multijet backgrounds are combined into a single background source referred to as "Non-$t\bar{t}$". The last bin in all figures contains the overflow. The bottom panel displays the ratio between data and total background prediction. The hashed area represents the total uncertainty on the background.

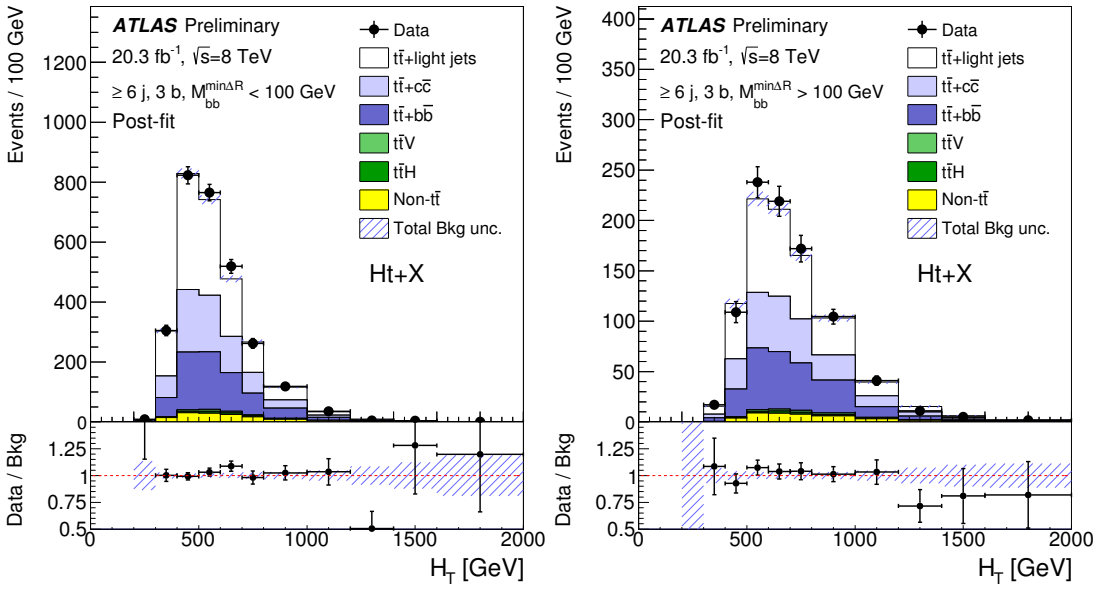

(a)

(b)

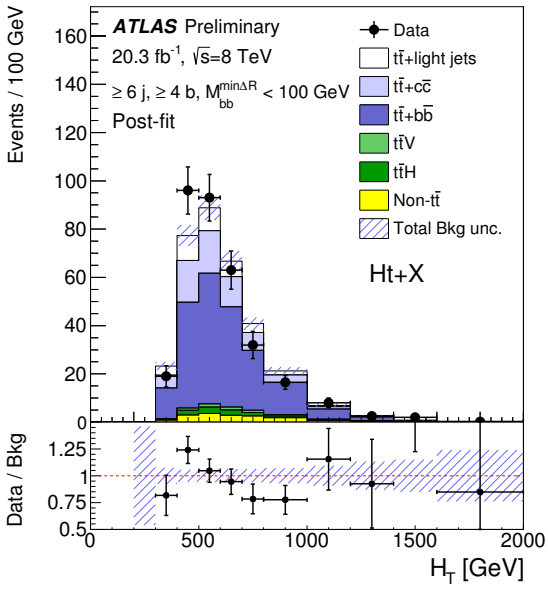

(c)

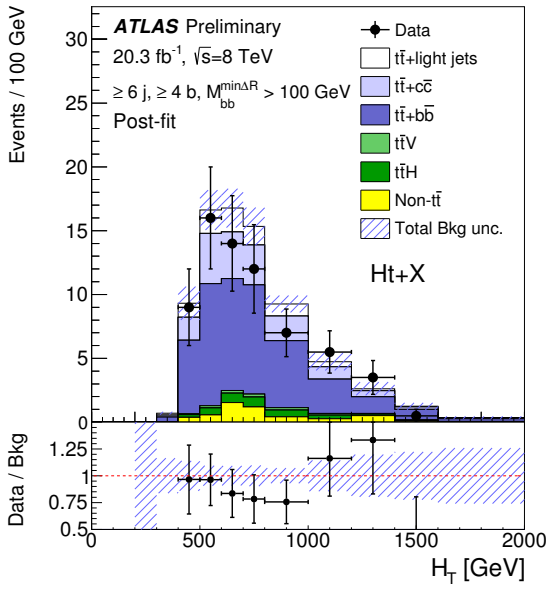

(d)

Figure 15: $T\bar{T} \rightarrow Ht$+X search: comparison between data and prediction for the distribution of the scalar sum of the transverse momenta of the lepton, the selected jets and the missing transverse momentum (H_{T}) in each of the analysed channels: (a) (≥6 j, 3 b, low $M_{bb}^{\mathrm{min}\Delta R}$), (b) (≥6 j, 3 b, high $M_{bb}^{\mathrm{min}\Delta R}$), (c) (≥6 j, ≥4 b, low $M_{bb}^{\mathrm{min}\Delta R}$), and (d) (≥6 j, ≥4 b, high $M_{bb}^{\mathrm{min}\Delta R}$). The background prediction is shown after the fit to data under the background-only hypothesis. The small contributions from W/Z+jets, single top, diboson and multijet backgrounds are combined into a single background source referred to as "Non-$t\bar{t}$". The last bin in all figures contains the overflow. The bottom panel displays the ratio between data and total background prediction. The hashed area represents the total uncertainty on the background.

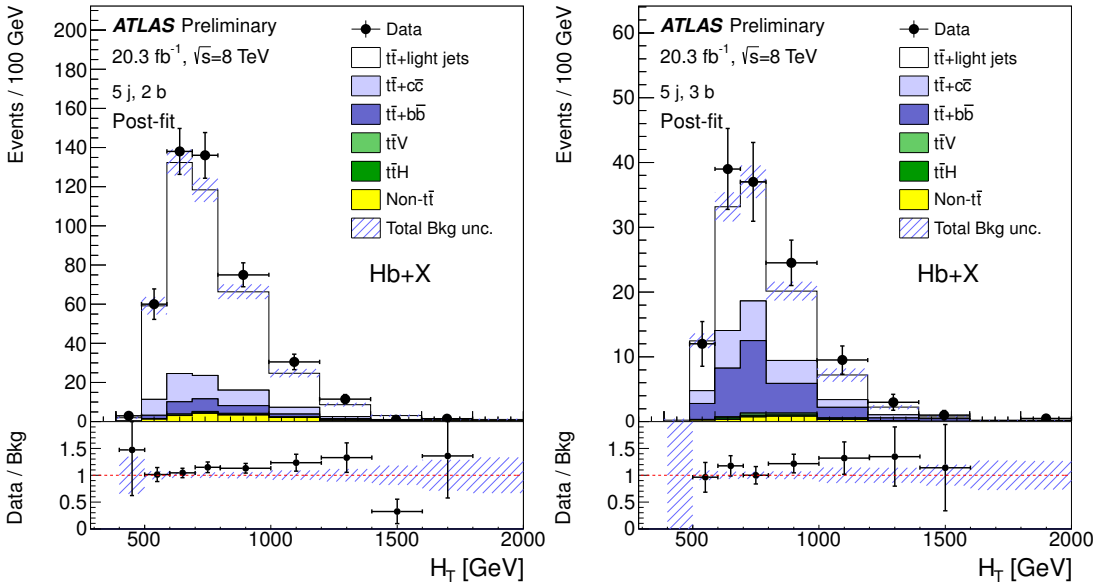

(a) (b)

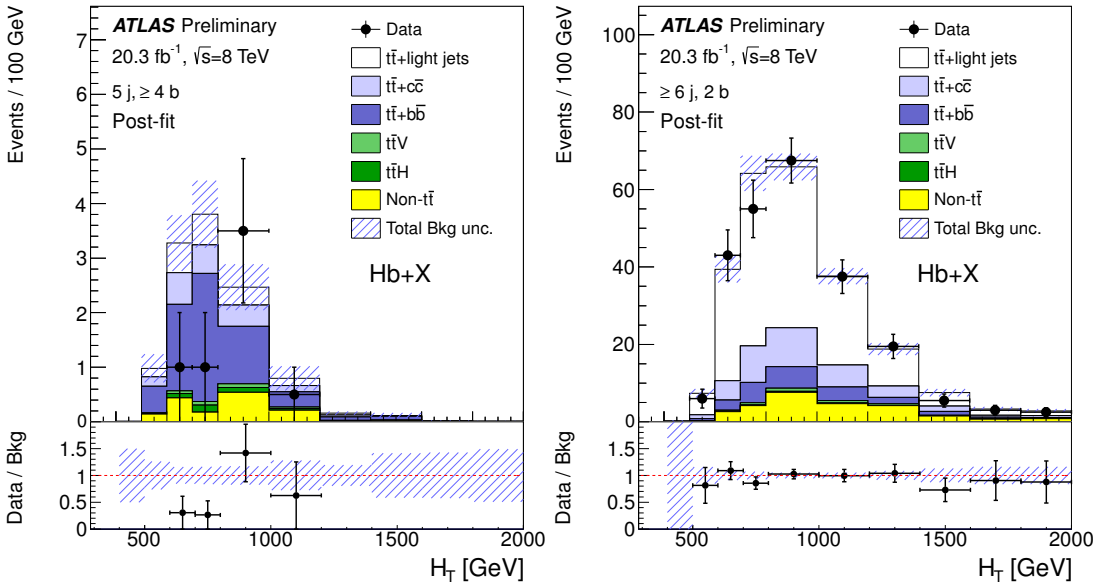

(c) (d)

Figure 16: $B\bar{B} \to Hb$+X search: comparison between data and prediction for the distribution of the scalar sum of the transverse momenta of the lepton, the selected jets and the missing transverse momentum (H_{T}) in each of the analysed channels: (a) (5 j, 2 b), (b) (5 j, 3 b), (c) (5 j, ≥4 b), and (d) (≥6 j, 2 b). The background prediction is shown after the fit to data under the background-only hypothesis. The small contributions from W/Z+jets, single top, diboson and multijet backgrounds are combined into a single background source referred to as "Non-$t\bar{t}$". The last bin in all figures contains the overflow. The bottom panel displays the ratio between data and total background prediction. The hashed area represents the total uncertainty on the background.

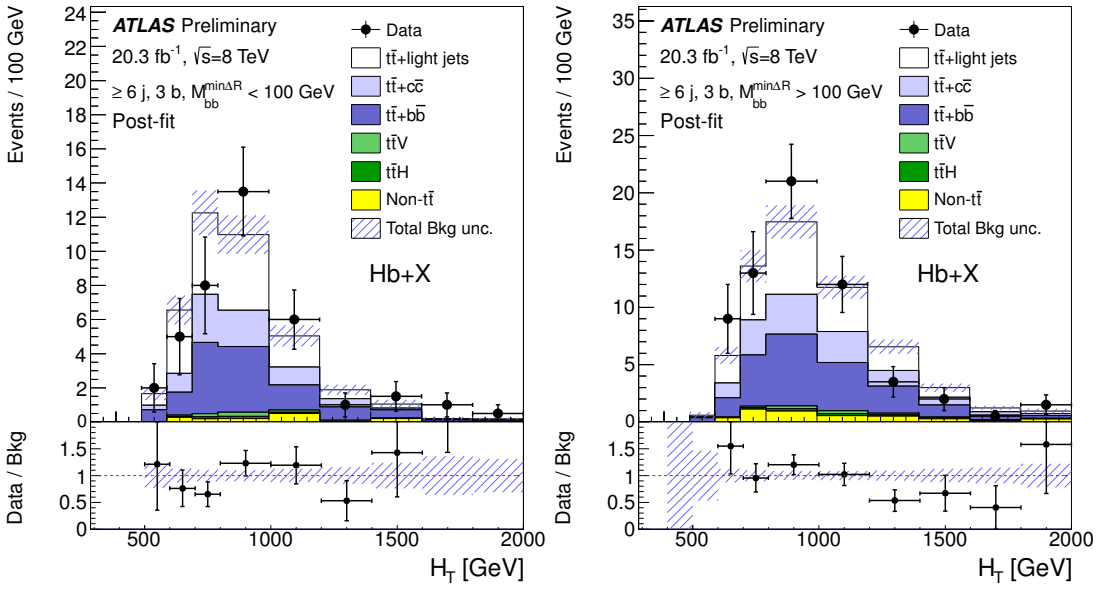

(a) (b)

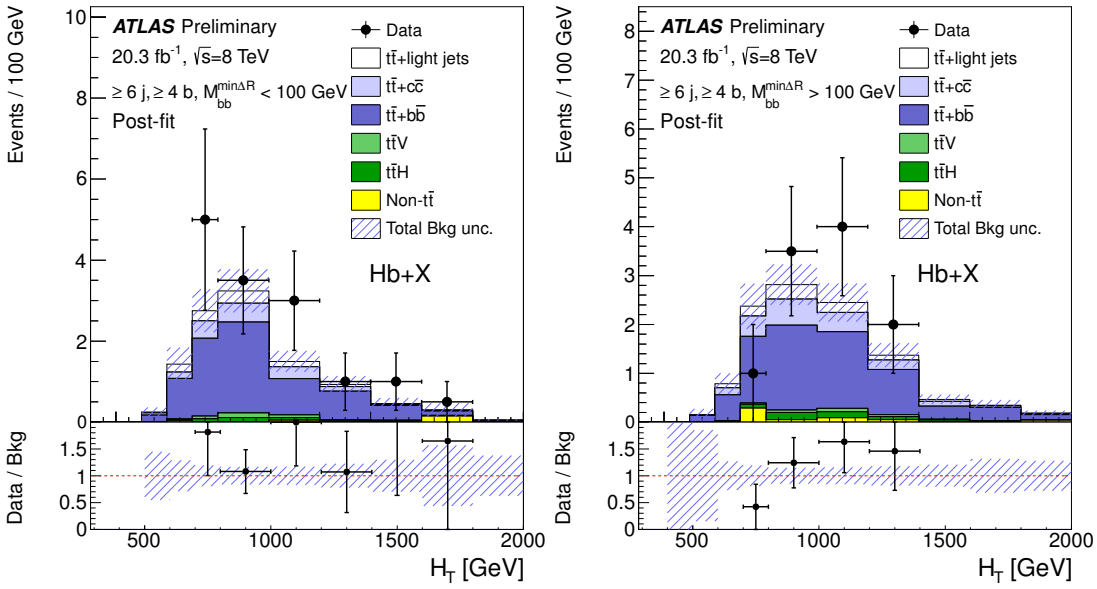

(c) (d)

Figure 17: $B\bar{B} \to Hb$+X search: comparison between data and prediction for the distribution of the scalar sum of the transverse momenta of the lepton, the selected jets and the missing transverse momentum (H_{T}) in each of the analysed channels: (a) (≥6 j, 3 b, low $M_{bb}^{\mathrm{min}\Delta R}$), (b) (≥6 j, 3 b, high $M_{bb}^{\mathrm{min}\Delta R}$), (c) (≥6 j, ≥4 b, low $M_{bb}^{\mathrm{min}\Delta R}$), and (d) (≥6 j, ≥4 b, high $M_{bb}^{\mathrm{min}\Delta R}$). The background prediction is shown after the fit to data under the background-only hypothesis. The small contributions from W/Z+jets, single top, diboson and multijet backgrounds are combined into a single background source referred to as "Non-$t\bar{t}$". The last bin in all figures contains the overflow. The bottom panel displays the ratio between data and total background prediction. The hashed area represents the total uncertainty on the background.

Fig. 18. The resulting lower limits on m_T correspond to the central value of the theoretical cross section. The scenarios considered include a chiral fourth-generation T quark, and a vector-like singlet and doublet T quark. Only the $T\bar{T} \to Wb$+X search is sensitive to a chiral fourth-generation T quark, yielding an observed (expected) 95% CL lower limit of $m_T > 770\,(795)$ GeV. This represents the most stringent limit to date, and is also applicable to a Y vector-like quark with electric charge of $-4/3$ and decaying into a W^- boson and a b quark. Both searches are sensitive to a vector-like singlet T quark. The $T\bar{T} \to Wb$+X and $T\bar{T} \to Ht$+X searches yield observed (expected) 95% CL limits of $m_T > 660\,(670)$ GeV and $m_T > 765\,(720)$ GeV respectively. The combination of both analyses results in a slight improvement over the $T\bar{T} \to Ht$+X search alone, yielding $m_T > 800\,(755)$ GeV. Finally, only the $T\bar{T} \to Ht$+X search is sensitive to a vector-like doublet T quark, yielding an observed (expected) 95% CL lower limit of $m_T > 855\,(820)$ GeV.

The same searches are used to derive exclusion limits on vector-like T quark production for different values of m_T and as a function of the two branching ratios $BR(T \to Wb)$ and $BR(T \to Ht)$. To probe this branching ratio plane, the signal samples are reweighted by the ratio of the desired branching ratio to the original branching ratio in Protos, and the complete analysis is repeated. The resulting 95% CL exclusion limits are shown in Fig. 19 for the combination of the $T\bar{T} \to Wb$+X and $T\bar{T} \to Ht$+X searches, for different values of m_T. Figure 20 presents the corresponding observed and expected T quark mass limits in the plane of $BR(T \to Ht)$ versus $BR(T \to Wb)$. The combined results set observed lower limits on the T quark mass ranging between 715 GeV and 950 GeV for all possible values of the branching ratios into the three decay modes. This implies that any branching ratio scenario is excluded at 95% CL for a T quark with mass below 715 GeV. The corresponding range of expected lower limits is between 675 GeV and 885 GeV. The exclusion limits for the individual searches can be found in Appendix C. These figures illustrate the complementarity of these searches and how their combination improves over simply taking the most sensitive search for each assumed branching ratio scenario, leading to large regions in the branching ratio plane being excluded.

12.3. Limits on $B\bar{B}$ production

In the case of the $B\bar{B} \to Hb$+X search, the smallest p_0-value found, 0.023, is obtained for $m_B = 450$ GeV, $BR(B \to Wt) = 0.0$ and $BR(B \to Hb) = 0.3$ ($BR(B \to Zb) = 1 - BR(B \to Wt) - BR(B \to Hb) = 0.7$), and corresponds to a local significance of 2.0 standard deviations above the background-only prediction.

Upper limits at 95% CL on the $B\bar{B}$ production cross section are set for two benchmark scenarios as a function of the B quark mass, as shown in Fig. 21. Assuming a branching ratio $BR(B \to Hb) = 1$, the intervals $350 < m_B < 580$ GeV and $635 < m_B < 700$ GeV are excluded at 95% CL. The expected exclusion is $m_B > 625$ GeV at 95% CL. For branching ratios corresponding to a B singlet, the observed (expected) 95% CL limit is $m_B > 735\,(635)$ GeV. Exclusion limits are set for values of m_B and as a function of the two branching ratios $BR(B \to Wt)$ and $BR(B \to Hb)$, shown in Fig. 22. The search shows sensitivity in particular at large branching ratio $BR(B \to Hb)$, but also at large branching ratio $BR(B \to Wt)$. Figure 23 presents the corresponding observed and expected B quark mass limits in the plane of $BR(B \to Hb)$ versus $BR(B \to Wt)$.

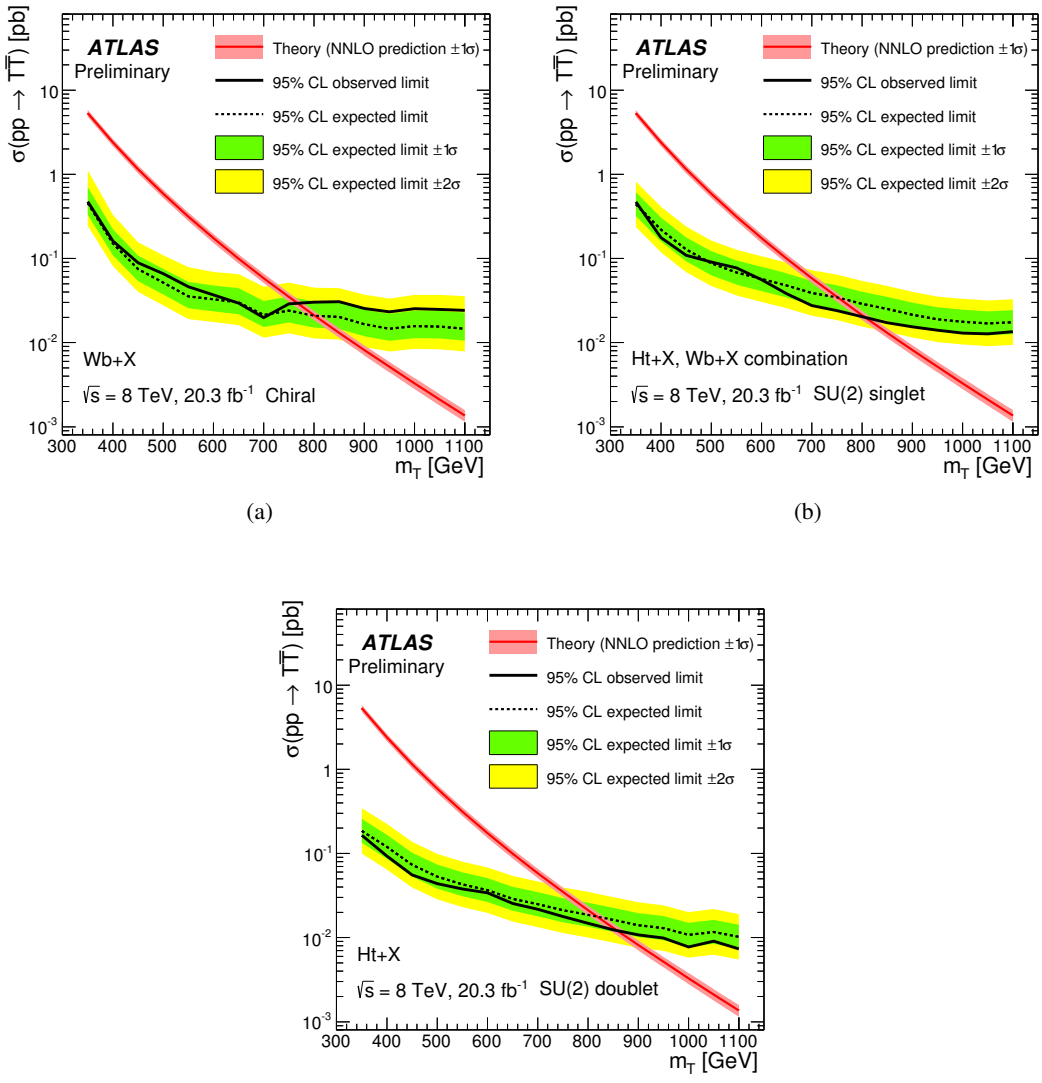

(a)

(b)

(c)

Figure 18: Observed (solid line) and expected (dashed line) 95% CL upper limits on the $T\bar{T}$ cross section as a function of the T quark mass for (a) a chiral fourth-generation T quark, (b) a vector-like singlet T quark, and (c) a vector-like doublet T quark. The surrounding shaded bands correspond to ±1 and ±2 standard deviations around the expected limit. The thin red line and band show the theoretical prediction and its ±1 standard deviation uncertainty.

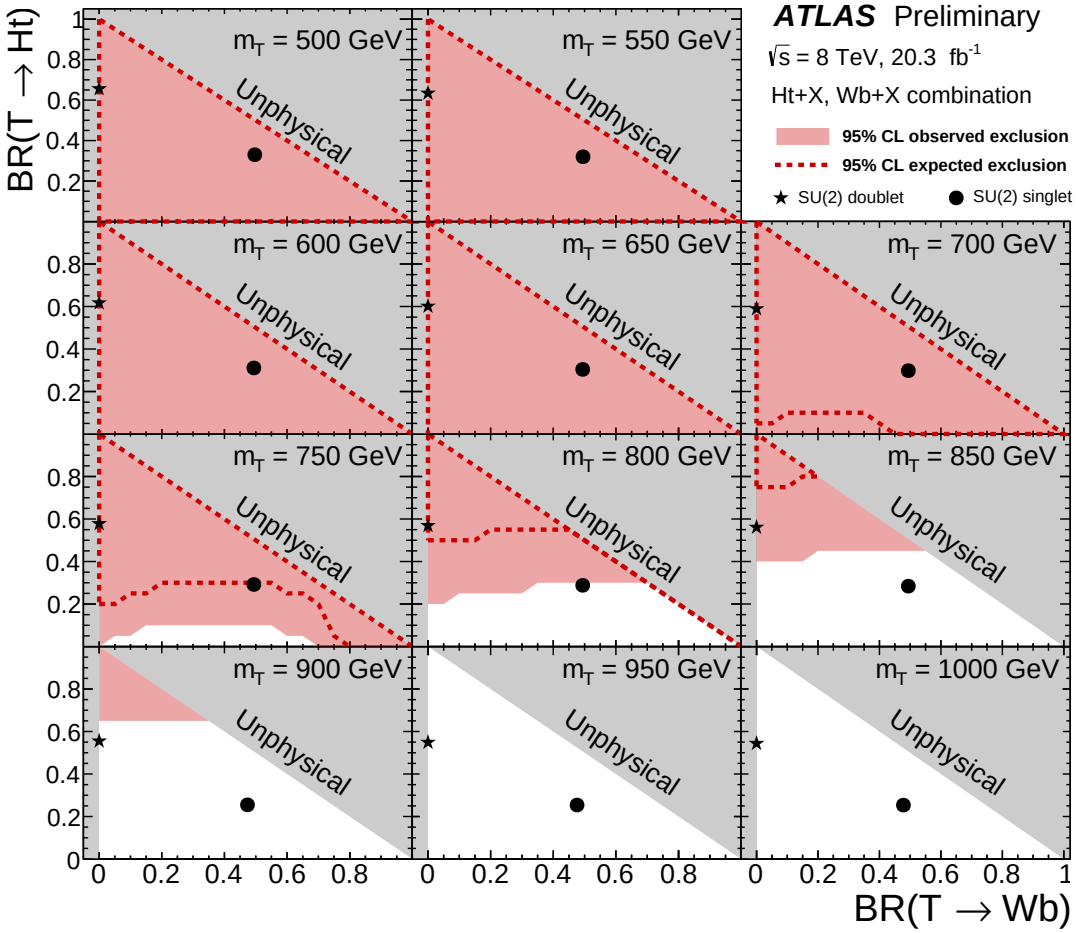

Figure 19: Observed (red filled area) and expected (red dashed line) 95% CL exclusion in the plane of $BR(T \to Wb)$ versus $BR(T \to Ht)$ from the combination of the $T\bar{T} \to Wb$+X and $T\bar{T} \to Ht$+X searches, for different values of the vector-like T quark mass. The grey (dark shaded) area corresponds to the unphysical region where the sum of branching ratios exceeds unity. The default branching ratio values from the PROTOS event generator for the weak-isospin singlet and doublet cases are shown as plain circle and star symbols respectively.

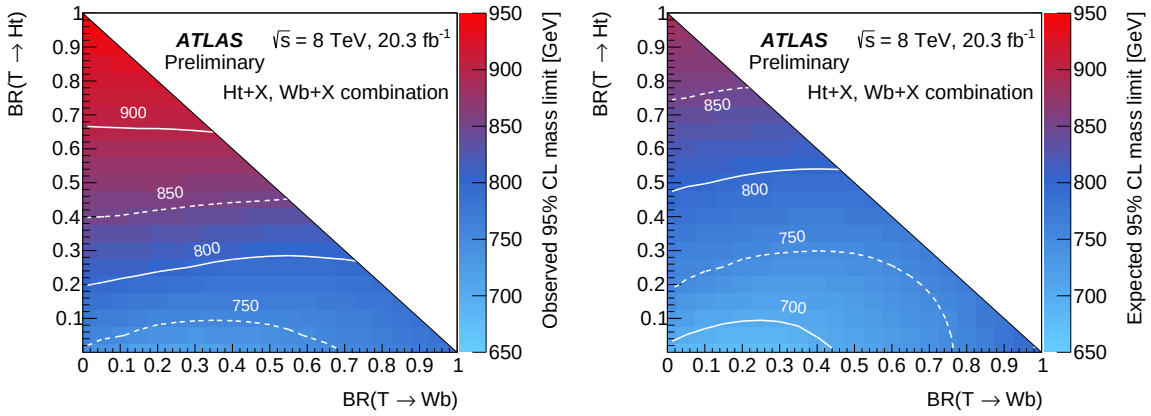

(a) (b)

Figure 20: Observed (a) and expected (b) limit (95% CL) on the mass of the T quark from the the combination of the $T\bar{T} \to Wb$+X and $T\bar{T} \to Ht$+X searches, and presented in the plane of $BR(T \to Ht)$ versus $BR(T \to Wb)$.

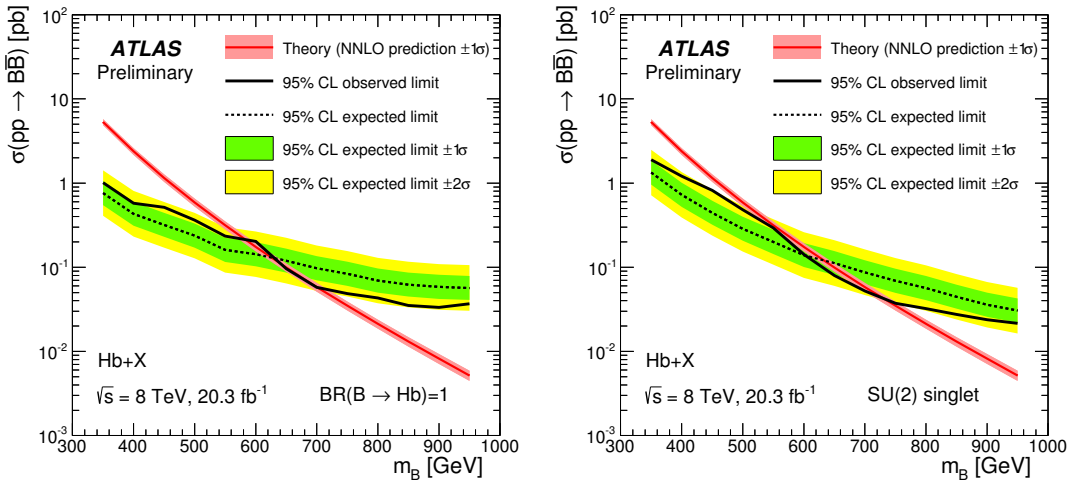

(a) (b)

Figure 21: Observed (solid line) and expected (dashed line) 95% CL upper limits on the $B\bar{B}$ cross section as a function of the B quark mass (a) under the assumption $BR(B \to Hb) = 1$ and (b) for a B quark singlet. The surrounding shaded bands correspond to ±1 and ±2 standard deviations around the expected limit. The thin red line and band show the theoretical prediction and its ±1 standard deviation uncertainty.

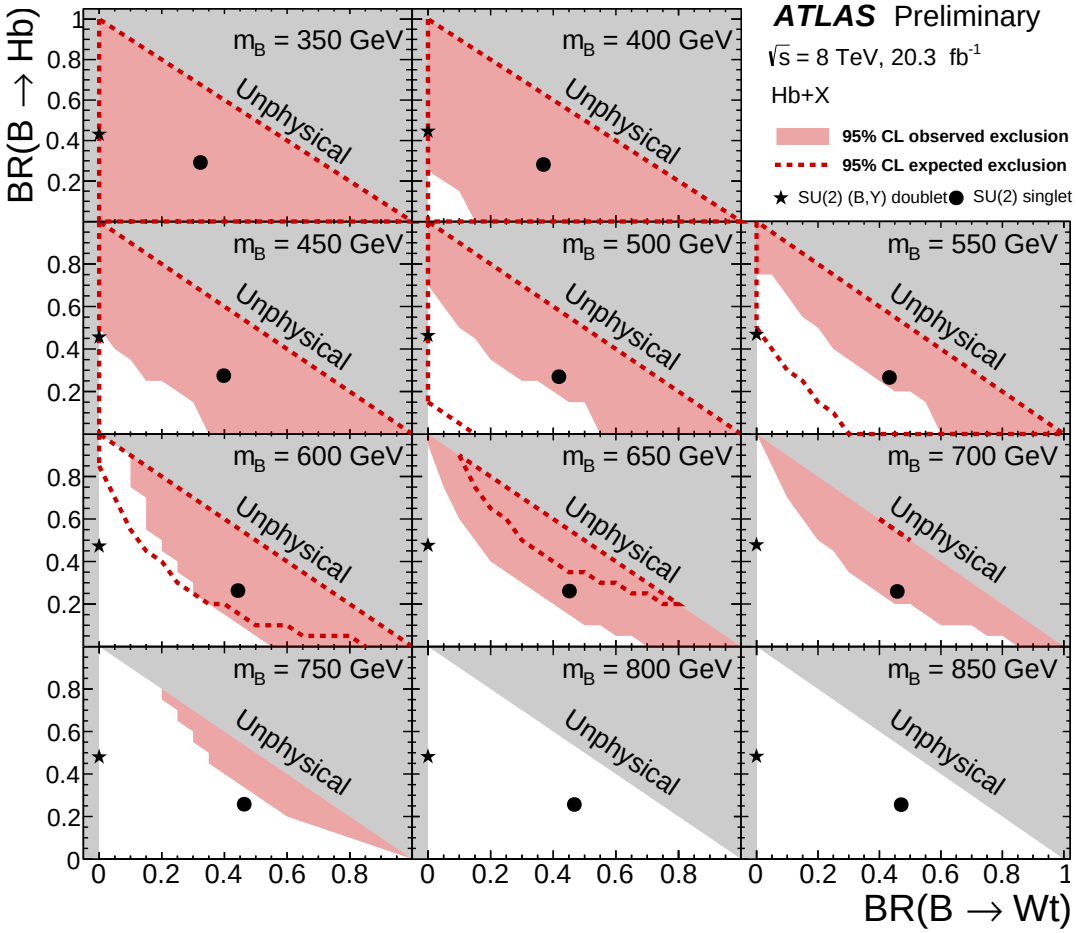

Figure 22: Observed (red filled area) and expected (red dashed line) 95% CL exclusion in the plane of $BR(B \to Wt)$ versus $BR(B \to Hb)$ from the $B\bar{B} \to Hb$+X search, for different values of the vector-like B quark mass. The grey (dark shaded) area corresponds to the unphysical region where the sum of branching ratios exceeds unity. The default branching ratio values from the Protos event generator for the weak-isospin singlet and (B,Y) doublet cases are shown as plain circle and star symbols respectively.

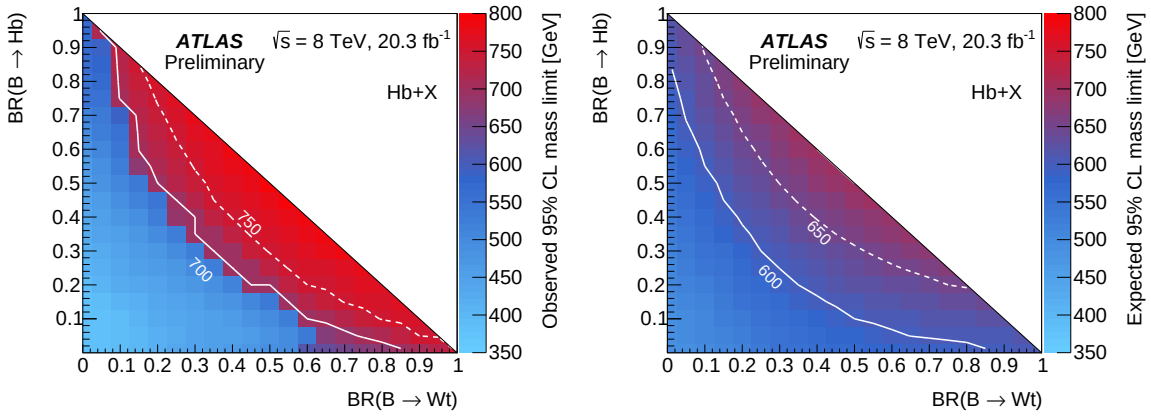

(a) (b)

Figure 23: Observed (a) and expected (b) limit (95% CL) on the mass of the B quark from the $B\bar{B} \to Hb$+X search, and presented in the plane of $BR(B \to Hb)$ versus $BR(B \to Wt)$.

12.4. Limits on $t\bar{t}t\bar{t}$ production

As discussed previously, the Ht+X analysis is also used to set limits on four-top-quark production considering different signal benchmark scenarios: SM-like $t\bar{t}t\bar{t}$, $t\bar{t}t\bar{t}$ via an EFT model with a four-top contact interaction, sgluon pair production with decay into $t\bar{t}$, and a Universal Extra Dimension (UED) model with two extra dimensions compactified under the Real Projective Plane (RPP) geometry. Except for the case of SM-like $t\bar{t}t\bar{t}$ production, for which the ATLAS multilepton search [27] achieves the best expected sensitivity, in all other benchmark scenarios this analysis achieves the most restrictive expected bounds.

In case of $t\bar{t}t\bar{t}$ production with the SM kinematics, the observed (expected) 95% CL upper limit on the production cross section is 34 (47) times the SM prediction, or 23 fb (32 fb). In this scenario the expected sensitivity of this analysis is comparable to that of the ATLAS multilepton search [27], for which the expected limit is 27 fb. In case of $t\bar{t}t\bar{t}$ production via an EFT model with a four-top contact interaction, the observed (expected) 95% CL upper limit on the production cross section is 12 fb (16 fb). The improved sensitivity in the case of the EFT model results from the harder H_{T} spectrum compared to that of SM $t\bar{t}t\bar{t}$ production. The upper limit on the production cross section can be translated into an observed (expected) limit on the free parameter of the model $|C_{4t}|/\Lambda^2 < 6.6$ (7.7).

The resulting observed and expected upper limits on the sgluon pair production cross section times branching ratio are shown in Fig. 24 as a function of the sgluon mass and are compared to the theoretical prediction. This translates into an observed (expected) 95% CL limit on the sgluon mass of 1.06 TeV (1.02 TeV).

Finally, the observed and expected upper limits on the production cross section times branching ratio are shown in Fig. 25 as a function of m_{KK} for the symmetric case ($\xi = R_4/R_5 = 1$), assuming production by tier (1,1) alone. The comparison to the LO theoretical cross section translates into an observed (expected) 95% CL limit on m_{KK} of 1.12 TeV (1.10 TeV). As mentioned before, four-top-quark events can also arise from tiers (2,0) and (0,2). In those tiers the theoretical production cross sections can be calculated, leading to more robust results (i.e. there is no need to make an assumption on a branching ratio). The dependence of the tier kinematics on the tier mass also allows the extrapolation of constraints on tier

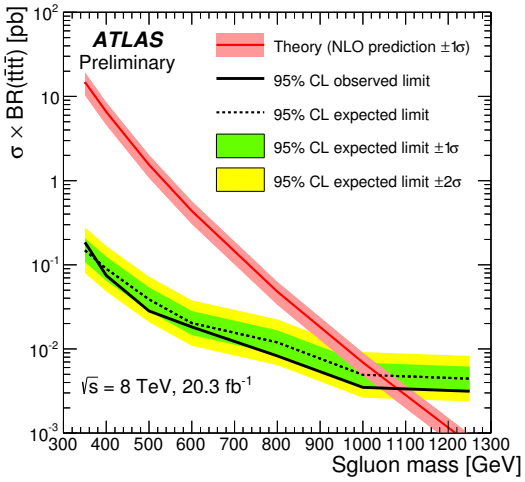

Figure 24: Observed (solid line) and expected (dashed line) 95% CL upper limits on the sgluon pair production cross section times branching ratio as a function of the sgluon mass. The surrounding shaded bands correspond to ±1 and ±2 standard deviations around the expected limit. The thin red line and band show the theoretical prediction and its ±1 standard deviation uncertainty.

(1,1) to tiers (2, 0) and (0, 2). Excluding a given production cross section for tier (1,1) at a given m_{KK} is equivalent to excluding this production cross section for tier (2, 0) alone at $m_{KK}/\sqrt{2}$ and for tier (0, 2) at $m_{KK}/\sqrt{2}\xi$. The contribution of tier (0,2) vanishes as ξ increases (highly-asymmetric case). Figure 26 presents the observed and expected upper limits on the production cross section times branching ratio as function of m_{KK} for two scenarios: tiers (2,0)+(0,2) alone in the symmetric case, and tier (2,0) alone in the highly-asymmetric case. In both cases a branching ratio of $A^{(1,1)} \to t\bar{t}$ of 0% is assumed. The corresponding observed (expected) 95% CL limits on m_{KK} are 0.61 TeV (0.60 TeV) and 0.57 TeV (0.55 TeV) respectively.

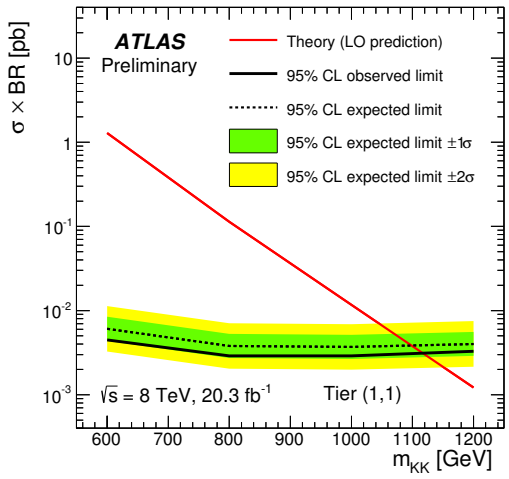

Figure 25: Observed (solid line) and expected (dashed line) 95% CL upper limits on the production cross section times branching ratio of four-top-quark events as a function of Kaluza-Klein mass (m_{KK}) from tier (1,1) in the symmetric case. The surrounding shaded bands correspond to ±1 and ±2 standard deviations around the expected limit. The thin red line shows the theoretical prediction for the production cross section of four-top-quark events by tier (1,1) assuming $BR(A^{(1,1)} \to t\bar{t}) = 1$, where $A^{(1,1)}$ is the lightest particle of this tier.

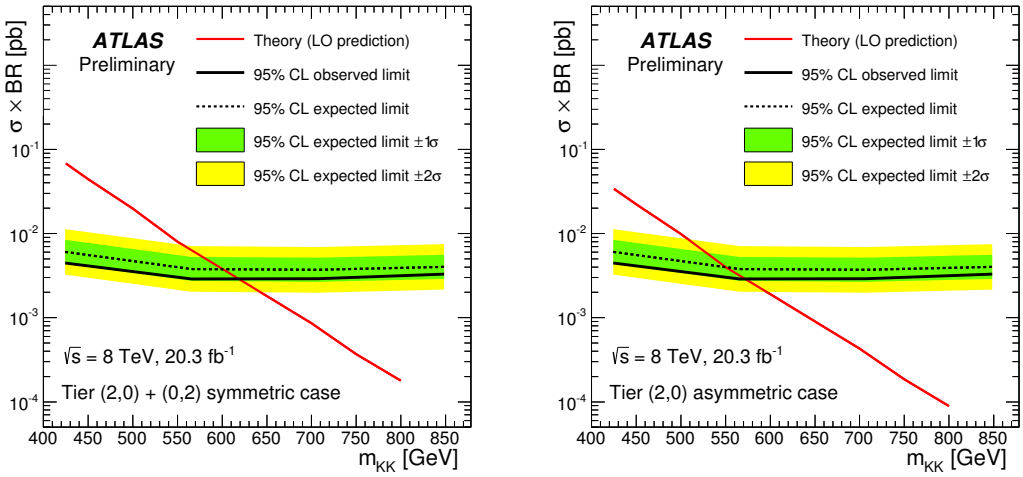

(a) (b)

Figure 26: Observed (solid line) and expected (dashed line) 95% CL upper limits on the production cross section times branching ratio of four-top-quark events as a function of Kaluza-Klein mass (m_{KK}) from (left) tiers (2,0)+(0,2) alone in the symmetric case and (right) tier (2,0) alone in the highly-asymmetric case. The surrounding shaded bands correspond to ±1 and ±2 standard deviations around the expected limit. The thin red line shows the theoretical prediction for the production cross section of four-top-quark events.

13. Conclusion

A search for pair production of vector-like quarks, both up-type (T) and down-type (B), as well as four-top-quark production has been performed using 20.3 fb^{-1} of pp collision data at $\sqrt{s} = 8$ TeV recorded with the ATLAS detector at the CERN Large Hadron Collider. Data are analysed in the lepton+jets final state, characterised by a high-transverse-momentum isolated electron or muon, large missing transverse momentum and at least four jets. Dedicated analyses are performed targeting three cases: a T quark with significant branching to a W boson and a b quark ($T\bar{T} \rightarrow Wb$+X), and both a T quark and a B quark with significant branching ratio to a Higgs boson and third generation quark ($T\bar{T} \rightarrow Ht$+X and $B\bar{B} \rightarrow Hb$+X respectively). The analyses exploit characteristic features of the signals to discriminate against the dominant background from top quark pair production, such as the high total transverse momenta of all final state objects, the presence of boosted hadronically-decaying W bosons, or the presence of Higgs bosons decaying into $b\bar{b}$, resulting in high b-jet multiplicity. No significant excess of events above the Standard Model expectation is observed, and lower limits are derived on the masses of the vector-like T and B quarks under several branching ratio hypotheses assuming contributions from $T \rightarrow Wb$, Zt, Ht and $B \rightarrow Wt$, Zb, Hb decays. The observed lower limits on the T quark mass range between 715 GeV and 950 GeV for all possible values of the branching ratios into the three possible decay modes, representing the most stringent constraints to date. In addition, one of the analyses is used to search for four-top-quark production, both within the Standard Model and in several new physics scenarios, resulting in some of the most restrictive existing bounds on this process.

Acknowledgements

We thank CERN for the very successful operation of the LHC, as well as the support staff from our institutions without whom ATLAS could not be operated efficiently.

We acknowledge the support of ANPCyT, Argentina; YerPhI, Armenia; ARC, Australia; BMWFW and FWF, Austria; ANAS, Azerbaijan; SSTC, Belarus; CNPq and FAPESP, Brazil; NSERC, NRC and CFI, Canada; CERN; CONICYT, Chile; CAS, MOST and NSFC, China; COLCIENCIAS, Colombia; MSMT CR, MPO CR and VSC CR, Czech Republic; DNRF, DNSRC and Lundbeck Foundation, Denmark; EPLANET, ERC and NSRF, European Union; IN2P3-CNRS, CEA-DSM/IRFU, France; GNSF, Georgia; BMBF, DFG, HGF, MPG and AvH Foundation, Germany; GSRT and NSRF, Greece; ISF, MINERVA, GIF, I-CORE and Benoziyo Center, Israel; INFN, Italy; MEXT and JSPS, Japan; CNRST, Morocco; FOM and NWO, Netherlands; BRF and RCN, Norway; MNiSW and NCN, Poland; GRICES and FCT, Portugal; MNE/IFA, Romania; MES of Russia and ROSATOM, Russian Federation; JINR; MSTD, Serbia; MSSR, Slovakia; ARRS and MIZŠ, Slovenia; DST/NRF, South Africa; MINECO, Spain; SRC and Wallenberg Foundation, Sweden; SER, SNSF and Cantons of Bern and Geneva, Switzerland; NSC, Taiwan; TAEK, Turkey; STFC, the Royal Society and Leverhulme Trust, United Kingdom; DOE and NSF, United States of America.

The crucial computing support from all WLCG partners is acknowledged gratefully, in particular from CERN and the ATLAS Tier-1 facilities at TRIUMF (Canada), NDGF (Denmark, Norway, Sweden), CC-IN2P3 (France), KIT/GridKA (Germany), INFN-CNAF (Italy), NL-T1 (Netherlands), PIC (Spain), ASGC (Taiwan), RAL (UK) and BNL (USA) and in the Tier-2 facilities worldwide.

Appendix

A. Systematic uncertainties for the individual searches

Table 6 presents a summary of the systematic uncertainties for the $T\bar{T} \to Wb$+X search with the impact on the normalisation of signal and backgrounds. A similar summary is presented for the $T\bar{T} \to Ht$+X and $B\bar{B} \to Hb$+X searches in Tables 7 and 8 respectively, restricted to the highest-sensitivity channel and displaying only the signal and the $t\bar{t}$+jets background categories. These tables also show the impact of the systematic uncertainties before and after the fit to data.

	Signal	$t\bar{t}$	Non-$t\bar{t}$	Total background
Luminosity	±2.8	±2.8	±2.8	±2.8
Lepton efficiencies	±1.6	±1.6	±1.5	±1.6
Jet energy scale	+3.4/−7.2	±16	+19/−9	+17/−12
Jet efficiencies	±1.5	±1.6	±1.6	±1.6
Jet energy resolution	±1.1	±0.6	±2.6	±1.8
b-tagging efficiency	±5.0	±0.7	±2.9	±2.0
c-tagging efficiency	±0.4	±1.2	±2.3	±1.9
Light jet-tagging efficiency	±0.2	±1.3	±1.6	±1.4
High-p_{T} tagging efficiency	±3.2	±1.3	±0.8	±1.1
Missing transverse energy	–	±2.6	–	±1.0
$t\bar{t}$: reweighting	–	±15	–	±5.9
$t\bar{t}$: parton shower	–	±9.3	–	±3.6
$t\bar{t}$+HF: normalisation	–	+12.0/−5.5	–	+4.5/−2.1
$t\bar{t}$+HF: modelling	–	±30	–	±11
Theoretical cross sections	–	±6.0	±33	±20
Multijet normalisation	–	–	±2.9	±1.8
Non-$t\bar{t}$ modelling	–	–	±2.3	±1.4
Total	+7.7/−10.0	±40	±35	±29

Table 6: Summary of the systematic uncertainties considered in the $T\bar{T} \to Wb$+X search with their impact (in %) on the normalisation of signal and backgrounds. Only sources of systematic uncertainty resulting in a normalisation change of at least 0.5% are displayed. The signal shown corresponds to a chiral fourth-generation T quark with mass m_T = 600 GeV.

≥6 j, ≥4 b, high $M_{bb}^{\min\Delta R}$							
	Pre-fit				Post-fit		
	Signal	$t\bar{t}$+light jets	$t\bar{t}+c\bar{c}$	$t\bar{t}+b\bar{b}$	$t\bar{t}$+light jets	$t\bar{t}+c\bar{c}$	$t\bar{t}+b\bar{b}$
Luminosity	±2.8	±2.8	±2.8	±2.8	±2.6	±2.6	±2.6
Lepton efficiencies	±1.5	±1.5	±1.5	±1.5	±1.5	±1.4	±1.5
Jet energy scale	±4.4	±15	±11	±12	±8.7	±6.4	±6.7
Jet efficiencies	–	±4.0	±2.2	±1.9	±2.7	±1.5	±1.3
Jet energy resolution	±0.1	±4.4	±3.8	±0.5	±3.1	±2.6	±0.4
b-tagging efficiency	±13	±5.6	±5.4	±9.3	±4.6	±4.6	±6.6
c-tagging efficiency	±1.6	±5.8	±12	±3.1	±5.6	±11	±2.9
Light jet-tagging efficiency	±0.6	±20	±5.7	±2.0	±17	±5.1	±1.8
High-p_{T} tagging efficiency	±4.8	±0.7	±1.7	±1.6	±0.6	±1.3	±1.2
$t\bar{t}$: reweighting	–	±13	±15	–	±10	±10	–
$t\bar{t}$: parton shower	–	±28	±17	±6.2	±13	±11	±4.0
$t\bar{t}$+HF: normalisation	–	–	±50	±50	–	±32	±18
$t\bar{t}$+HF: modelling	–	–	±17	±12	–	±16	±10
Theoretical cross sections	–	±6.3	±6.3	±6.3	±4.6	±4.6	±4.6
Total	±15	±42	±61	±55	±22	±30	±15

Table 7: Summary of the systematic uncertainties considered in the (≥6 j, ≥4 b, high $M_{bb}^{\min\Delta R}$) channel of the $T\bar{T} \to Ht$+X search with their impact (in %) on the normalisation of signal and backgrounds, before and after the fit to data. Only sources of systematic uncertainty resulting in a normalisation change of at least 0.5% are displayed. The signal shown corresponds to a singlet vector-like T quark with mass $m_T = 600$ GeV. The total post-fit uncertainty can be different from the sum in quadrature of individual sources due to the anti-correlations between them.

≥6 j, ≥4 b, high $M_{bb}^{\min\Delta R}$							
	Pre-fit				Post-fit		
	Signal	$t\bar{t}$+light jets	$t\bar{t}+c\bar{c}$	$t\bar{t}+b\bar{b}$	$t\bar{t}$+light jets	$t\bar{t}+c\bar{c}$	$t\bar{t}+b\bar{b}$
Luminosity	±2.8	±2.8	±2.8	±2.8	±2.7	±2.7	±2.7
Lepton efficiencies	±1.6	±1.4	±1.5	±1.7	±1.4	±1.5	±1.6
Jet energy scale	±5.6	±14	±14	±11	±13	±14	±11
Jet efficiencies	±3.1	±3.3	±1.0	±0.9	±3.2	±0.9	±0.8
Jet energy resolution	±0.1	±6.0	±1.1	±1.9	±4.5	±0.9	±1.5
b-tagging efficiency	±16	±7.6	±9.2	±16	±3.9	±5.2	±7.5
c-tagging efficiency	±1.0	±6.1	±15	±3.0	±5.8	±14	±2.8
Light jet-tagging efficiency	–	±19	±6.3	±2.4	±18	±5.8	±2.3
High-p_{T} tagging efficiency	±11	±2.7	±5.3	±5.0	±1.9	±3.8	±3.6
$t\bar{t}$: reweighting	–	±15	±16	–	±14	±15	–
$t\bar{t}$: parton shower	–	±22	±35	±26	±14	±33	±24
$t\bar{t}$+HF: normalisation	–	–	±50	±50	–	±44	±30
$t\bar{t}$+HF: modelling	–	–	±27	±24	–	±28	±21
Theoretical cross sections	–	±6.3	±6.2	±6.3	±5.9	±5.9	±5.9
Total	±21	±38	±73	±65	±24	±46	±27

Table 8: Summary of the systematic uncertainties considered in the (≥6 j, ≥4 b, high $M_{bb}^{\min\Delta R}$) channel of the $B\bar{B} \to Hb$+X search with their impact (in %) on the normalisation of signal and backgrounds, before and after the fit to data. Only sources of systematic uncertainty resulting in a normalisation change of at least 0.5% are displayed. The signal shown corresponds to a vector-like B quark with mass m_T = 600 GeV and $BR(B \to Hb) = 1$. The total post-fit uncertainty can be different from the sum in quadrature of individual sources due to the anti-correlations between them.

B. Post-fit event yields

Table 9 presents the observed and predicted background yields in each of the analysis channels for the $T\bar{T} \to Ht$+X search, after the fit to the data under the background-only hypothesis. The corresponding observed and predicted yields for the $B\bar{B} \to Hb$+X search are summarised in Table 10.

	5 j, 2 b	5 j, 3 b	5 j, ≥4 b	≥6 j, 2 b
$t\bar{t}$+light jets	32200 ± 1500	2940 ± 220	49.1 ± 8.8	16000 ± 1000
$t\bar{t} + c\bar{c}$	5600 ± 1700	1000 ± 310	61 ± 17	4300 ± 1300
$t\bar{t} + b\bar{b}$	1820 ± 360	990 ± 180	124 ± 19	1440 ± 280
$t\bar{t}V$	139 ± 44	25.0 ± 7.9	3.1 ± 1.0	164 ± 52
$t\bar{t}H$	39.8 ± 1.4	22.0 ± 1.2	6.1 ± 0.5	58.7 ± 2.9
W+jets	1200 ± 580	86 ± 41	4.3 ± 2.0	560 ± 280
Z+jets	390 ± 120	27.6 ± 8.7	1.6 ± 0.5	190 ± 60
Single top	1600 ± 260	172 ± 31	7.1 ± 0.8	710 ± 150
Diboson	88 ± 27	7.7 ± 2.6	0.4 ± 0.2	43 ± 13
Multijet	125 ± 40	31 ± 10	6.4 ± 2.2	52 ± 16
Total background	43240 ± 320	5360 ± 79	263 ± 10	23100 ± 240
Data	43319	5309	244	23001

	≥6 j, 3 b low $M_{bb}^{\min\Delta R}$	≥6 j, 3 b high $M_{bb}^{\min\Delta R}$	≥6 j, ≥4 b low $M_{bb}^{\min\Delta R}$	≥6 j, ≥4 b high $M_{bb}^{\min\Delta R}$
$t\bar{t}$+light jets	1260 ± 130	421 ± 43	38.3 ± 8.1	9.5 ± 2.1
$t\bar{t} + c\bar{c}$	760 ± 210	278 ± 79	72 ± 20	20.4 ± 6.2
$t\bar{t} + b\bar{b}$	730 ± 120	285 ± 51	211 ± 29	52.0 ± 7.9
$t\bar{t}V$	28.1 ± 8.9	12.3 ± 3.9	6.3 ± 2.0	1.5 ± 0.5
$t\bar{t}H$	25.0 ± 1.3	11.7 ± 0.9	11.1 ± 0.9	4.2 ± 0.4
W+jets	50 ± 25	12.0 ± 6.1	5.4 ± 2.9	0.4 ± 0.2
Z+jets	16.8 ± 5.5	3.3 ± 1.2	1.6 ± 0.5	0.3 ± 0.1
Single top	76 ± 17	33 ± 10	11.3 ± 3.2	2.8 ± 1.5
Diboson	4.3 ± 1.5	1.4 ± 0.5	0.4 ± 0.1	0.2 ± 0.1
Multijet	1.7 ± 0.7	4.3 ± 1.8	< 0.01	2.6 ± 0.8
Total background	2948 ± 54	1062 ± 25	357 ± 16	93.9 ± 5.0
Data	3015	1085	362	84

Table 9: Predicted and observed yields in each of the analysis channels considered by the $T\bar{T} \to Ht$+X search. The background prediction is shown after the combined fit to data in all channels under the background-only hypothesis. The quoted uncertainties are the sum in quadrature of statistical and systematic uncertainties on the yields, computed taking into account correlations among nuisance parameters and among processes.

	5 j, 2 b	5 j, 3 b	5 j, ≥4 b	≥6 j, 2 b
$t\bar{t}$+light jets	406 ± 35	77.8 ± 8.8	2.3 ± 0.5	239 ± 26
$t\bar{t} + c\bar{c}$	60 ± 31	25 ± 11	2.4 ± 1.1	58 ± 26
$t\bar{t} + b\bar{b}$	28 ± 10	35.4 ± 9.3	7.4 ± 1.9	33 ± 11
$t\bar{t}V$	4.2 ± 1.3	1.7 ± 0.5	0.3 ± 0.1	5.1 ± 1.6
$t\bar{t}H$	1.0 ± 0.1	1.2 ± 0.1	0.5 ± 0.1	1.5 ± 0.2
W+jets	23 ± 12	3.9 ± 2.0	0.8 ± 0.5	13.9 ± 7.5
Z+jets	7.2 ± 2.7	2.0 ± 2.2	0.6 ± 0.5	4.0 ± 3.1
Single top	41.5 ± 4.9	9.1 ± 1.2	0.6 ± 0.1	26.8 ± 4.2
Diboson	1.9 ± 0.8	0.5 ± 0.3	0.05 ± 0.05	1.2 ± 0.6
Multijet	< 0.01	< 0.01	0.3 ± 0.2	0.18 ± 0.01
Total background	573 ± 20	156.3 ± 8.5	15.2 ± 1.9	383 ± 16
Data	576	165	10	375

	≥6 j, 3 b low $M_{bb}^{\min\Delta R}$	≥6 j, 3 b high $M_{bb}^{\min\Delta R}$	≥6 j, ≥4 b low $M_{bb}^{\min\Delta R}$	≥6 j, ≥4 b high $M_{bb}^{\min\Delta R}$
$t\bar{t}$+light jets	23.4 ± 4.5	34.6 ± 4.9	1.5 ± 0.3	1.6 ± 0.4
$t\bar{t} + c\bar{c}$	12.0 ± 5.2	22 ± 10	2.5 ± 1.2	3.1 ± 1.4
$t\bar{t} + b\bar{b}$	19.6 ± 6.2	36 ± 11	11.8 ± 3.0	11.8 ± 3.1
$t\bar{t}V$	1.2 ± 0.4	1.7 ± 0.5	0.6 ± 0.2	0.4 ± 0.1
$t\bar{t}H$	0.7 ± 0.1	1.4 ± 0.2	0.5 ± 0.1	0.9 ± 0.1
W+jets	2.3 ± 1.3	1.3 ± 0.8	0.5 ± 0.5	0.07 ± 0.06
Z+jets	0.1 ± 0.1	0.2 ± 0.1	< 0.01	< 0.01
Single top	3.1 ± 0.4	4.7 ± 1.4	0.8 ± 0.1	0.4 ± 0.2
Diboson	0.2 ± 0.1	0.10 ± 0.03	0.02 ± 0.01	0.01 ± 0.01
Multijet	< 0.01	0.6 ± 0.2	< 0.01	0.4 ± 0.1
Total background	62.6 ± 5.3	101.9 ± 7.3	18.3 ± 2.6	18.6 ± 2.6
Data	62	103	23	20

Table 10: Predicted and observed yields in each of the analysis channels considered by the $B\bar{B} \to Hb$+X search. The background prediction is shown after the combined fit to data in all channels under the background-only hypothesis. The quoted uncertainties are the sum in quadrature of statistical and systematic uncertainties on the yields, computed taking into account correlations among nuisance parameters and among processes.

C. Limits on $T\bar{T}$ production from individual searches

Figure 27 shows 95% CL upper limits on the $T\bar{T}$ production cross section as a function of the T quark mass obtained by the individual $T\bar{T} \to Wb$+X and $T\bar{T} \to Ht$+X searches for the singlet scenario. The $T\bar{T} \to Wb$+X and $T\bar{T} \to Ht$+X searches yield observed (expected) 95% CL limits of $m_T > 660$ (665) GeV and $m_T > 765$ (720) GeV respectively. Figure 28 shows the 95% CL exclusion limits on vector-like T quark production, for different values of m_T and as a function of the two branching ratios $BR(T \to Wb)$ and $BR(T \to Ht)$, obtained by the $T\bar{T} \to Wb$+X search. Figure 29(a,b) present the corresponding expected and observed T quark mass limits respectively, in the plane of $BR(T \to Ht)$ versus $BR(T \to Wb)$. The exclusion limits obtained by the $T\bar{T} \to Ht$+X search can be found in Figs. 30 and 31. The $T\bar{T} \to Wb$+X search search set observed (expected) lower limits on the T quark mass ranging between 350 GeV and 760 GeV (350 GeV and 800 GeV) for all possible values of the branching ratios into the three decay modes. The $T\bar{T} \to Ht$+X search search set observed (expected) lower limits on the T quark mass ranging between 510 GeV and 950 GeV (505 GeV and 885 GeV) for all possible values of the branching ratios into the three decay modes.

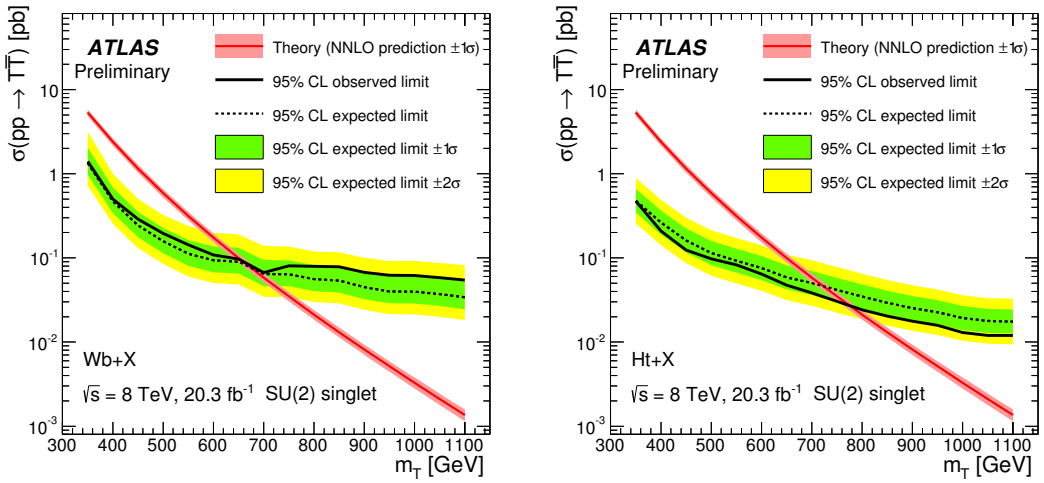

(a) (b)

Figure 27: Observed (solid line) and expected (dashed line) 95% CL upper limits on the $T\bar{T}$ cross section for a vector-like singlet T quark as a function of the T quark mass from (a) the $T\bar{T} \to Wb$+X search and (b) $T\bar{T} \to Ht$+X search. The surrounding shaded bands correspond to ±1 and ±2 standard deviations around the expected limit. The thin red line and band show the theoretical prediction and its ±1 standard deviation uncertainty.

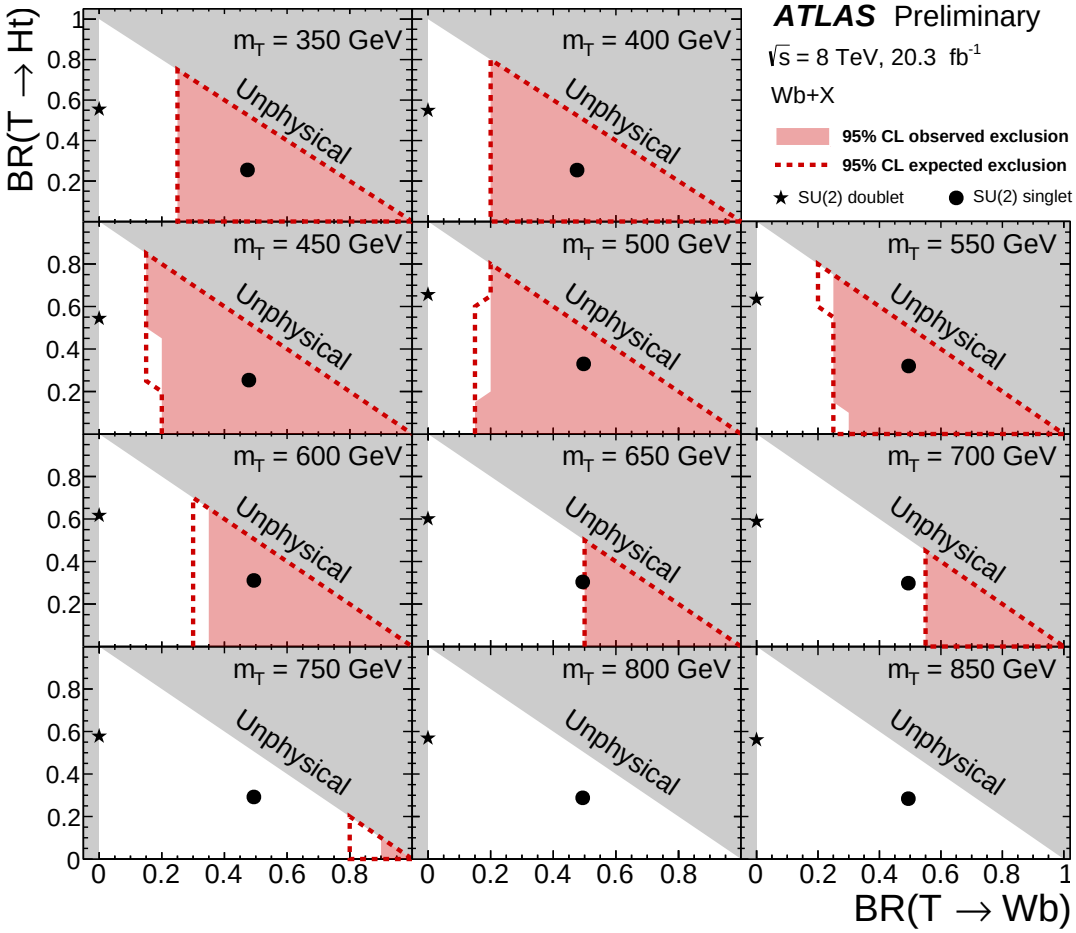

Figure 28: Observed (red filled area) and expected (red dashed line) 95% CL exclusion in the plane of $BR(T \to Wb)$ versus $BR(T \to Ht)$ for the $T\bar{T} \to Wb$+X search, for different values of the vector-like T quark mass. The grey (dark shaded) area corresponds to the unphysical region where the sum of branching ratios exceeds unity. The default branching ratio values from the Protos event generator for the weak-isospin singlet and doublet cases are shown as plain circle and star symbols respectively.

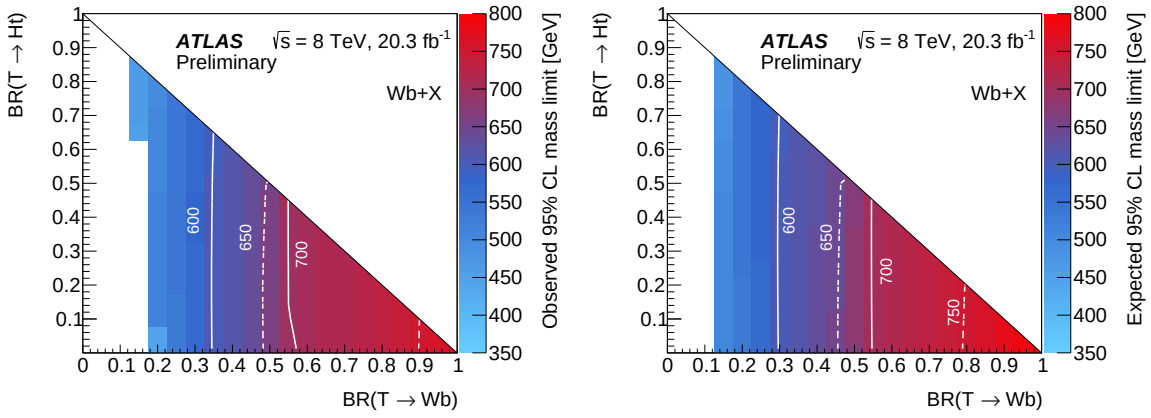

(a) (b)

Figure 29: Observed (a) and expected (b) limit (95% CL) on the mass of the T quark from the the $T\bar{T} \rightarrow Wb$+X search, and presented in the plane of $BR(T \rightarrow Ht)$ versus $BR(T \rightarrow Wb)$. The region shown in white is not excluded for any values of the T quark mass probed.

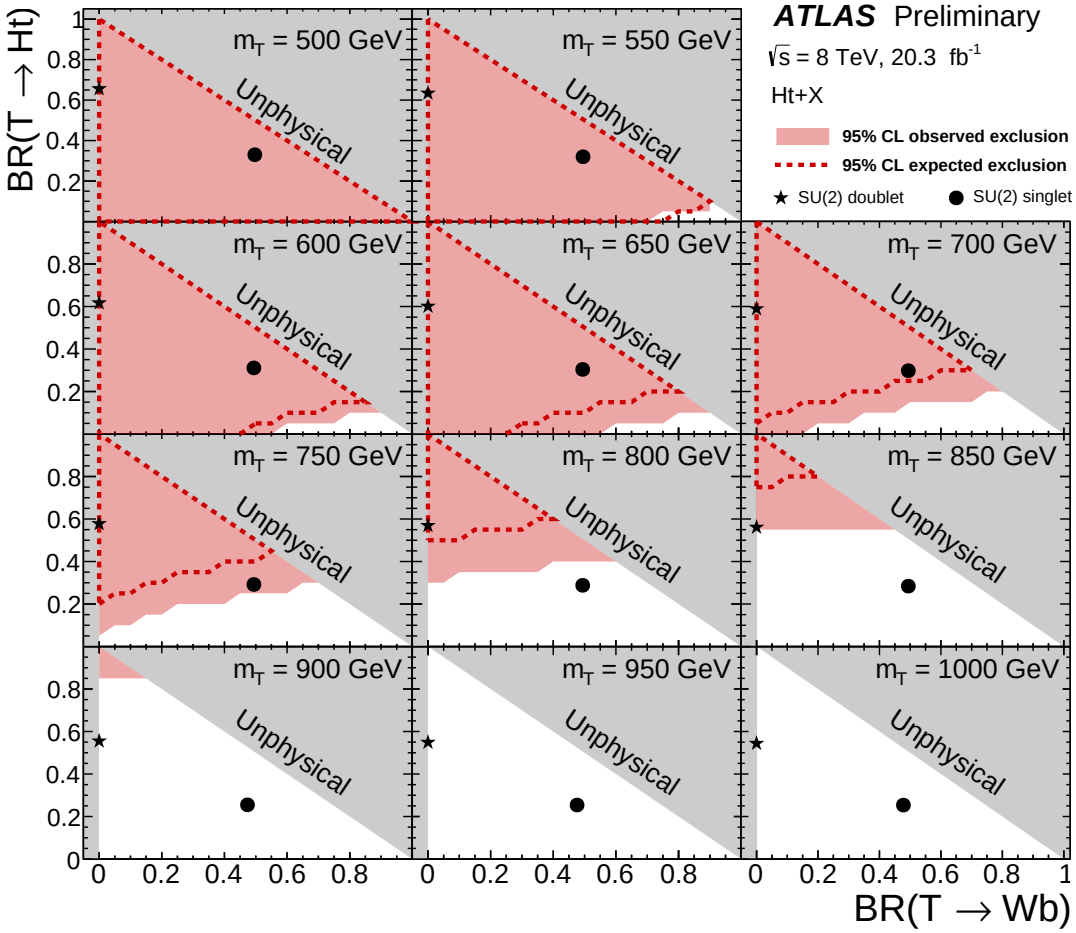

Figure 30: Observed (red filled area) and expected (red dashed line) 95% CL exclusion in the plane of $BR(T \to Wb)$ versus $BR(T \to Ht)$ for the $T\bar{T} \to Ht$+X search, for different values of the vector-like T quark mass. The grey (dark shaded) area corresponds to the unphysical region where the sum of branching ratios exceeds unity. The default branching ratio values from the Protos event generator for the weak-isospin singlet and doublet cases are shown as plain circle and star symbols respectively.

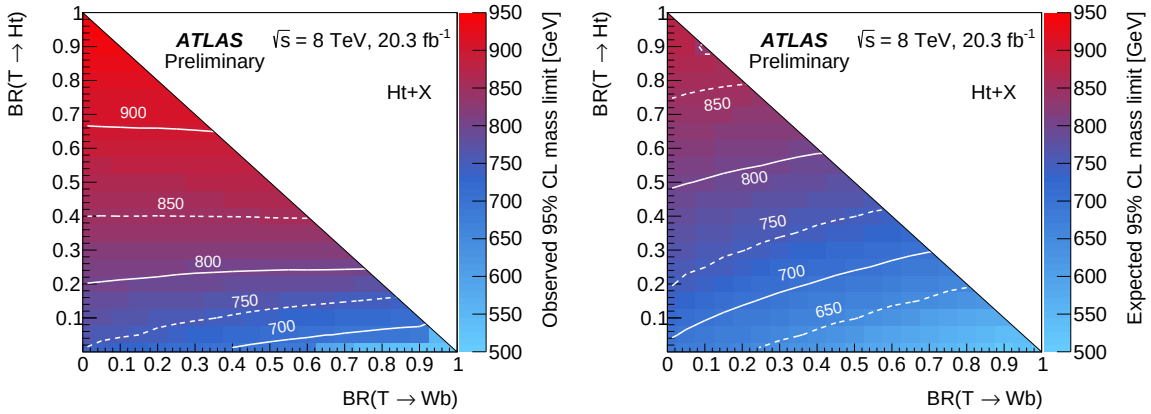

(a) (b)

Figure 31: Observed (a) and expected (b) limit (95% CL) on the mass of the T quark from the the $T\bar{T} \rightarrow Ht$+X search, and presented in the plane of $BR(T \rightarrow Ht)$ versus $BR(T \rightarrow Wb)$.

References

[1] ATLAS Collaboration, *Observation of a new particle in the search for the Standard Model Higgs boson with the ATLAS detector at the LHC*, Phys. Lett. B **716** (2012) 1–29, arXiv: 1207.7214 [hep-ex].

[2] CMS Collaboration, *Observation of a new boson at a mass of 125 GeV with the CMS experiment at the LHC*, Phys. Lett. B **716** (2012) 30–61, arXiv: 1207.7235 [hep-ex].

[3] L. Susskind, *Dynamics of Spontaneous Symmetry Breaking in the Weinberg-Salam Theory*, Phys. Rev. D **20** (1979) 2619–2625.

[4] N. Arkani-Hamed et al., *The Littlest Higgs*, JHEP **0207** (2002) 034, arXiv: hep-ph/0206021.

[5] M. Schmaltz and D. Tucker-Smith, *Little Higgs review*, Ann. Rev. Nucl. Part. Sci. **55** (2005) 229–270, arXiv: hep-ph/0502182.

[6] D. B. Kaplan, H. Georgi and S. Dimopoulos, *Composite Higgs Scalars*, Phys. Lett. B **136** (1984) 187.

[7] K. Agashe, R. Contino and A. Pomarol, *The Minimal composite Higgs model*, Nucl. Phys. B **719** (2005) 165–187, arXiv: hep-ph/0412089.

[8] C. T. Hill and E. H. Simmons, *Strong dynamics and electroweak symmetry breaking*, Phys. Rept. **381** (2003) 235–402, arXiv: hep-ph/0203079.

[9] F. del Aguila and M. J. Bowick, *The Possibility of New Fermions With $\Delta I = 0$ Mass*, Nucl. Phys. B **224** (1983) 107.

[10] J. Aguilar-Saavedra, *Identifying top partners at LHC*, JHEP **0911** (2009) 030, arXiv: 0907.3155 [hep-ph].

[11] J. Aguilar-Saavedra, *Mixing with vector-like quarks: constraints and expectations*, EPJ Web Conf. **60** (2013) 16012, arXiv: 1306.4432 [hep-ph].

[12] J. Aguilar-Saavedra et al., *Handbook of vectorlike quarks: Mixing and single production*, Phys. Rev. D **88** (2013) 094010, arXiv: 1306.0572 [hep-ph].

[13] A. Atre et al., *Heavy Quarks Above the Top at the Tevatron*, Phys. Rev. D **79** (2009) 054018, arXiv: 0806.3966 [hep-ph].

[14] A. Atre et al., *Model-Independent Searches for New Quarks at the LHC*, JHEP **1108** (2011) 080, arXiv: 1102.1987 [hep-ph].

[15] ATLAS Collaboration, *Search for pair production of a heavy up-type quark decaying to a W boson and a b quark in the lepton+jets channel with the ATLAS detector*, Phys. Rev. Lett. **108** (2012) 261802, arXiv: 1202.3076 [hep-ex].

[16] ATLAS Collaboration, *Search for pair-produced heavy quarks decaying to Wq in the two-lepton channel at $\sqrt{s} = 7$ TeV with the ATLAS detector*, Phys. Rev. D **86** (2012) 012007, arXiv: 1202.3389 [hep-ex].

[17] CMS Collaboration, *Search for pair produced fourth-generation up-type quarks in pp collisions at $\sqrt{s} = 7$ TeV with a lepton in the final state*, Phys. Lett. B **718** (2012) 307–328, arXiv: 1209.0471 [hep-ex].

[18] CMS Collaboration, *Search for heavy, top-like quark pair production in the dilepton final state in pp collisions at* $\sqrt{s}$ = 7 *TeV*, Phys. Lett. B **716** (2012) 103–121, arXiv: 1203.5410 [hep-ex].

[19] ATLAS Collaboration, *Search for pair production of a new quark that decays to a Z boson and a bottom quark with the ATLAS detector*, Phys. Rev. Lett. **109** (2012) 071801, arXiv: 1204.1265 [hep-ex].

[20] CMS Collaboration, *Search for heavy quarks decaying into a top quark and a W or Z boson using lepton + jets events in pp collisions at* $\sqrt{s}$ = 7 *TeV*, JHEP **1301** (2013) 154, arXiv: 1210.7471 [hep-ex].

[21] CMS Collaboration, *Search for a Vector-like Quark with Charge 2/3 in t + Z Events from pp Collisions at* $\sqrt{s}$ = 7 *TeV*, Phys. Rev. Lett. **107** (2011) 271802, arXiv: 1109.4985 [hep-ex].

[22] ATLAS Collaboration, *Search for down-type fourth generation quarks with the ATLAS detector in events with one lepton and hadronically decaying W bosons*, Phys. Rev. Lett. **109** (2012) 032001, arXiv: 1202.6540 [hep-ex].

[23] CMS Collaboration, *Search for heavy bottom-like quarks in 4.9 inverse femtobarns of pp collisions at* $\sqrt{s}$ = 7 *TeV*, JHEP **1205** (2012) 123, arXiv: 1204.1088 [hep-ex].

[24] ATLAS Collaboration, *Search for pair production of heavy top-like quarks decaying to a high-pT W boson and a b quark in the lepton plus jets final state at* $\sqrt{s}$=7 *TeV with the ATLAS detector*, Phys. Lett. B **718** (2013) 1284–1302, arXiv: 1210.5468 [hep-ex].

[25] ATLAS Collaboration, *Search for pair and single production of new heavy quarks that decay to a Z boson and a third-generation quark in pp collisions at* $\sqrt{s}$ = 8 *TeV with the ATLAS detector*, JHEP **1411** (2014) 104, arXiv: 1409.5500 [hep-ex].

[26] ATLAS Collaboration, *Search for vector-like B quarks in events with one isolated lepton, missing transverse energy, and jets at* $\sqrt{s}$ = 8 TeV *with the ATLAS detector*, To be submitted to Phys. Rev. D.

[27] ATLAS Collaboration, *Analysis of events with b-jets and two leptons of the same charge or three leptons in pp collisions at* $\sqrt{s}$ = 8 TeV *with the ATLAS detector*, To be submitted to JHEP.

[28] CMS Collaboration, *Inclusive search for a vector-like T quark with charge* $\frac{2}{3}$ *in pp collisions at* $\sqrt{s}$ = 8 *TeV*, Phys. Lett. B **729** (2014) 149–171, arXiv: 1311.7667 [hep-ex].

[29] ATLAS Collaboration, *The ATLAS Experiment at the CERN Large Hadron Collider*, JINST **3** (2008) S08003.

[30] ATLAS Collaboration, *Performance of the ATLAS Trigger System in 2010*, Eur. Phys. J. C **72** (2012) 1849, arXiv: 1110.1530 [hep-ex].

[31] ATLAS Collaboration, *Electron reconstruction and identification efficiency measurements with the ATLAS detector using the 2011 LHC proton-proton collision data*, Eur. Phys. J. C **C74** (2014) 2941, arXiv: 1404.2240 [hep-ex].

[32] ATLAS Collaboration, *Muon reconstruction efficiency and momentum resolution of the ATLAS experiment in proton-proton collisions at* $\sqrt{s}$ = 7 *TeV in 2010*, Eur. Phys. J. C **C74** (2014) 3034, arXiv: 1404.4562 [hep-ex].

[33] ATLAS Collaboration, *Measurement of the muon reconstruction performance of the ATLAS detector using 2011 and 2012 LHC proton-proton collision data*, Eur. Phys. J. C **C74** (2014) 3130, arXiv: 1407.3935 [hep-ex].

[34] M. Cacciari, G. P. Salam and G. Soyez, *The Anti-k(t) jet clustering algorithm*, JHEP **0804** (2008) 063, arXiv: 0802.1189 [hep-ph].

[35] M. Cacciari and G. P. Salam, *Dispelling the N^3 myth for the k_t jet-finder*, Phys. Lett. B **641** (2006) 57–61, arXiv: hep-ph/0512210.

[36] M. Cacciari, G. P. Salam and G. Soyez, *FastJet User Manual*, Eur. Phys. J. C **C72** (2012) 1896, arXiv: 1111.6097 [hep-ph].

[37] C. Cojocaru et al., *Hadronic calibration of the ATLAS liquid argon end-cap calorimeter in the pseudorapidity region $1.6 < |\eta| < 1.8$ in beam tests*, Nucl. Instrum. Meth. **A531** (2004) 481–514, arXiv: physics/0407009 [physics].

[38] W. Lampl et al., *Calorimeter Clustering Algorithms : Description and Performance*, ATL-LARG-PUB-2008-002 (2008), http://cds.cern.ch/record/1099735.

[39] G. Aad et al., *Jet energy measurement with the ATLAS detector in proton-proton collisions at $\sqrt{s} = 7$ TeV*, Eur.Phys.J. **C73**.3 (2013) 2304, arXiv: 1112.6426 [hep-ex].

[40] ATLAS Collaboration, *Jet energy measurement and its systematic uncertainty in proton-proton collisions at $\sqrt{s} = 7$ TeV with the ATLAS detector*, Eur. Phys. J. C **C75** (2015) 17, arXiv: 1406.0076 [hep-ex].

[41] ATLAS Collaboration, *Calibration of b-tagging using dileptonic top pair events in a combinatorial likelihood approach with the ATLAS experiment*, ATLAS-CONF-2014-004 (2014), http://cds.cern.ch/record/1664335.

[42] ATLAS Collaboration, *Calibration of the performance of b-tagging for c and light-flavour jets in the 2012 ATLAS data*, ATLAS-CONF-2014-046 (2014), http://cds.cern.ch/record/1741020.

[43] ATLAS Collaboration, *Performance of Missing Transverse Momentum Reconstruction in Proton-Proton Collisions at 7 TeV with ATLAS*, Eur. Phys. J. C **72** (2012) 1844, arXiv: 1108.5602 [hep-ex].

[44] ATLAS Collaboration, *Improved luminosity determination in pp collisions at sqrt(s) = 7 TeV using the ATLAS detector at the LHC*, Eur. Phys. J. C **73** (2013) 2518, arXiv: 1302.4393 [hep-ex].

[45] M. Czakon and A. Mitov, *Top++: A Program for the Calculation of the Top-Pair Cross-Section at Hadron Colliders*, Comput. Phys. Commun. **185** (2014) 2930, arXiv: 1112.5675 [hep-ph].

[46] M. Cacciari et al., *Top-pair production at hadron colliders with next-to-next-to-leading logarithmic soft-gluon resummation*, Phys. Lett. B **710** (2012) 612–622, arXiv: 1111.5869 [hep-ph].

[47] P. Bärnreuther, M. Czakon and A. Mitov, *Percent Level Precision Physics at the Tevatron: First Genuine NNLO QCD Corrections to $q\bar{q} \to t\bar{t} + X$*, Phys. Rev. Lett. **109** (2012) 132001, arXiv: 1204.5201 [hep-ph].

[48] M. Czakon and A. Mitov, *NNLO corrections to top-pair production at hadron colliders: the all-fermionic scattering channels*, JHEP **1212** (2012) 054, arXiv: 1207.0236 [hep-ph].

[49] M. Czakon and A. Mitov, *NNLO corrections to top pair production at hadron colliders: the quark-gluon reaction*, JHEP **1301** (2013) 080, arXiv: 1210.6832 [hep-ph].

[50] M. Czakon, P. Fiedler and A. Mitov, *Total Top-Quark Pair-Production Cross Section at Hadron Colliders Through $O(\alpha_S^4)$*, Phys. Rev. Lett. **110** (2013) 252004, arXiv: 1303.6254 [hep-ph].

[51] A. Martin et al., *Parton distributions for the LHC*, Eur. Phys. J. C **63** (2009) 189–285, arXiv: 0901.0002 [hep-ph].

[52] A. Martin et al., *Uncertainties on alpha(S) in global PDF analyses and implications for predicted hadronic cross sections*, Eur. Phys. J. C **64** (2009) 653–680, arXiv: 0905.3531 [hep-ph].

[53] M. Botje et al., *The PDF4LHC Working Group Interim Recommendations* (2011), arXiv: 1101.0538 [hep-ph].

[54] H.-L. Lai et al., *New parton distributions for collider physics*, Phys. Rev. D **82** (2010) 074024, arXiv: 1007.2241 [hep-ph].

[55] J. Gao et al., *CT10 next-to-next-to-leading order global analysis of QCD*, Phys. Rev. D **89** (2014) 033009, arXiv: 1302.6246 [hep-ph].

[56] R. D. Ball et al., *Parton distributions with LHC data*, Nucl. Phys. B **867** (2013) 244–289, arXiv: 1207.1303 [hep-ph].

[57] J. A. Aguilar-Saavedra, *PROTOS, a PROgram for TOp Simulations*, http://jaguilar.web.cern.ch/jaguilar/protos/.

[58] T. Sjöstrand, S. Mrenna and P. Z. Skands, *PYTHIA 6.4 Physics and Manual*, JHEP **0605** (2006) 026, arXiv: hep-ph/0603175.

[59] ATLAS Collaboration, *ATLAS tunes of PYTHIA6 and PYTHIA8 for MC11*, ATL-PHYS-PUB-2011-008 (2011), http://cds.cern.ch/record/1363300.

[60] ATLAS Collaboration, *New ATLAS event generator tunes to 2010 data*, ATL-PHYS-PUB-2011-009 (2011), http://cds.cern.ch/record/1345343.

[61] V. D. Barger, A. Stange and R. Phillips, *Four heavy quark hadroproduction*, Phys. Rev. D **44** (1991) 1987–1996.

[62] V. Barger, W.-Y. Keung and B. Yencho, *Triple-Top Signal of New Physics at the LHC*, Phys. Lett. B **687** (2010) 70–74, arXiv: 1001.0221 [hep-ph].

[63] A. Pomarol and J. Serra, *Top Quark Compositeness: Feasibility and Implications*, Phys. Rev. D **78** (2008) 074026, arXiv: 0806.3247 [hep-ph].

[64] B. Lillie, J. Shu and T. M. Tait, *Top Compositeness at the Tevatron and LHC*, JHEP **0804** (2008) 087, arXiv: 0712.3057 [hep-ph].

[65] K. Kumar, T. M. Tait and R. Vega-Morales, *Manifestations of Top Compositeness at Colliders*, JHEP **0905** (2009) 022, arXiv: 0901.3808 [hep-ph].

[66] M. Guchait, F. Mahmoudi and K. Sridhar, *Associated production of a Kaluza-Klein excitation of a gluon with a t anti-t pair at the LHC*, Phys. Lett. B **666** (2008) 347–351, arXiv: 0710.2234 [hep-ph].

[67] C. Degrande et al., *Non-resonant New Physics in Top Pair Production at Hadron Colliders*, JHEP **1103** (2011) 125, arXiv: 1010.6304 [hep-ph].

[68] H. Georgi et al., *Effects of top compositeness*, Phys. Rev. D **51** (1995) 3888–3894, arXiv: hep-ph/9410307.

[69] T. Plehn and T. M. Tait, *Seeking Sgluons*, J. Phys. **G36** (2009) 075001, arXiv: 0810.3919 [hep-ph].

[70] S. Choi et al., *Color-Octet Scalars of N=2 Supersymmetry at the LHC*, Phys. Lett. B **672** (2009) 246–252, arXiv: 0812.3586 [hep-ph].

[71] C. Kilic, T. Okui and R. Sundrum, *Vectorlike Confinement at the LHC*, JHEP **1002** (2010) 018, arXiv: 0906.0577 [hep-ph].

[72] C. Kilic, T. Okui and R. Sundrum, *Colored Resonances at the Tevatron: Phenomenology and Discovery Potential in Multijets*, JHEP **0807** (2008) 038, arXiv: 0802.2568 [hep-ph].

[73] G. Burdman, B. A. Dobrescu and E. Ponton, *Resonances from two universal extra dimensions*, Phys. Rev. D **74** (2006) 075008, arXiv: hep-ph/0601186.

[74] S. Calvet et al., *Searching for sgluons in multitop events at a center-of-mass energy of 8 TeV*, JHEP **1304** (2013) 043, arXiv: 1212.3360 [hep-ph].

[75] G. Cacciapaglia, A. Deandrea and J. Llodra-Perez, *A Dark Matter candidate from Lorentz Invariance in 6D*, JHEP **1003** (2010) 083, arXiv: 0907.4993 [hep-ph].

[76] G. Cacciapaglia et al., *Four tops on the real projective plane at LHC*, JHEP **1110** (2011) 042, arXiv: 1107.4616 [hep-ph].

[77] A. Arbey et al., *Dark Matter in a twisted bottle*, JHEP **1301** (2013) 147, arXiv: 1210.0384 [hep-ph].

[78] J. Alwall et al., *MadGraph/MadEvent v4: The New Web Generation*, JHEP **0709** (2007) 028, arXiv: 0706.2334 [hep-ph].

[79] T. Sjostrand, S. Mrenna and P. Z. Skands, *A Brief Introduction to PYTHIA 8.1*, Comput. Phys. Commun. **178** (2008) 852–867, arXiv: 0710.3820 [hep-ph].

[80] P. Meade and M. Reece, *BRIDGE: Branching ratio inquiry / decay generated events* (2007), arXiv: hep-ph/0703031.

[81] P. M. Nadolsky et al., *Implications of CTEQ global analysis for collider observables*, Phys. Rev. D **78** (2008) 013004, arXiv: 0802.0007 [hep-ph].

[82] D. Goncalves-Netto et al., *Sgluon Pair Production to Next-to-Leading Order*, Phys. Rev. D **85** (2012) 114024, arXiv: 1203.6358 [hep-ph].

[83] ATLAS Collaboration, *The ATLAS Simulation Infrastructure*, Eur. Phys. J. C **70** (2010) 823–874, arXiv: 1005.4568 [physics.ins-det].

[84] S. Agostinelli et al., *GEANT4: A Simulation toolkit*, Nucl. Instrum. Meth. **A506** (2003) 250–303.

[85] P. Golonka and Z. Was, *PHOTOS Monte Carlo: A Precision tool for QED corrections in Z and W decays*, Eur. Phys. J. C **45** (2006) 97–107, arXiv: hep-ph/0506026.

[86] S. Jadach, J. H. Kuhn and Z. Was,
TAUOLA: A Library of Monte Carlo programs to simulate decays of polarized tau leptons,
Comput. Phys. Commun. **64** (1990) 275–299.

[87] P. Nason, *A New method for combining NLO QCD with shower Monte Carlo algorithms*,
JHEP **0411** (2004) 040, arXiv: hep-ph/0409146.

[88] S. Frixione, P. Nason and C. Oleari,
Matching NLO QCD computations with Parton Shower simulations: the POWHEG method,
JHEP **0711** (2007) 070, arXiv: 0709.2092 [hep-ph].

[89] S. Alioli et al., *A general framework for implementing NLO calculations in shower Monte Carlo programs: the POWHEG BOX*, JHEP **1006** (2010) 043, arXiv: 1002.2581 [hep-ph].

[90] P. Z. Skands, *Tuning Monte Carlo Generators: The Perugia Tunes*,
Phys. Rev. D **82** (2010) 074018, arXiv: 1005.3457 [hep-ph].

[91] G. Corcella et al., *HERWIG 6: An Event generator for hadron emission reactions with interfering gluons (including supersymmetric processes)*, JHEP **0101** (2001) 010,
arXiv: hep-ph/0011363.

[92] J. Butterworth, J. R. Forshaw and M. Seymour,
Multiparton interactions in photoproduction at HERA, Z. Phys. C **72** (1996) 637–646,
arXiv: hep-ph/9601371.

[93] ATLAS Collaboration, *Measurements of normalized differential cross sections for $t\bar{t}$ production in pp collisions at $\sqrt{s} = 7$ TeV using the ATLAS detector*, Phys. Rev. D **90** (2014) 072004,
arXiv: 1407.0371 [hep-ex].

[94] F. Cascioli et al., *NLO matching for $t\bar{t}b\bar{b}$ production with massive b-quarks*,
Phys. Lett. B **734** (2014) 210–214, arXiv: 1309.5912 [hep-ph].

[95] T. Gleisberg et al., *Event generation with SHERPA 1.1*, JHEP **0902** (2009) 007,
arXiv: 0811.4622 [hep-ph].

[96] F. Cascioli, P. Maierhofer and S. Pozzorini, *Scattering Amplitudes with Open Loops*,
Phys. Rev. Lett. **108** (2012) 111601, arXiv: 1111.5206 [hep-ph].

[97] ATLAS Collaboration, *Search for the Standard Model Higgs boson produced in association with top quarks and decaying into $b\bar{b}$ in pp collisions at $\sqrt{s} = 8$ TeV with the ATLAS detector*,
To be submitted to Eur. Phys. J. C.

[98] M. L. Mangano et al.,
ALPGEN, a generator for hard multiparton processes in hadronic collisions,
JHEP **0307** (2003) 001, arXiv: hep-ph/0206293.

[99] M. L. Mangano, M. Moretti and R. Pittau, *Multijet matrix elements and shower evolution in hadronic collisions: $Wb\bar{b}$ + n jets as a case study*, Nucl. Phys. B **632** (2002) 343–362,
arXiv: hep-ph/0108069.

[100] K. Melnikov and F. Petriello,
*Electroweak gauge boson production at hadron colliders through O(alpha(s)**2)*,
Phys. Rev. D **74** (2006) 114017, arXiv: hep-ph/0609070.

[101] S. Frixione et al., *Single-top production in MC@NLO*, JHEP **0603** (2006) 092,
arXiv: hep-ph/0512250.

[102] N. Kidonakis, *Next-to-next-to-leading-order collinear and soft gluon corrections for t-channel single top quark production*, Phys. Rev. D **83** (2011) 091503, arXiv: 1103.2792 [hep-ph].

[103] N. Kidonakis, *Two-loop soft anomalous dimensions for single top quark associated production with a W- or H-*, Phys. Rev. D **82** (2010) 054018, arXiv: 1005.4451 [hep-ph].

[104] N. Kidonakis, *NNLL resummation for s-channel single top quark production*, Phys. Rev. D **81** (2010) 054028, arXiv: 1001.5034 [hep-ph].

[105] J. M. Campbell and R. K. Ellis, *An Update on vector boson pair production at hadron colliders*, Phys. Rev. D **60** (1999) 113006, arXiv: hep-ph/9905386.

[106] G. Bevilacqua et al., *HELAC-NLO*, Comput. Phys. Commun. **184** (2013) 986–997, arXiv: 1110.1499 [hep-ph].

[107] J. M. Campbell and R. K. Ellis, *$t\bar{t}W^{+-}$ production and decay at NLO*, JHEP **1207** (2012) 052, arXiv: 1204.5678 [hep-ph].

[108] M. Garzelli et al., *$t\,\bar{t}\,W^{+-}$ and $t\,\bar{t}\,Z$ Hadroproduction at NLO accuracy in QCD with Parton Shower and Hadronization effects*, JHEP **1211** (2012) 056, arXiv: 1208.2665 [hep-ph].

[109] S. Dawson et al., *Associated Higgs production with top quarks at the Large Hadron Collider: NLO QCD corrections*, Phys. Rev. D **68** (2003) 034022, arXiv: hep-ph/0305087.

[110] L. Reina and S. Dawson, *Next-to-leading order results for $t\bar{t}h$ production at the Tevatron*, Phys. Rev. Lett. **87** (2001) 201804, arXiv: hep-ph/0107101.

[111] W. Beenakker et al., *NLO QCD corrections to $t\bar{t}H$ production in hadron collisions*, Nucl. Phys. B **653** (2003) 151–203, arXiv: hep-ph/0211352.

[112] W. Beenakker et al., *Higgs radiation off top quarks at the Tevatron and the LHC*, Phys. Rev. Lett. **87** (2001) 201805, arXiv: hep-ph/0107081.

[113] A. Djouadi, J. Kalinowski and M. Spira, *HDECAY: A Program for Higgs boson decays in the standard model and its supersymmetric extension*, Comput. Phys. Commun. **108** (1998) 56–74, arXiv: hep-ph/9704448.

[114] A. Bredenstein et al., *Precise predictions for the Higgs-boson decay $H \to WW/ZZ \to 4$ leptons*, Phys. Rev. D **74** (2006) 013004, arXiv: hep-ph/0604011.

[115] S. Actis et al., *NNLO Computational Techniques: The Cases $H \to \gamma\gamma$ and $H \to gg$*, Nucl. Phys. B **811** (2009) 182–273, arXiv: 0809.3667 [hep-ph].

[116] A. Denner et al., *Standard Model Higgs-Boson Branching Ratios with Uncertainties*, Eur. Phys. J. C **71** (2011) 1753, arXiv: 1107.5909 [hep-ph].

[117] S. Dittmaier et al., *Handbook of LHC Higgs Cross Sections: 1. Inclusive Observables* (2011), arXiv: 1101.0593 [hep-ph].

[118] ATLAS Collaboration, *Measurement of the top quark-pair production cross section with ATLAS in pp collisions at $\sqrt{s} = 7$ TeV*, Eur. Phys. J. C **71** (2011) 1577, arXiv: 1012.1792 [hep-ex].

[119] J. Alwall et al., *Comparative study of various algorithms for the merging of parton showers and matrix elements in hadronic collisions*, Eur. Phys. J. C **53** (2008) 473–500, arXiv: 0706.2569 [hep-ph].

[120] S. Frixione et al., *Single-top hadroproduction in association with a W boson*, JHEP **0807** (2008) 029, arXiv: 0805.3067 [hep-ph].

[121] W. Verkerke and D. P. Kirkby, *The RooFit toolkit for data modeling*, eConf **C0303241** (2003) MOLT007, arXiv: physics/0306116 [physics].

[122] W. Verkerke and D. Kirkby, *RooFit Users Manual*, http://roofit.sourceforge.net/.

[123] G. Cowan et al., *Asymptotic formulae for likelihood-based tests of new physics*, Eur. Phys. J. C **71** (2011) 1554, arXiv: 1007.1727 [physics.data-an].

[124] T. Junk, *Confidence level computation for combining searches with small statistics*, Nucl. Instrum. Meth. **A434** (1999) 435–443, arXiv: hep-ex/9902006.

[125] A. L. Read, *Presentation of search results: The CL(s) technique*, J. Phys. **G28** (2002) 2693–2704.